

Carnegie Mellon University

CARNEGIE INSTITUTE OF TECHNOLOGY

THESIS

SUBMITTED IN PARTIAL FULFILLMENT OF THE REQUIREMENTS
FOR THE DEGREE OF **Doctor of Philosophy**

TITLE

Mode-resolved thermal transport across semiconductor
heterostructures

Presented by **SIMON LU**

**ACCEPTED BY THE DEPARTMENT OF
MECHANICAL ENGINEERING**

ADVISOR, MAJOR PROFESSOR

DATE

DEPARTMENT HEAD

DATE

APPROVED BY THE COLLEGE COUNCIL

DEAN

DATE

**MODE-RESOLVED THERMAL TRANSPORT
ACROSS SEMICONDUCTOR
HETEROSTRUCTURES**

Submitted in partial fulfillment of the requirements for the degree of
DOCTOR OF PHILOSOPHY
in
MECHANICAL ENGINEERING.

Simon Lu

S.B., Physics, Massachusetts Institute of Technology, MA, USA

S.B., Aerospace Engineering, Massachusetts Institute of Technology, MA, USA

Carnegie Institute of Technology

Carnegie Mellon University

Pittsburgh, PA 15213

September 2016

Copyright © 2016 Simon Lu.

Abstract

Mode-resolved thermal transport across semiconductor heterostructures

by
Simon Lu

Chair: [Professor Alan J. H. McGaughey](#)

Thermal transport across three-dimensional Lennard-Jones superlattices, two-dimensional heterostructures of graphene and hexagonal boron nitride (hBN), and in C_{60} molecular crystals is studied atomistically. The first two systems are studied as finite junctions placed between bulk leads, while the molecular crystal is studied as a bulk. Two computational methods are used: molecular dynamics (MD) simulations and harmonic lattice dynamics calculations in conjunction with the scattering boundary method (SBM).

In Lennard-Jones superlattice junctions with a superlattice period of four atomic monolayers at low temperatures, those with mass-mismatched leads have a greater thermal conductance than those with mass-matched leads. We attribute this lead effect to interference between and the ballistic transport of emergent junction vibrational modes. The lead effect diminishes when the temperature is increased, when the superlattice period is increased, and when interfacial disorder is introduced, and is reversed in the harmonic limit.

In graphene-hBN heterostructure junctions, the thermal conductance is dominated by acoustic phonon modes near the Brillouin zone center that have high group velocity, population, and transmission coefficient. Out-of-plane modes make their most significant contributions at low frequencies, whereas in-plane modes contribute across the frequency spectrum. Finite-length superlattice junctions between graphene and hBN leads have a lower thermal conductance than comparable junctions between two graphene leads due to lack of transmission in the hBN phonon band gap. The thermal conductances of bilayer systems differ by less than 10% from their single-layer counterparts on a per area basis, in contrast to the strong thermal conductivity reduction when moving to from single- to multi-layer

graphene.

We model C_{60} molecules using the polymer consistent force-field and compute the single molecule vibrational spectrum and heat capacity. In the face-center cubic C_{60} molecular crystal at a temperature of 300 K, we find three frequency peaks in the center-of-mass translations at 20, 30 and 38 cm^{-1} , agreeing with the average frequencies of the three acoustic branches of the frozen phonon model of the same system and suggesting that a phonon description of center-of-mass translations. We use both direct method and Green-Kubo MD simulations to predict the thermal conductivity of the molecular crystals at a temperature of 300 K. We find that the thermal conductivity of the molecular crystal is 20 to 50% lower than that of a reduced order model where only molecular center-of-mass translations are present, suggesting that molecular vibrations and rotations act as significant scattering sources for the center-of-mass phonons.

Acknowledgements

I would like to thank my parents, and to remember my dad. I think back now and I believe many if not most of my current interests were a direct result of his influence. He got me interested in engineering at a point where I did not even know what engineering was. After his untimely departure, my mom heroically took over everything, and has since been a tireless advocate for me, regardless of the situation. A Ph.D. is not an easy thing, nor a necessary thing, for a person to do, however, due to my upbringing, it always seemed like the inevitable thing.

In direct relation to my thesis, I would like to thank Professor Alan McGaughey above all else. Without his invitation to conduct research at CMU and his support and guidance along the way, this document would not have been possible. I would like to recognize him especially for his leniency in allowing me to explore coursework not directly related to my thesis research, as it has made my time at CMU a much more enriching experience. I would also like to thank Professor Jonathan Malen, who has reviewed and commented on my work throughout my time at CMU as a part of the Supergroup, Professor Michael Widom, for advising me on the radiation boundary condition used in this thesis, and finally Professor Di Xiao, for agreeing to serve on my committee despite never having crossed paths with me before.

It would have been impossible to tolerate the five long years of this program without friends, and it is with great fortune that many of my labmates have become good friends of mine over the years. I would especially like to recognize Dr. Justin Feig, Kevin Parrish, Dr. Ankit Jain, and Dr. Baoan Liu for a great deal of support in troubling times, for eye-opening discussion, and for being good friends. I'd also like to thank the other members of the Supergroup in my cohort and some students outside the supergroup: Dr. Jiawei Shi, Dr. Pengfei Li, Dr. Wee-Liat Ong, Dr. Shubhaditya Majumdar, Dr. Ying-Ju Yu,

Dr. Keith Regner, Dr. Justin Freedman, and Lily Ehrlich. They formed a very warm and hospitable work community. I also want to recognize the surprising friendship of newer students, particularly Paarth Thapar, Bowen Yu, Sushant Kumar, whom I worked with extensively on C_{60} , Wei Gong, for letting me borrow his car countless times, Dipanjan Saha, and Jiayu Li.

Last but certainly not least, I recognize the funding sources which enabled my work and livelihood in Pittsburgh. First, NSF grant number DMR1006480, which supported the superlattice junction project as well as the graphene/hBN project. Second, the Jean-Francois and Catherine Heitz Scholarship at Carnegie Mellon University which generously supported me in the interim. Finally, NSF grant number DMR1507325, which currently supports the C_{60} project.

Contents

Abstract	iv
Acknowledgements	vi
List of Figures	xiii
List of Tables	xix
Nomenclature	xx
1 Introduction	1
1.1 Motivation	1
1.2 Objectives	2
1.2.1 Overview	2
1.2.2 Three-dimensional semiconductor junctions	3
1.2.3 Two-dimensional semiconductor junctions	3
1.2.4 Molecular crystals	3
1.3 Methods	4
1.4 Overview	5
2 Theory and methods	7

2.1	Introduction	7
2.2	Molecular dynamics simulations	9
2.2.1	Formulation	9
2.2.2	Temperature in MD	11
2.2.3	Direct heat MD simulation	12
2.3	Harmonic lattice dynamics calculations	18
2.3.1	Formulation	18
2.3.2	Temperature in HLD	24
2.3.3	Crystal thermal conductivity	25
2.4	Scattering boundary method	27
2.4.1	Landauer formalism	27
2.4.2	Scattering boundary equations	30
2.4.3	Symmetry considerations	33
2.4.3.1	Crystal momentum conservation	34
2.4.3.2	Energy conservation	35
3	Lennard-Jones superlattice junctions	39
3.1	Introduction	39
3.2	Superlattice junction structure: the multiple thin film system	41
3.3	Methods	43
3.3.1	Thermal circuit	43
3.3.2	Non-equilibrium molecular dynamics	44
3.3.3	Scattering boundary method	47
3.3.3.1	Landauer formula	47
3.3.3.2	Determination of scattered modes	49
3.3.3.3	Scattering boundary equations	50

3.4	Results	52
3.4.1	NEMD indicates a lead effect	52
3.4.2	Lead effect is reversed in harmonic calculation	55
3.5	Summary	57
4	Graphene/hBN heterostructures	61
4.1	Introduction	61
4.2	Thermal conductance model	63
4.2.1	Landauer formalism	63
4.2.2	Junction configurations and force constants	65
4.3	Results	69
4.3.1	Junction Types I and II: Cross-interface interaction	69
4.3.2	Junction Type III: Finite superlattices	75
4.3.3	Junction Types II-S and IV: Substrates and bilayers	77
4.4	Summary	81
5	C₆₀ molecular crystal	83
5.1	Introduction	83
5.2	C ₆₀ model	85
5.2.1	Structure	85
5.2.2	Polymer consistent force-field	87
5.2.3	Point mass	89
5.3	Thermal conductivity calculation	90
5.4	Results	92
5.4.1	Validation	92
5.4.2	Thermal conductivity	93
5.5	Conclusions	95

6	Summary and future work	97
6.1	Overview	97
6.1.1	Summary	97
6.1.2	Molecular dynamics versus scattering boundary method	99
6.2	Future work	101
6.2.1	Coupled leads	101
6.2.2	C_{60} intercage thermal conductance	103
A	Intermolecular interactions by mode projection	105
A.1	Theory	105
A.2	Toy example	108
A.3	Towards thermal conductance	111
B	Phonons as an operator equation	113
	Bibliography	117

List of Figures

- 2.1 Workflow for direct heat MD simulations. Blue boxes indicate pre- and post-simulation tasks, while black boxes indicate tasks completed within the MD simulation program. 17

- 2.2 A schematic of a junction system in the Landauer formalism. Bulk leads L and R are connected via the junction, but the leads are positioned far from the junction. Phonon scattering events, as represented by the transmission event of a single phonon into two, occur within the junction. 30

- 2.3 Schematic representation of the SBM computational cell for an armchair interface indicating the left boundary (red) and right boundary (blue). . . 33

- 2.4 Workflow for SBM calculations. Blue boxes represent pre- and post-processing steps, while black boxes indicate calculations done within the SBM program. Dotted gray boxes indicate computations that must be repeated for every wavevector, and every phonon polarization at a wavevector. 37

- 3.1 Example structure for the case of eight thin films ($m = 8$, a mismatched case) with five monolayers per thin film ($n = 5$). Cyan atoms are Type 1 and pink atoms are Type 2. The red and blue atoms are in the reservoirs and the gray atoms are fixed for use in the MD simulations. 42

3.2	Temperature profile from NEMD for eight films ($m = 8$) of eight atomic monolayers each ($n = 8$) at an average temperature of 20 K. The error bars on the monolayer temperatures represent their standard deviation over the data collection time steps. The intrajunction films are numbered 1 through 8, while the left and right leads are labeled L and R.	45
3.3	Intrajunction (a) film thermal conductivities and (b) film-film interface thermal conductances for the same case as Fig. 3.2 ($n = 8, m = 8$). These data are averaged from temperature profiles from five independent NEMD runs, including the profile shown in Fig. 3.2. They are compared against temperature-dependent NEMD values of bulk thermal conductivity and isolated interface thermal conductance. The error bars indicate the standard deviation over the five independent runs.	46
3.4	Length-dependent junction thermal conductances for the cases (a) $n = 2, T = 20$ K, (b) $n = 2, T = 40$ K, (c) $n = 8, T = 20$ K, and (d) $n = 2, T = 20$ K with $p = 0.2$ interfacial species disorder from NEMD and the thermal circuit model. The $n = 2, T = 20$ K case shows a strong lead effect, which persists as the number of junction thin films increases. The lead effect is diminished at higher temperatures, greater number of monolayers per thin film, and with the introduction of species disorder at the interfaces. . . .	51
3.5	Length-dependent junction thermal conductances for the case $n = 2, T = 20$ K from NEMD simulations and the SBM calculations. Red and blue curves under the square symbols are power law fits to the NEMD data. Red and blue lines under the diamond symbols are the length-converged SBM results.	55

3.6	Transmission coefficient versus frequency color histograms from the SBM for length-converged matched and mismatched cases. Since these results represent length-converged systems, differences in transmission coefficients between the two cases are due to differences in the right lead mass. The cutoff frequency of Type 2 argon is 7.23 Trad/s. Different colors represent the number of modes in bins of frequency and transmission coefficient. . . .	57
3.7	Accumulation of junction thermal conductance with frequency from the SBM for length-converged matched and mismatched cases.	58
4.1	Graphene/hBN interfaces: (a) armchair and (b) boron-bonded zig-zag. . .	68
4.2	Phonon dispersion along the high symmetry loop Γ -M-K- Γ in the first Brillouin zone of (a) graphene and (b) hBN using force constants from the Tersoff potential. The quadratic z -acoustic (ZA) branch is indicated for both systems. The band gap in hBN is highlighted. Both graphene and hBN are at a lattice constant of 1.4422 Å	70
4.3	The Landauer integrand [Eq. (4.1)] throughout the graphene first Brillouin zone for the (a) Type IA, (b) Type IZ, (c) Type IIA, (d) Type IIZ, (e) Type III: $2 \times 2 \times 14$, and (f) Type III: $2 \times 2 \times 14.5$ junctions. κ_x and κ_y are given in units of \AA^{-1} . In (f), the white dashed line highlights contributions of modes whose frequencies lie within the hBN band gap. These modes contribute in cases of matched leads (f), but not in cases of mismatched leads (e). . . .	72
4.4	(a) Accumulation and (b) modal contribution to thermal conductance as a function of frequency for Type IIA junctions. Note that the characteristic thermal frequency at 300 K is 39.2 Trad/s.	74

4.5	Thermal conductance of Type III junctions as a function of the number of superlattice periods. The purple line corresponds to a single graphene/hBN interface. The gray lines serve as a guide for the eye.	77
4.6	Modal transmission coefficient versus frequency for (a) Type IIA, (b) Type IVA-1 and (c) Type IVA-2 junctions and their corresponding thermal conductances as calculated from the SBM.	80
5.1	A single C ₆₀ molecule, viewed along the z -axis of construction.	86
5.2	The effective molecular pair potential $U_{\text{Eff}}(r)$ used in point mass simulations. The vertical line crosses the minimum of the potential, which occurs at a pair separation of 9 Å.	91
5.3	A diagram of a full degree of freedom C ₆₀ direct method MD simulation cell along with the temperature profile for a 15 unit cell (216 nm) long sample. Note that the rotational orientations of the C ₆₀ are random. Each data point represents the temperature of a layer of C ₆₀ molecules. The error bars represent the standard deviation of the kinetic energy within a layer (see Sec. 2.2.2).	92
5.4	The (a) heat capacity and (b) spectrum of molecular vibrations of a single C ₆₀ molecule from the PCFF model compared to that using first principals density functional theory. Note that the experimental value was measured by Jin <i>et al.</i> [121] from crystalline C ₆₀ and has been normalized to a single crystal.	94
5.5	The frequency spectrum of center of mass translations in FCC C ₆₀ using the PCFF compared against the frozen phonon dispersion by Jin <i>et al.</i> , also produced from PCFF. The three peaks highlighted in red correspond with the average frequencies of the three acoustic branches.	94

5.6	Thermal conductivity of full degree of freedom and center-of-mass translation only C ₆₀ systems at a temperature of 300 K.	96
-----	---	----

List of Tables

4.1 Junction configurations considered. G and BN indicate the Broido *et al.* [101] and Sevik *et al.* [102] Tersoff interaction parameters for graphene and hBN. G' indicates a system using graphene Tersoff parameters but with hBN atomic masses. In cases where both graphene and hBN use the same Tersoff parameters, no cross-interface mixing is used. Otherwise, appropriate mixing rules are applied. 67

Nomenclature

Abbreviations

FBZ First Brillouin zone.

FCC Face-centered cubic.

HLD Harmonic lattice dynamics.

LAMMPS Large-scale Atomic/Molecular Massively Parallel Simulator.

LJ Lennard-Jones.

MD Molecular dynamics.

NEMD Non-equilibrium molecular dynamics.

PCFF Polymer consistent force field.

SBM Scattering boundary method.

UC Unit cell.

Subscripts

i, j Atom index in system or in unit cell.

n, l Unit cell index.

Superscripts

α, β Cartesian direction index.

\dagger Transpose complex conjugate.

p At the p^{th} time step.

Variables

$\alpha, \alpha_{\text{R} \rightarrow \text{L}}$ Phonon transmission coefficient.

ΔT Change in temperature (e.g., across a junction).

Δt Time step.

$\boldsymbol{\kappa}$ Thermal conductivity tensor.

$\Phi_{ni,lj}$ Second-order force constant matrix.

\hbar Reduced Planck constant.

κ On-diagonal thermal conductivity component.

ν Phonon mode branch index.

ω Phonon mode frequency.

\mathbf{a} Primitive translation vector.

\mathbf{D} Dynamical matrix.

\mathbf{e} Phonon mode polarization vector.

\mathbf{k} Phonon mode wavevector.

\mathbf{q} Heat vector.

\mathbf{r}_n Lattice vector to unit cell n .

\mathbf{r}_{ni} Equilibrium position of atom i in unit cell n .

\mathbf{v} Velocity.

\mathbf{v}_g Phonon mode group velocity.

\mathbf{x} Position.

A	Cross-sectional area.
G	Thermal conductance.
k_B	Boltzmann constant.
m	Mass.
N	Number of atoms in system or in unit cell.
n_{BE}	Bose-Einstein distribution function.
P	Number of time steps.
q	Heat vector component (e.g., across a junction).
t	Time.
$T, \langle T \rangle$	Thermodynamic temperature.
T^p	Instantaneous temperature at the p^{th} time step.
U, U_{N-N}	Interatomic potential.
V	Volume of unit cell.

Introduction

1.1 Motivation

Technological applications in areas such as microelectronics, solid state lighting, solar energy, and thermoelectrics require heterostructures composed of different crystalline semiconductors and molecules. Tuning the relative length scales and geometric configurations of the constituent materials allows design for specific electronic and electron transport properties in these devices. Their performance, however, is limited by the scattering of electrons with atomic nuclei, which generates heat. The dissipation of this heat is critical to practical device operation, hence, understanding the mechanisms of vibrational thermal transport in such systems is of technological importance [1, 2].

Thermal transport in heterostructured and multi-component systems is determined in large part by the transmission of atomic vibrations across interfaces and junctions formed by the constituent materials, where A the characteristic area of the junction [3]. In a system composed of two different crystals, such as a superlattice, a junction can be an interface between the two crystals [4, 5, 6]. In low-dimensional semiconductor materials such as graphene and hexagonal boron nitride, junctions between the two materials form possible building blocks to band gap graphene devices [7, 8]. In a large unit cell (LUC) crystal, such as face-centered cubic (FCC) C_{60} , the weak effective bond between neighboring C_{60} cages may be treated as a junction [9].

1.2 Objectives

1.2.1 Overview

The thermal transport property of a material can be summarized by its thermal conductivity κ or its thermal conductance G ,

$$\kappa = -\frac{q}{A} \left(\frac{dT}{dx} \right)^{-1} \quad (1.1)$$

$$G = -\frac{q}{A\Delta T}. \quad (1.2)$$

where q is the heat flow through a material, A is its cross-sectional area, T is the temperature field, x is any Cartesian direction, and ΔT is a finite difference in temperature along that direction. Eq. 1.1 is the Fourier law and Eq. 1.2 defines the thermal conductance G . Both are empirical, linear response models relating a temperature difference or temperature gradient to heat flow. Thermal conductivity κ is an intrinsic property, and is best used to describe bulk, homogenous materials. G is an extrinsic property, and is best used to describe objects of finite extent, such as a junction. Both k and G are macroscopic quantities that can be computed from the underlying microscopic dynamics of a solid [10, 11].

The objective of this thesis is to understand thermal transport across junctions between crystalline semiconductors and within C_{60} molecular crystals. We apply molecular dynamics simulations, harmonic lattice dynamics calculations, and mode-resolved scattering boundary method calculations to compute the thermal conductance of junctions between (i) three-dimensional semiconductors and (ii) two-dimensional semiconductors. We also apply molecular dynamics simulations to compute the thermal conductivity of molecular crystals. Our calculations provide fundamental insight into the thermal transport proper-

ties in semiconductors and molecular crystals at the phonon-mode level.

1.2.2 Three-dimensional semiconductor junctions

Three-dimensional semiconductors are widely-used in technological applications such as solid state lighting, microelectronics, and thermoelectric energy conversion. In particular, semiconductor superlattices are popular due to the dependence of their electronic and thermal properties with the superlattice period [5, 6]. We investigate the thermal transport across junctions of 3D semiconductor superlattices. We also identify finite-size effects that arise from both the superlattice period and the overall size of the junction.

1.2.3 Two-dimensional semiconductor junctions

Two-dimensional materials (e.g., graphene) have received considerable research attention due to their unique physical properties. Examples include the quadratic behavior of the phonon dispersion at the Brillouin zone-center and very high thermal and electrical conductivities[12, 13]. Recently, researchers have fabricated heterostructures of graphene and other 2D materials for the purposes of tuning the electronic band gap[14, 15]. We study the transport of phonons across junctions between graphene and hexagonal boron nitride (hBN).

1.2.4 Molecular crystals

Molecular crystals are crystals formed not by atoms but instead by molecules. An example is the C_{60} molecular crystal, where C_{60} molecules arrange themselves in cubic structures. These materials exhibit crystal-like to amorphous-like thermal transport depending on the temperature. The low temperature behavior is like that of an atomic crystal, where plane wave motion of the molecules' centers of mass dominates thermal transport. However, near

room temperature, the individual C_{60} molecules rotate freely about their centers of mass, causing a transition to amorphous-like thermal transport [9, 16]. In order to characterize the effect of the orientational disorder, we will study the thermal conductivity in C_{60} molecular crystals with varying degrees of freedom frozen out.

1.3 Methods

Two atomistic methods will be used for in this work. The first is molecular dynamics simulation, where numerical time integration of the classical equations of motion is used to predict the trajectories of atoms given some initial condition [17]. The second is harmonic lattice dynamics[18], where atoms are assumed to (i) sit at their equilibrium positions and (ii) be coupled to other atoms via harmonic springs. Their dynamics are determined by solving the coupled spring-mass system. While both quantum and classical population distributions can be used in harmonic lattice dynamics, molecular dynamics simulations are inherently classical and cannot account for quantum population effects. This is a limitation of the molecular dynamics method makes it unsuitable for room temperature study of materials with high Debye temperature, where quantum population effects significantly impact the thermal transport properties [19, 20]. In both harmonic lattice dynamics and molecular dynamics, the interaction between atoms must be specified. In molecular dynamics, the interatomic interactions may be fully anharmonic and may come from empirical potentials such as Lennard-Jones[21] or Tersoff [22] or from *ab initio* density functional theory calculations [23, 24]. In harmonic lattice dynamics, the interatomic interactions can only be specified up to the second-order force constant (i.e., the Hooke's law spring constant). These force constants may be taken from either empirical potentials or from DFT calculations. The limitation of harmonic lattice dynamics to second-order force constants limits its ability to describe real crystals, as a phenomenon such as thermal expansion

and finite thermal conductivity within bulk crystals requires the presence of cubic- and higher-order force constants [19, 20]. We overcome this limitation by studying only thermal conductance using the harmonic lattice dynamics approach, where the theory allows prediction of thermal conductance from only second-order force constants.

Both molecular dynamics and harmonic lattice dynamics are applied to study junction thermal conductance in separate ways. With molecular dynamics, we use the direct heat method [25], where a finite heat is applied across the simulation domain and interpolation of the resultant temperature versus position data is used to extract a thermal conductance or thermal conductivity. MD simulation with the direct heat method allows us to capture the finite-temperature effects associated with anharmonic interatomic interactions. With harmonic lattice dynamics, we use the scattering boundary method [26, 27, 28]. Within the scattering boundary method, the junction is assumed to connect two bulk crystalline leads. Bulk vibrational modes (i.e., phonons) of one lead scatter from the junction and are either reflected or transmitted to the other lead, resulting in a transmission coefficient associated with each mode. The total transmitted energy flux is calculated for all modes and is used to compute the thermal conductance. The scattering boundary method has the advantage of providing mode-level detail and allows the use of quantum statistical distributions.

1.4 Overview

The remainder of the thesis is organized as follows. The theoretical foundations of the methods utilized in this thesis are discussed in Chapter 2. The basics of atomistic modeling are discussed. The technique of molecular dynamics is developed, along with the notion of temperature in molecular dynamics. The procedure necessary to perform direct heat molecular dynamics simulation is given. Harmonic lattice dynamics is developed for crystal systems, and the notion of phonon modes and phonons are introduced. Harmonic lattice

dynamics is then coupled to the Landauer formalism and the scattering boundary method for computing junction conductance is developed. Symmetry conditions in the scattering boundary method are considered.

In Chapter 3, superlattice heterostructures of three-dimensional semiconductors are studied using a representative Lennard-Jones system. The thermal conductance of a superlattice junction is calculated as a function of its length using both direct heat molecular dynamics and the scattering boundary method, and compared against a thermal circuit model.

In Chapter 4, heterostructure junctions composed of two-dimensional materials are studied. Specifically, the thermal conductance of various junctions between graphene and hexagonal boron nitride is calculated at a temperature of 300 K. The junction types considered include armchair and zig-zag interfaces, armchair-aligned superlattice junctions, and bilayer junctions. The contributions to the thermal conductance is mapped at a mode-resolved level throughout the first Brillouin zone of graphene.

In Chapter 5, the thermal conductivity of the face-centered cubic C_{60} molecular crystal is calculated using direct heat molecular dynamics simulations. The bonded interactions within individual C_{60} are described by the polymer consistent force field, while intercage interactions are described by a Lennard-Jones potential. Thermal conductivities predicted from full-fidelity simulations are compared to thermal conductivities in simulations where each C_{60} molecule is represented by a point mass, allowing us to quantify the effect of both molecular rotation and intracage vibrations on the thermal conductivity. The point mass interaction is computed by averaging the interaction between two fully defined C_{60} molecules over all angular configurations.

In Chapter 6, the primary contributions of this thesis are summarized and suggested directions for further study are presented.

Theory and methods

2.1 Introduction

In this chapter, we will derive the theoretical underpinnings of and provide practical details for the two major methods used in this thesis: molecular dynamics (MD) simulations and the scattering boundary method (SBM). We show that the methods provide two paths to solving the interacting many-body problem, each under a different set of assumptions. As a result, we are able to use both MD simulation and the SBM to calculate thermal transport properties in different regimes.

In order to study thermal transport in solid materials, it is first necessary to develop a model for the dynamics of the solid. We view a solid as composed of interacting nuclei and electrons which evolve in time under the Hamiltonian

$$H_{\text{Solid}} = H_{\text{Nuclei}} + H_{\text{Electrons}} + H_{\text{N-N}} + H_{\text{E-E}} + H_{\text{N-E}} . \quad (2.1)$$

H_{Nuclei} and $H_{\text{Electrons}}$ are the self-energies of the nuclei and electrons, while $H_{\text{N-N}}$, $H_{\text{E-E}}$, and $H_{\text{N-E}}$ describe their interactions with one another. Since the materials of interest are electrical semiconductors or insulators, the electron contribution to thermal transport is ignored, as are the detailed electron dynamics. Instead, we take the Born-Oppenheimer approximation [20]. That is, we instead recognize that the presence of electrons and their resultant electric fields serve to screen or modify the interactions between nuclei. Hence, instead of considering an interacting many-body quantum system involving both nuclei and electrons, we now have an interacting many-body classical system involving only nuclei.

This simplification leads to the following Hamiltonian

$$H_{\text{Solid}} = H_{\text{Nuclei}} + H_{\text{N-N}}, \quad (2.2)$$

We further assume that the nuclei are well approximated as point masses, and H_{Solid} can be written out explicitly as

$$H_{\text{Solid}}(\mathbf{x}_1, \mathbf{x}_2, \dots, \mathbf{v}_1, \mathbf{v}_2, \dots) = \sum_i^N \frac{1}{2} m_i \mathbf{v}_i^2 + H_{\text{N-N}}(\mathbf{x}_1, \mathbf{x}_2, \dots) \quad (2.3)$$

$$= \sum_i^N \frac{1}{2} m_i \mathbf{v}_i^2 + U(\mathbf{x}_1, \mathbf{x}_2, \dots). \quad (2.4)$$

The \mathbf{x}_i and \mathbf{v}_i are the classical phase space variables representing the positions and velocities of the N nuclei in the system. The first term on the right-hand side is the kinetic energy of the nuclei, where each nucleus is indexed by i and m_i is the mass i^{th} nucleus. The second term on the right-hand side $H_{\text{N-N}}(\mathbf{x}_1, \mathbf{x}_2, \dots) = U(\mathbf{x}_1, \mathbf{x}_2, \dots)$ is the potential energy of the internuclear interactions, which is assumed to be velocity independent. The nuclei are often referred to as atoms and $U(\mathbf{x}_1, \mathbf{x}_2, \dots)$ as the interatomic potential or simply the potential.

Formally, the potential U should include the direct Coulombic interaction between protons, the screening effect of the electrons, and all quantum effects such as exchange interaction. Practically, in a computational framework where we aim to model physical reality as opposed to exactly recreating it, U can range in form from simple analytical pair potentials to interaction parameters computed from first principals density functional theory. In this thesis, we use the following potential types: Lennard-Jones (LJ) [21], Tersoff [22], and Polymer consistent Force Field (PCFF) [29].

2.2 Molecular dynamics simulations

2.2.1 Formulation

The Hamiltonian in Eq. 2.4 is associated with the following set of equations of motion

$$m_i \frac{d\mathbf{v}_i}{dt} = - \frac{\partial U(\mathbf{x}_1, \mathbf{x}_2, \dots)}{\partial \mathbf{x}_i}, \quad (2.5)$$

where t is time and $\partial U/\partial \mathbf{x}_i$ is the force in direction i . The solution of Eq. 2.5 given an initial condition will result in the time evolution (or trajectory) $\{\mathbf{x}(t), \mathbf{v}(t)\}$ of all of the atoms. The trajectory can then be used to extract physically relevant quantities, including thermal transport properties. However, even with the simplifications already made, Eq. 2.4 is still intractable due to two reasons. First, to represent technologically relevant solids, the number of atoms N can range from thousands to numbers on the order of 10^{23} . Second, any form of U more complicated than Hooke's law would make Eq. 2.5 a set of coupled, non-linear, differential equations, which cannot be solved analytically [20].

The first challenge can be overcome by appropriately selecting a small system that is representative of the solid. In this thesis, we focus on charge-neutral crystals, which are well represented by model systems composed of thousands or tens of thousands of atoms. When coupled with the use of periodic boundary conditions, this choice results in a tractable system size.

The second challenge can be overcome by numerically integrating Eq. 2.5. The use of numerical integration to solve for the atomic trajectories in a judiciously chosen model system is MD simulation. MD simulation is a mature technique with many available general-use software packages. In this thesis, the Large-scale Atomic/Molecular Massively Parallel Simulator (LAMMPS) software package [30] is used exclusively to conduct MD simulations.

In a MD simulation, time t is discretized into a sequence $0, t^1, \dots, t^p$, where $t^p = p\Delta t$ and Δt is the time step. An initial state in phase space is specified as $\{\mathbf{x}_i(0), \mathbf{v}_i(0)\}$ and the evolution in phase space at future times $\{\mathbf{x}_i(t), \mathbf{v}_i(t)\}$ is approximated by discrete sequences $\{\mathbf{x}_i^p, \mathbf{v}_i^p\}$, where the simulation trajectory \mathbf{x}_i^p is an approximation of the physical trajectory $\mathbf{x}_i(t^p)$. In the limit as $\Delta t \rightarrow 0$, the phase space sequence approaches the physical phase space trajectory, $\{\mathbf{x}_i^p, \mathbf{v}_i^p\} \rightarrow \{\mathbf{x}(t), \mathbf{v}(t)\}$. Practically, it is impossible to make Δt infinitesimal, and the choice of Δt depends on the characteristics of the interaction potential U . Δt is usually chosen to be five to ten times smaller than the period associated with the highest frequency oscillation present in U . Trial and error is then used to pinpoint the appropriate time step. A properly chosen Δt will result in energy conservation to five or six significant figures during the MD simulation with no drift in the mean energy. The choice of time step is critical to MD simulations. Too large a time step will cause $\{\mathbf{x}_i^p, \mathbf{v}_i^p\}$ to diverge from $\{\mathbf{x}(t), \mathbf{v}(t)\}$ and result in an MD simulation that does not represent the classical equations of motion. Too small a time step will make the simulation unnecessarily long in terms of computational time.

In addition to the choice of time step, the algorithm used to predict $\{\mathbf{x}_i^{p+1}, \mathbf{v}_i^{p+1}\}$ from $\{\mathbf{x}_i^p, \mathbf{v}_i^p\}$ (e.g., the numerical integration scheme) must also be specified. In LAMMPS, the explicit velocity Verlet algorithm is used. The algorithm goes as follows

$$\mathbf{x}_i^{p+1} = \mathbf{x}_i^p + \mathbf{v}_i^p \Delta t + \frac{1}{2} \frac{d\mathbf{v}_i^p}{dt} \Delta t^2 \quad (2.6)$$

$$\mathbf{v}_i^{p+1} = \mathbf{v}_i^p + \frac{1}{2} \left[\frac{d\mathbf{v}_i^p}{dt} + \frac{d\mathbf{v}_i^{p+1}}{dt} \right] \Delta t. \quad (2.7)$$

In Eqs. 2.6 and 2.7, $d\mathbf{v}_i^p/dt$ and $d\mathbf{v}_i^{p+1}/dt$ are defined according to Eq. 2.5. More details regarding MD simulations can be found in Ref [17].

2.2.2 Temperature in MD

In order to predict thermal transport properties from MD simulations, it is necessary to connect the phase space trajectories $\{\mathbf{x}_i^{p+1}, \mathbf{v}_i^{p+1}\}$ that are calculated by the simulation to the temperature. The instantaneous temperature T^p of a group of N atoms in a three-dimensional MD simulation is given by

$$T^p = \frac{2}{3Nk_B} \sum_{i=1}^N \frac{1}{2} m_i \mathbf{v}_i^{p2}, \quad (2.8)$$

where k_B is the Boltzmann constant and the summation on the right-hand side is the kinetic energy of that group of atoms. Eq. 2.8 is based on the definition of temperature in the kinetic theory of gasses. Two assumptions are made. First, we assume that the classical equipartition theorem holds and each quadratic degree of freedom has a heat capacity of $k_B/2$. Second, in terms of temperature computation, atoms in an MD simulation behave as a non-interacting ideal gas just as in the kinetic theory of gasses. While U is not only non-zero, but also has terms beyond quadratic order in most MD simulations, the definition of temperature given in Eq. 2.8 is one that is convenient to compute and well-established in the literature. The thermodynamic temperature $\langle T \rangle$ of a group of atoms in an MD simulation can then be defined as the time-average of the instantaneous temperature over long time

$$\langle T \rangle = \frac{1}{P} \sum_{p=0}^P T^p. \quad (2.9)$$

While formally $\langle T \rangle$ should be computed as an ensemble average over the phase space variables, it is assumed that the system is ergodic, and that time averaging is equivalent to phase space averaging. Often times, the same system is initiated from many initial conditions and the simulations are averaged together for faster convergence of $\langle T \rangle$ and other thermodynamics quantities.

2.2.3 Direct heat MD simulation

Once temperature is defined within the framework of an MD simulation, it is possible to conduct a “computational experiment” by which thermal transport properties can be extracted in direct analogy to an experiment in a laboratory. The empirical Fourier law, introduced in one-dimensional form in Eq. 1.1, relates the gradient in temperature field T to the heat \mathbf{q} flowing across a cross-section of area A

$$\mathbf{q} = -\boldsymbol{\kappa}A \nabla_{\mathbf{x}} T \quad (2.10)$$

via $\boldsymbol{\kappa}$, the thermal conductivity tensor [10]. $\boldsymbol{\kappa}$ is only non-zero on the diagonal elements, indicating that heat always flows in the same direction as the temperature gradient. It is often more convenient to write individual equations for each of the on-diagonal elements. Let κ^α represent the $\alpha - \alpha$ component of thermal conductivity and let the related thermal conductance G^α be a property that relates heat flow in the α direction to a finite difference in temperature, also along the α direction (on occasions when there are no ambiguities, the α superscript is dropped). The Fourier law can be written along a specific direction as

$$q^\alpha = -\kappa^\alpha A \frac{dT}{dx^\alpha} \quad (2.11)$$

$$q^\alpha = -G^\alpha A \Delta^\alpha T . \quad (2.12)$$

Eq. 2.11 defines the intrinsic material property of thermal conductivity κ^α and is most appropriate to describe bulk or homogenous materials. Eq. 2.12 defines the thermal conductance of a single object with finite spatial extent and is most appropriate to describe interfaces or junctions between bulk materials. In both Eqs. 2.11 and 2.12, x^α is the α^{th} Cartesian direction, q^α is the heat flux normal to the x^α direction, and A is the area normal to the x^α direction. $\Delta^\alpha T$ is the finite change in the temperature profile along the

x^α direction usually defined across an object of interest, such as an interface. In order to extract κ^α or G^α from an MD simulation, we create an atomistic representation of the material, impose a heat flux within the material, run the MD simulation until the system is at steady state, and extract the resultant temperature profile using the method discussed in Sec. 2.2.2. Eqs. 2.11 and 2.12 are then applied to the temperature profile to extract κ^α or G^α . This technique is the direct heat method, and is a steady-state, non-equilibrium method of computing κ^α and G^α from MD simulation [25, 31]. It is also referred to simply as non-equilibrium MD (NEMD).

For clarity, assume that the direction x^α in Eqs. 2.11 and 2.12 is z . Since the direction of interest is usually apparent, the superscript z will be left out of κ and G . The simulation cell has fixed boundary conditions along the z -direction, but is periodic along the x and y . The sample is a collection of atoms that has a length L along the z -direction and cross-sectional area A normal to the z -direction. At $z = 0$ and $z = L$, layers of fixed atoms are placed that interact with the remainder of the sample, but themselves have no dynamics. They exist to prevent the sample from sublimating. In LAMMPS, the fixed atoms can be created with the `fix setforce` command. The fixed atoms remain so for the entirety of the simulation and are excluded from the discussion from this point forward. Immediately adjacent to the fixed atoms are the reservoir atoms. Without loss of generality, the reservoir atoms near $z = 0$ form the hot reservoir, while the reservoir atoms near $z = L$ form the cold reservoir.

Since both κ and G are temperature-dependent quantities, the MD simulation is initiated by scaling the velocities of all atoms so that the overall distribution of atomic velocities corresponds to that of the Maxwell-Boltzmann velocity distribution at the desired temperature T [32]. At every time step, the velocities of the atoms are artificially rescaled so that

their distribution is

$$D(v_\alpha) \propto \exp\left(\frac{\bar{m}v^{\alpha 2}}{2k_{\text{B}}T}\right) \quad (2.13)$$

up to a normalization factor. \bar{m} is the average atomic mass of the system and the index α ranges over the three Cartesian coordinates. Following the initial scaling of the velocities, the velocities are rescaled at every time step according to the difference between the actual instantaneous temperature and the target instantaneous temperature. This rescaling is not done from a distribution, but is rather performed by computing the difference from the target kinetic energy for the entire system, and adding or subtracting an even amount of kinetic energy from each atom. Velocity rescaling is performed for P_{Rescale} time steps, and can be accomplished in LAMMPS using the `fix temp/rescale` command.

While velocity rescaling allows the entire system to come close to the correct temperature in a short number of time steps, it is artificial and disruptive when compared to the energy-conserving dynamics described by Eq. 2.5. In addition, it may not achieve the desired equilibrium Maxwell-Boltzmann velocity distribution. Instead, the Nose-Hoover thermostat [33], a less disruptive method of achieving thermal equilibrium, is used following the rescaling for $P_{\text{N-H}}$ time steps. The Nose-Hoover thermostat alters the equations of motion given in Eq. 2.5 to

$$m_i \frac{d\mathbf{v}_i}{dt} = -\frac{\partial U}{\partial(\mathbf{x}_1, \mathbf{x}_2, \dots)} \mathbf{x}_i + \eta(T)\mathbf{v}_i(t). \quad (2.14)$$

The velocity-dependent second term on the right-hand side of Eq. 2.14 represents the interaction of the system with a large bath at temperature T . The strength of the interaction and the temperature of the bath is determined by the damping parameter $\eta(T)$. The aim of the Nose-Hoover thermostat is to alter the dynamics of the atoms as to emulate the existence of equilibrium in the canonical ensemble. Specifically, it aims to match the fluc-

tuations in the system’s kinetic energy to that of the canonical ensemble. When Eq. 2.14 is integrated, the system is gradually brought into thermal equilibrium at temperature T . Nose-Hoover requires more time steps than velocity rescaling but produces a more stable equilibrium velocity distribution, hence it is used for fine temperature adjustment after velocity rescaling. The Nose-Hoover thermostat can be activated in LAMMPS using the `fix nvt` command. Following the Nose-Hoover thermostat, the equations of motion are returned to those in Eq. 2.5, and the system is evolved in an energy-conserving manner for P_{Relax} time steps (accessible in LAMMPS using the `fix nve` command).

After the system is at thermal equilibrium at temperature T , the transient portion of the simulation begins. For the next $P_{\text{Transient}}$ time steps, a heat flux is imposed in the sample along the z direction by removing ΔE from the kinetic energy of the cold reservoir and adding ΔE to the kinetic energy of the hot reservoir at every time step. Doing so conserves the total energy in the system, but establishes a heat flow

$$q^z = \frac{\Delta E}{\Delta t} . \tag{2.15}$$

Establishing the heat flow be accomplished in LAMMPS using the command `fix heat` twice in succession, once to remove heat and once to add heat. Throughout this period, apart from the addition and subtraction of heat from the reservoirs, the entire sample is evolved according to Eq. 2.5.

Following the transient period, the system is at steady state and the data collection portion begins. During this portion, no changes are made to the simulation dynamics. Since the objective is to extract either dT/dz or $\Delta_z T$, it is necessary to divide the sample into groups of atoms according to their position in the z -direction. If the sample is crystalline, a natural grouping would be crystal planes normal to the z -direction. For each atomic group (corresponding with an average z location), the temperature $T(z)$ is calculated

using Eq. 2.8 and recorded. To avoid excessive data output, it is best to create running averages of temperature that are rarely output. This is achievable in LAMMPS using the `fix ave/time` command. After data output is performed for $P_{\text{Collection}}$ time steps, the simulation concludes. A linear fit to the extracted temperature profiles $T(z)$ can be used to extract k according to Eq. 2.11. Likewise, G can be extracted by inspection according to Eq. 2.12.

The choice of system size parameters L and A , the choice of heat q_z , as well as the time steps necessary for each portion of the simulation P_{Rescale} , $P_{\text{N-H}}$, P_{Relax} , $P_{\text{Transient}}$, and $P_{\text{Collection}}$ are critical to the success of the simulation. A should be chosen so that the center-to-edge dimension on a plane normal to z at least exceeds the cut-off distance of the interaction potential U . Convergence can be performed in both L and A so that the predicted k or G is invariant to changes in the system size. If convergence cannot be achieved within tractable system sizes, extrapolation may be necessary. Similarly, the predicted k or G should be invariant to changes in q^z . Typically, q^z should be selected so that the overall change in temperature across the sample is no more than 10% of the average system temperature T . Further, q^z should not be made so large that the temperature profile $T(z)$ becomes non-linear. Non-linearities in $T(z)$ are often times unavoidable near the hot and cold reservoirs, as the addition and subtraction of ΔE at each time step is physically artificial. Linear fits to $T(z)$ should avoid portions near the reservoir where non-linearities are present. $P_{\text{Transient}}$ must be chosen to be large such that the system is at steady state prior to data collection. $P_{\text{Transient}}$ depends on the thermal diffusivity of the sample, but since that is often times unknown, $P_{\text{Transient}}$ must be determined by trial and error. Though parameters will vary for different systems, $P_{\text{Rescale}} = P_{\text{N-H}} = P_{\text{Relax}} = 200,000$, $P_{\text{Transient}} = 1 \times 10^7$ and $P_{\text{Collection}} = 3 \times 10^6$ serve as good starting points. The workflow for direct head MD simulations is summarized in Fig. 2.1.

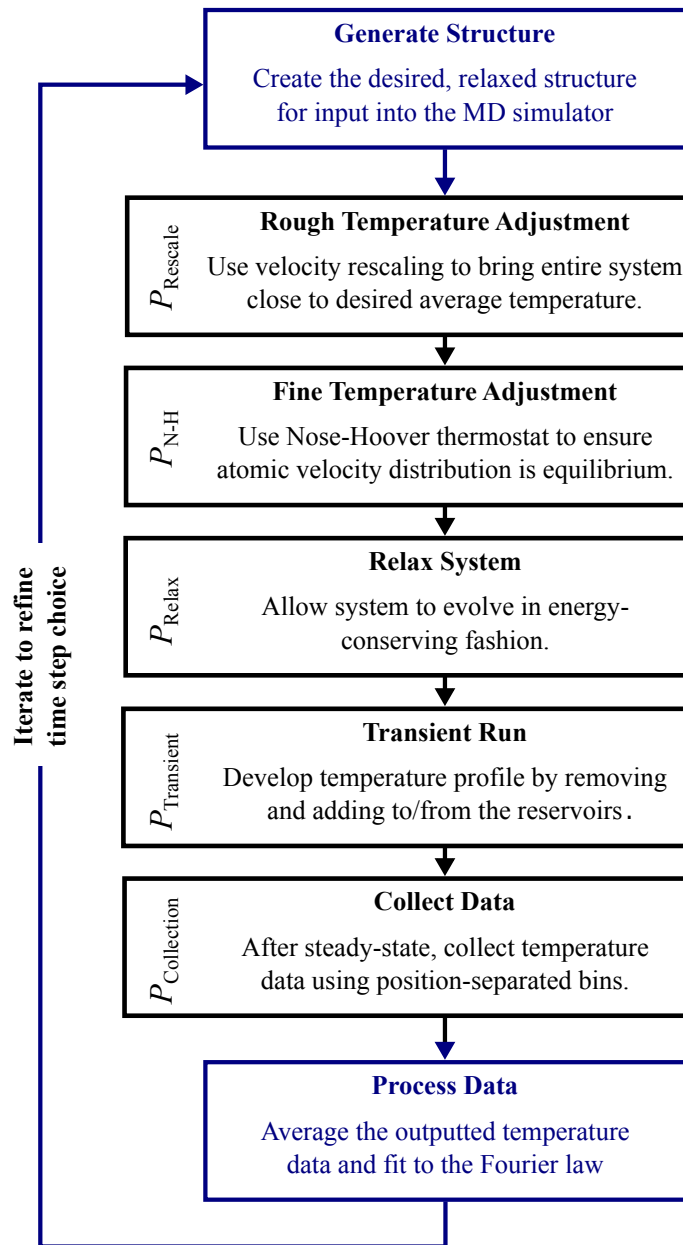


Figure 2.1: Workflow for direct heat MD simulations. Blue boxes indicate pre- and post-simulation tasks, while black boxes indicate tasks completed within the MD simulation program.

2.3 Harmonic lattice dynamics calculations

2.3.1 Formulation

While MD simulations are a robust method of overcoming the difficulties associated with Eq. 2.5, an alternate method known as harmonic lattice dynamics (HLD) is applicable to solids that are crystalline. A crystal is an infinite periodic arrangement of unit cells (UCs), where each UC contains atoms that have equilibrium positions fixed relative to the origin of the UC. The dynamics of the atoms involve only small deviations away from the equilibrium positions. Since a perfect crystal is both infinite in extent and perfectly periodic, no real material is exactly described by this model, however, it provides a very useful starting point.

Previously in Eq. 2.4, each atom was assigned an index i that ranged up to N , the total number of atoms in the system. In a crystal, the total number of atoms is infinite and this indexing scheme is not useful. Instead, the index i will range only through the atoms within a single UC, while N represents the total number of atoms in a UC. In a three-dimensional crystal, the UC is replicated endlessly throughout space in a periodic fashion via three primitive translation vectors \mathbf{a}_1 , \mathbf{a}_2 , and \mathbf{a}_3 , such that any integer linear combination of the translation vectors gives the origin of a UC, called a lattice vector. Each UC will be given a single index n or l (one can imagine that as the countably infinite UCs are built up from the translation vectors, each one is assigned a countably infinite index). The n^{th} lattice vector (or equivalently the origin of the n^{th} UC) \mathbf{r}_n is

$$\mathbf{r}_n = a\mathbf{a}_1 + b\mathbf{a}_2 + c\mathbf{a}_3, \quad (2.16)$$

where a , b and c are integers (the exact mapping from a , b , and c to n is irrelevant). Since each UC is indistinguishable from the next, any arbitrary lattice vector may be selected as

the origin and be referred to as the central cell. The equilibrium position of the i^{th} atom within the n^{th} UC will be denoted as \mathbf{r}_{ni} . Since atoms are assumed to deviate slightly from their equilibrium positions, the variable $\mathbf{x}_{ni}(t)$ is now the time-dependent deviation of the i^{th} atom in the n^{th} UC from its equilibrium position. The \mathbf{x}_{ni} differ from the \mathbf{x}_i used in Sec. 2.2 only by a translation \mathbf{r}_n , and hence make equally valid phase space variables. The velocities \mathbf{v}_{ni} do not differ from \mathbf{v}_i , as the UC origins \mathbf{r}_n do not move in time.

In addition to assuming the existence of a periodic lattice, we also assume that the interatomic potential U is harmonic, that is, U is at most quadratic in the phase space variables. This is akin to assuming that the interactions between atoms are governed by Hooke's law springs. The equations of motion in Eq. 2.5 are modified to

$$m_i \frac{d\mathbf{v}_{ni}}{dt} = -\Phi_{ni,lj} \mathbf{x}_{lj}, \quad (2.17)$$

where $\Phi_{ni,lj}$ is the matrix of second-order force constants between atom i in unit cell n and atom j in unit cell l . It is best to define $\Phi_{ni,lj}$ by its α - β matrix elements $\Phi_{ni,lj}^{\alpha\beta}$ individually.

$$\Phi_{ni,lj}^{\alpha\beta} = \frac{\partial^2 U}{\partial x_{ni}^\alpha \partial x_{lj}^\beta}, \quad (2.18)$$

where U is the interatomic potential in Eq. 2.5. The commutativity of the two partial differentiations in Eq. 2.18 ensures that $\Phi_{ni,lj}$ is Hermitian (e.g., self-conjugate). This is a consequence of Newton's third law. Using $\Phi_{ni,lj}^{\alpha\beta}$, it is possible to write Eq. 2.17 as scalar equations involving the individual Cartesian components of $\mathbf{x}_{n,i}$

$$m_i \frac{dv_{ni}^\alpha}{dt} = - \sum_{l,j} \Phi_{ni,lj}^{\alpha\beta} x_{lj}^\beta. \quad (2.19)$$

In Eq. 2.19, the summation is performed over all atoms j in all unit cells l . v_i^α , and x_j^β

represent the α and β Cartesian components of the velocity and position vectors of the i^{th} and j^{th} atoms. The assumption of harmonic interactions ensures that no non-linear terms can appear in the equations of motion Eq. 2.19. Indeed, Eq. 2.19 now represents a set of coupled, homogenous, linear, second-order, ordinary differential equations that are exactly solvable. The numerical integration used in MD simulation (see Sec. 2.2.1) is no longer necessary, and we proceed with an analytical solution. We make the ansatz that the \mathbf{x}_{ni} evolve periodically in time so that

$$x_{ni}^{\alpha}(t) = \frac{1}{\sqrt{m_i}} u_{ni}^{\alpha} \exp(-i\omega t), \quad (2.20)$$

where ω is the frequency of oscillation, i is the imaginary unit, and \mathbf{u}_{ni} is the time-independent portion of \mathbf{x}_{ni} . The factor $1/\sqrt{m_i}$ on the right-hand side is placed for symmetry later in the derivation. Substitution of Eq. 2.20 into Eq. 2.19 results in

$$\omega^2 u_{ni}^{\alpha} = \sum_{l,j} \frac{1}{\sqrt{m_i m_j}} \Phi_{ni,lj}^{\alpha\beta} u_{lj}^{\beta}. \quad (2.21)$$

The equations have been transformed from a set of coupled differential equations (Eq. 2.19) to a set of coupled difference equations (Eq. 2.21). However, because the index n must range over the countably infinite UCs in a crystal, Eq. 2.21 represents an infinite set of difference equations. Fortunately, the periodicity of the crystal allows us to reduce the dimensionality of the problem from infinite to $3N$ (e.g., three times the number of atoms in a UC). We make another ansatz stating that \mathbf{u}_{ni} must be spatially periodic in the lattice vectors \mathbf{r}_n , in accordance to the periodicity of the crystal

$$u_{ni}^{\alpha} = e_i^{\alpha} \exp(i\mathbf{k}^* \mathbf{r}_n). \quad (2.22)$$

\mathbf{k} is the spatial frequency or wavevector and \mathbf{e}_i is the portion of \mathbf{u}_{ni} that is independent of the UC position. \mathbf{r}_n is any lattice vector (see Eqn. 2.16). Furthermore, because all UCs are identical, the force constant matrix must depend only on the difference between lattice vectors, and not their absolute positions

$$\Phi_{ni,lj}^{\alpha\beta} = \Phi_{ij}^{\alpha\beta}(\mathbf{r}_l - \mathbf{r}_n). \quad (2.23)$$

Substitution of Eqs. 2.22 and 2.23 into Eq. 2.21 results in

$$\omega^2 e_i^\alpha = \sum_j \frac{1}{\sqrt{m_i m_j}} \left[\sum_l \Phi_{ij}^{\alpha,\beta}(\mathbf{r}_l - \mathbf{r}_n) \exp[(i\mathbf{k}^\dagger(\mathbf{r}_l - \mathbf{r}_n))] \right] e_j^\beta, \quad (2.24)$$

which is a set of $3N$ difference equations. The quantity within the square brackets on the right-hand side of Eq. 2.24 is the wavevector-dependent dynamical matrix. Without loss of generality, we choose UC n to be the central cell such that $\mathbf{r}_n = \mathbf{0}$. The elements of the dynamical matrix $D_{ij}^{\alpha\beta}$ then can be written in the illustrative form

$$D_{ij}^{\alpha\beta}(\mathbf{k}) = \frac{1}{\sqrt{m_i m_j}} \sum_l \Phi_{ij}^{\alpha\beta}(\mathbf{r}_l) \exp(i\mathbf{k}^\dagger \mathbf{r}_l). \quad (2.25)$$

Eq. 2.25 reveals that the dynamical matrix is the discrete spatial Fourier transform of the force constant matrix $\Phi_{ij}^{\alpha\beta}$ from the lattice vector variable \mathbf{r}_l to the wavevector variable \mathbf{k} . While the summation over l should formally cover UCs very far from the central UC (e.g., $\mathbf{r}_l \rightarrow \infty$), potentials U used for non-ionic dielectric solids go to zero at finite distance due to cut-offs. Hence, $\Phi_{ij}^{\alpha\beta}(\mathbf{r}_l)$ goes to zero for $|\mathbf{r}_l|$ greater than the cut-off distance of U and the Fourier transform summation is convergent. In practice, the summation can simply be truncated at the cut-off distance without loss of fidelity.

$D_{ij}^{\alpha\beta}$ can be composed into 3×3 pairwise dynamical submatrices \mathbf{D}_{ij} that describe the

interaction between atoms i and j within a unit cell

$$\mathbf{D}_{ij}(\mathbf{k}) = \begin{bmatrix} D_{ij}^{11} & \dots & D_{ij}^{13} \\ \vdots & \ddots & \vdots \\ D_{ij}^{3,1} & \dots & D_{ij}^{33} \end{bmatrix}. \quad (2.26)$$

Using the notation in Eq. 2.25, Eq. 2.24 can be rewritten compactly as

$$\omega^2 e_i^\alpha = D_{ij}^{\alpha\beta}(\mathbf{k}) e_j^\beta. \quad (2.27)$$

If we concatenate the elements e_i^α to form a $3N$ -dimensional vector describing the time- and lattice vector-independent displacements of an entire UC (called the polarization vector)

$$\mathbf{e} = [e_1^1, e_1^2, e_1^3, e_2^1, \dots, e_N^3] \quad (2.28)$$

and similarly concatenate the 3×3 pairwise dynamical submatrices \mathbf{D}_{ij} into the $3N \times 3N$ dynamical matrix \mathbf{D}

$$\mathbf{D}(\mathbf{k}) = \begin{bmatrix} \mathbf{D}_{11} & \dots & \mathbf{D}_{13} \\ \vdots & \ddots & \vdots \\ \mathbf{D}_{31} & \dots & \mathbf{D}_{33} \end{bmatrix}, \quad (2.29)$$

we can rewrite Eq. 2.25 as

$$\mathbf{D}(\mathbf{k}) \mathbf{e} = \omega^2 \mathbf{e}, \quad (2.30)$$

which is a $3N \times 3N$ Hermitian eigenvalue problem where the squared frequencies ω^2 are the eigenvalues and the UC complex polarization vectors \mathbf{e} are the eigenvectors. Due to the hermiticity of \mathbf{D} , the eigenvectors \mathbf{e} are of unit norm such that $\mathbf{e}^\dagger \mathbf{e} = 1$. Eq. 2.30 can be solved using any hermitian eigenvalue solver. The open source C++ library Eigen [34] was used for all data presented in this thesis, while ScaLAPACK [35] is a parallelized but

less user-friendly alternative.

Solution of Eq. 2.30 at a given \mathbf{k} produces $3N$ eigenvector-eigenvalue pairs $[\mathbf{e}(\mathbf{k}), \omega(\mathbf{k})]_\nu$, where the branch index ν ranges through all pairs. Each pair corresponds to a plane wave solution to the equations of motion (Eq. 2.17) of the form

$$\mathbf{x}_{\mathbf{k},\nu}(\mathbf{r}, t) = \mathbf{e}(\mathbf{k}, \nu) \exp [\mathbf{i}\mathbf{k}^\dagger \mathbf{r} - \mathbf{i}\omega(\mathbf{k}, \nu)t] , \quad (2.31)$$

where \mathbf{x} is the time- and lattice vector-dependent atomic displacement from equilibrium for an entire UC (e.g., $\mathbf{x} = [\mathbf{x}_{n1}, \mathbf{x}_{n2}, \dots, \mathbf{x}_{nN}]$ for any n). Solutions of the form given in Eq. 2.31 are called phonon modes. Due to the linearity of Eq. 2.17, any solution can be written as a complex-coefficient linear combination of phonon modes, so that the general solution of Eq. 2.17 is

$$\mathbf{x}_{\text{General}}(\mathbf{r}, t) = \int_{\text{FBZ}} d\mathbf{k} \sum_{\nu=1}^{3N} A(\mathbf{k}, \nu) \mathbf{e}(\mathbf{k}, \nu) \exp [\mathbf{i}\mathbf{k}^\dagger \mathbf{r} - \mathbf{i}\omega(\mathbf{k}, \nu)t] , \quad (2.32)$$

where the coefficients $A(\mathbf{k}, \nu)$ can be selected to suit any initial condition. Eq. 2.32 indicates that the phonon modes form a complete basis for the dynamics of a crystal. Instead of integrating the equations of motion as in MD simulation, the objective of an HLD calculation is to determine all the phonon modes of a system. Unlike continuous systems, the range of \mathbf{k} required for the phonon modes to be complete basis is not infinite but is instead a finite region in \mathbf{k} -space called the first Brillouin zone (FBZ). The geometric configuration of the FBZ differs for different configurations of crystal. More information can be found in Refs. [18, 19, 20].

Since all phonon modes are plane waves (Eq. 2.31), properties attributed to systems described by wave equations can also be attributed to crystals. Specifically, the dispersion

relation $\omega(\mathbf{k}, \nu)$, and the related group velocity $\mathbf{v}_g(\mathbf{k}, \nu)$

$$\mathbf{v}_g(\mathbf{k}, \nu) = \nabla_{\mathbf{k}} \omega(\mathbf{k}, \nu) \quad (2.33)$$

are of great importance. The group velocity is the propagation velocity of a wave packet composed of many phonon modes. More importantly, it is the velocity at which energy propagates, and hence is used as the velocity of phonon modes for the purposes of energy flux computation in particle models of phonon transport.

2.3.2 Temperature in HLD

Before thermal transport properties within crystals can be discussed, the notion of temperature must be introduced into the HLD/phonon mode framework. To do this, we must quantize the classical derivation presented in Sec. 2.3.1 and introduce the individual phonon, which is the quasi-particle representing one quantum of energy within a phonon mode.

The procedure of second quantization is applied to the Hamiltonian in Eq. 2.4, which, under the HLD assumptions, becomes

$$H_{\text{HLD}} = \sum_{n,i} \frac{p_{ni}^2}{2m_i} + \sum_{n,i} \sum_{j,l} \Phi_{ni,jl} \mathbf{x}_{ni} \mathbf{x}_{jl}. \quad (2.34)$$

The derivation involves performing spatial Fourier transforms similar to what is done in Sec. 2.3.1 and introducing creation and annihilation operators for each phonon mode. Details of the diagonalization of a quantum one-dimensional crystal can be found in Appendix B. Details of the complete derivation of phonons from quantum mechanics can be found in most solid state physics textbooks [20], but is particularly clear in Refs. [36, 37]. The quantization of the electromagnetic field shares many similarities with the second

quantization of phonons, and can be found, for example, in Ref. [38].

Each phonon mode is revealed to behave as independent quantum harmonic oscillators, thus the energy of each phonon mode is given by the quantum harmonic oscillator eigenvalue spectrum

$$E(\mathbf{k}, \nu) = \hbar\omega(\mathbf{k}, \nu) \left[n(\mathbf{k}, \nu) + \frac{1}{2} \right], \quad (2.35)$$

where \hbar is the reduced Planck constant, $\omega(\mathbf{k}, \nu)$ is the frequency of the phonon mode as in Eq. 2.30 [20]. $n(\mathbf{k}, \nu)$ is the occupation number, representing the number of phonons in the phonon mode at \mathbf{k} and ν . Phonons are bosons, thus it is possible for each phonon mode to contain a unlimited number of phonons. Further, it is possible to define temperature in the context of the crystal system using Bose-Einstein statistics. For a crystal in thermal equilibrium at temperature T , the occupation number $n(\mathbf{k}, \nu)$ depends only on the phonon mode frequency $n(\mathbf{k}, \nu) = n(\omega(\mathbf{k}, \nu))$ and is given by the Bose-Einstein distribution n_{BE}

$$n_{\text{BE}}(T, \mathbf{k}, \nu) = \frac{1}{\exp \left[\frac{\hbar\omega(\mathbf{k}, \nu)}{k_{\text{B}}T} \right] - 1}. \quad (2.36)$$

Combining Eq. 2.36 with Eq. 2.35, the energy of a crystal at temperature T is

$$E_{\text{Crystal}}(T) = \int_{\text{FBZ}} d\mathbf{k} \sum_{\nu=1}^{3N} \hbar\omega(\mathbf{k}, \nu) \left[n_{\text{BE}}(T, \omega(\mathbf{k}, \nu)) + \frac{1}{2} \right]. \quad (2.37)$$

2.3.3 Crystal thermal conductivity

Phonons as introduced in Sec. 2.3.2 allow more parallels to be drawn between crystals and the kinetic theory of gasses. If phonons are thought of as particles that travel at their group velocity $\mathbf{v}_{\text{g}}(\mathbf{k}, \nu)$ and carry energy $\hbar\omega(\mathbf{k}, \nu)$, then we can define the heat \mathbf{q} in the

phonon basis and rewrite the Fourier law (Eq. 2.10) for crystals as

$$\frac{1}{V} \int_{\text{FBZ}} d\mathbf{k} \sum_{\nu=1}^{3N} \hbar\omega(\mathbf{k}, \nu) \mathbf{v}_g(\mathbf{k}, \nu) n(\mathbf{k}, \nu) = -\boldsymbol{\kappa} \nabla_{\mathbf{x}} T, \quad (2.38)$$

where V is the volume of a UC. Note that $n(\mathbf{k}, \nu)$ is not the equilibrium Bose-Einstein distribution, since the introduction of a temperature gradient moves the crystal out of equilibrium. The task of computing $\boldsymbol{\kappa}$ involves solving for the steady-state non-equilibrium distribution function $n(\mathbf{k}, \nu)$ under an applied temperature gradient. This can be done by modeling the phonon particle dynamics using the Boltzmann transport equation

$$\mathbf{v}_g(\mathbf{k}, \nu)^\dagger \nabla_{\mathbf{x}} n(\mathbf{k}, \nu) = \left[\frac{\partial n(\mathbf{k}, \nu)}{\partial t} \right]_{\text{Coll}}. \quad (2.39)$$

The partial derivative on the right-hand side of Eq. 2.39 accounts for changes to $n(\mathbf{k}, \nu)$ due to scattering of phonons. For the perfect crystal described in Sec. 2.3.1, phonons do not scatter. However, the perfect crystal must be modified to better describe real crystals. In doing so, the finite boundaries of the crystal cause boundary scattering. Impurities and defects are also a source of scattering. The presence of terms in the interatomic potential U of cubic and greater order in the phase space variables causes anharmonic or phonon-phonon scattering. These deviations away from the perfect crystal cause the phonon modes (Eq. 2.31) to decay in time into other phonon modes. The central challenge in solving Eq. 2.39 is to solve for the phonon scattering dynamics with all possible sources. This technique is called anharmonic lattice dynamics (ALD) and is done by introducing boundaries, impurities, anharmonicity, etc., as perturbations to the perfect crystal. More information on the practical application of ALD to research topics can be found in Refs. [39, 40, 41]. For pedagogical treatment of phonon-phonon interactions, Ref. [42] and [43] are invaluable. Discussion of phonon transport is best in the classical text by Ziman [44],

but is also covered in the survey text Ref. [11]. Since most of phonon transport theory is based on analogues to the kinetic theory of gasses, Reif [32] is a good reference for classical thermodynamics and transport.

2.4 Scattering boundary method

2.4.1 Landauer formalism

While ALD as discussed in Sec. 2.3.3 provides a framework for calculating the thermal conductivity κ of a crystal, the Landauer formalism allows the calculation of thermal conductance G of junctions connecting crystals. The physical picture provided by the Landauer formalism is akin to that of the kinetic theory of gasses. Suppose that a junction joins two bulk crystals L and R, and that the center of the junction is located at $z = 0$. Though the junction has finite spatial extent, as $z \rightarrow -\infty$, we approach a pure crystal of type L, called the left lead. Similarly, as $z \rightarrow \infty$, we approach a pure crystal of type R, called the right lead. Since the leads are very far away from the junction, the phonon picture as described in Sec. 2.3 is a valid and complete description of the lead dynamics. Much like in Sec. 2.3.3, the lead phonons behave as particles that travel at their group velocities $\mathbf{v}_g(\mathbf{k}, \nu)$, each carrying energy $\hbar\omega(\mathbf{k}, \nu)$. The leads L and R are held at equilibrium separately at temperatures T_L and T_R . Without loss of generality, assume that $T_L > T_R$ such that the net heat across the junction is

$$q_{\text{Net}} = q_{L \rightarrow R} + q_{R \rightarrow L}, \quad (2.40)$$

where the L to R heat $q_{L \rightarrow R}$ and the R to L heat $q_{R \rightarrow L}$ are defined as

$$q_{L \rightarrow R}(T_L) = \frac{1}{V_L} \int_{\text{FBZ}_L} d\mathbf{k} \sum_{\nu}^{+z} \hbar\omega_L(\mathbf{k}, \nu) \mathbf{v}_{g,L}(\mathbf{k}, \nu)^\dagger \hat{\mathbf{z}} n_{\text{BE}}(T_L, \mathbf{k}, \nu) \alpha_{L \rightarrow R}(\mathbf{k}, \nu) \quad (2.41)$$

$$q_{R \rightarrow L}(T_R) = \frac{1}{V_R} \int_{\text{FBZ}_R} d\mathbf{k} \sum_{\nu}^{-z} \hbar\omega_R(\mathbf{k}, \nu) \mathbf{v}_{g,R}(\mathbf{k}, \nu)^\dagger \hat{\mathbf{z}} n_{\text{BE}}(T_R, \mathbf{k}, \nu) \alpha_{R \rightarrow L}(\mathbf{k}, \nu). \quad (2.42)$$

Subscripts of L and R in Eqs. 2.41 and 2.42 indicate summation over the respective FBZs of the two leads, while the limits of the summation on the right-hand sides indicate only phonons traveling in the positive z (negative z) direction are considered for crystal L (R). Only the z -components of group velocity are considered. Eqs. 2.41 and 2.42 differ slightly from the heat as defined in Eq. 2.38 by the addition of the transmission coefficient $\alpha_{L \rightarrow R}$ ($\alpha_{R \rightarrow L}$) on side L (side R). The transmission coefficient ranges from zero to unity and is a property of the junction describing the fraction of phonons at phonon mode \mathbf{k} and ν that transmit across the junction. The Landauer formalism was originally developed for electron transport [45]. Ref. [46] gives a thorough survey of both the Landauer formalism and other formalisms in the context of electron transport, which has many parallels with phonon transport. Ref. [11] discusses Landauer specifically in the context of phonon transport.

In the case that $T_L = T_R = T$, q_{Net} must vanish, hence $q_{L \rightarrow R}(T) = -q_{R \rightarrow L}(T)$. This allows us to express $q_{R \rightarrow L}(T_R)$ purely in terms of the phonon modes of the left lead

$$q_{R \rightarrow L}(T_R) = -q_{L \rightarrow R}(T_R) = -\frac{1}{V_L} \int_{\text{FBZ}_L} d\mathbf{k} \sum_{\nu}^{+z} \hbar\omega_L(\mathbf{k}, \nu) \mathbf{v}_{g,L}(\mathbf{k}, \nu)^\dagger \hat{\mathbf{z}} n_{\text{BE}}(T_R, \mathbf{k}, \nu) \alpha_{L \rightarrow R}(\mathbf{k}, \nu). \quad (2.43)$$

Substitution of Eq. 2.43 into Eq. 2.40 gives

$$q_{\text{Net}} = \frac{1}{V_L} \int_{\text{FBZ}_L} d\mathbf{k} \sum_{\nu}^{+z} \hbar\omega_L(\mathbf{k}, \nu) \mathbf{v}_{g,L}(\mathbf{k}, \nu)^\dagger \hat{\mathbf{z}} [n_{\text{BE}}(T_L, \mathbf{k}, \nu) - n_{\text{BE}}(T_R, \mathbf{k}, \nu)] \alpha_{L \rightarrow R}(\mathbf{k}, \nu). \quad (2.44)$$

Eq. 2.44 represents the net heat crossing the junction from the left lead to the right lead using only the phonon modes of the left lead. Combining Eq. 2.44 with the Fourier law for G (Eq. 2.12) and assuming that the temperature difference between the leads $T_L - T_R$ is infinitesimally small, we arrive upon the Landauer formula for the phonon thermal conductance G of the junction

$$G(T) = \frac{1}{V_L} \int_{\text{FBZ}_L} d\mathbf{k} \sum_{\nu}^{+z} \hbar\omega_L(\mathbf{k}, \nu) \mathbf{v}_{\mathbf{g},L}(\mathbf{k}, \nu) \dagger \hat{\mathbf{z}} \frac{\partial n_{\text{BE}}(T, \mathbf{k}, \nu)}{\partial T} \alpha_{L \rightarrow R}(\mathbf{k}, \nu), \quad (2.45)$$

where T is the temperature of the junction, $T = T_L \approx T_R$. The partial derivative of the Bose-Einstein distribution with respect to temperature on the right-hand side of Eq. 2.45 comes from the first-order term of the limit as $T_L - T_R$ goes to zero. A schematic of the Landauer formalism is shown in Fig. 2.2

While Eq. 2.45 is compact and physically intuitive, there are limitations. First, we assume that the temperature difference between the left and right leads is infinitesimal such that the distribution functions are well approximated by the equilibrium Bose-Einstein distribution at a single temperature. The Landauer formalism as stated in Eq. 2.45 is thus not suitable for finite temperature differences, nor does it account for the non-equilibrium phonon population distributions that must exist in the leads in order for a finite heat to flow. Some work has been done in attempting to use non-equilibrium distributions with the Landauer formalism (see Ref. [4]), but a complete solution must simultaneously solve Eq. 2.45 as well as the ALD problem (discussed in Sec. 2.3.3) for the non-equilibrium distributions in the left and right leads.

Second, G is computed as a summation over the phonon modes in Eq. 2.45 and the transmission coefficients $\alpha_{L \rightarrow R}$ are properties of individual phonon modes. The summation can be interpreted as an assumption that the simultaneous scattering of many phonons from many different phonon modes act independently, and the scattering of a particular

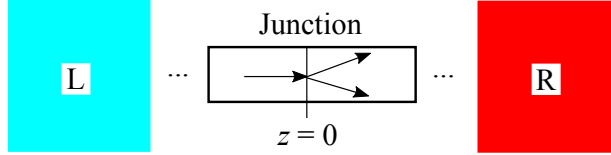


Figure 2.2: A schematic of a junction system in the Landauer formalism. Bulk leads L and R are connected via the junction, but the leads are positioned far from the junction. Phonon scattering events, as represented by the transmission event of a single phonon into two, occur within the junction.

phonon mode does not impact that of others. Eq. 2.45 assumes that, when crossing the junction, phonons interact only with the junction and not with each other, and so the Landauer formalism is referred to as a model for ballistic transport. While phonon-phonon events may be accounted for in the scheme used to compute $\alpha_{L \rightarrow R}$, all phonon-phonon events must still be reduced to a single transmission coefficient for each phonon, much like the relaxation time approximation that can be used in ALD.

2.4.2 Scattering boundary equations

All terms within Eq. 2.45 can be determined by solving the HLD problem (Eq. 2.30) associated with crystal L with the exception of the transmission coefficients $\alpha_{L \rightarrow R}$. Calculation of $\alpha_{L \rightarrow R}$ requires consideration of the structure and dynamics of the junction itself and cannot be ascertained by considering only the lead dynamics. The scattering boundary method (SBM) is a method to compute the transmission coefficient $\alpha(\boldsymbol{\kappa}, \nu)$. It is an HLD-like method that was first formulated by Lumpkin *et al.*[26] as an analytical solution to an interface between two one-dimensional chains. This formalism was extended to two dimensions by Young and Maris[47] and to three dimensions by Zhao and Freund[28]. It has since been applied to silicon/germanium[4, 27] and Lennard-Jones[48] systems. The SBM is theoretically equivalent[49] to the atomistic Green's function method[50].

The SBM computational domain, shown in Fig. 2.3, is an atomistically-defined junction

with left and right boundaries (representing semi-infinite leads) that is treated as a classical spring-mass system. The required inputs to the SBM are the bulk phonon modes of the left and right leads, the atomic structure of the junction, and the second-order (i.e., harmonic) force constants between the atoms within the junction. The formulation presented here is applicable to one-, two-, and three-dimensional systems [28].

The SBM computes $\alpha(\boldsymbol{\kappa}, \nu)$ by solving Newton's second law of motion in the steady state after phonon mode $(\boldsymbol{\kappa}, \nu)$ is incident on the junction from the left boundary. The phonon modes are treated as plane waves and, because all interactions are harmonic, the entire system evolves at $\omega(\boldsymbol{\kappa}, \nu)$, the frequency of the incident phonon.

For every atom within the junction, the equations to be solved are

$$-\omega^2(\boldsymbol{\kappa}, \nu) m^i x_\alpha^i = \sum_{j, \beta} \Phi_{\alpha\beta}^{ij} x_\beta^j, \quad (2.46)$$

where m^i is the mass of atom i , the unknown x_α^i is the α^{th} Cartesian degree of freedom of atom i , and $\Phi_{\alpha\beta}^{ij}$ is the second-order force constant between the α^{th} Cartesian degree of freedom of atom i and the β^{th} Cartesian degree of freedom of atom j . The summation is over all atoms and their degrees of freedom both in the junction and in the boundaries, including self-interaction terms involving the on-diagonal force constant element $\Phi_{\alpha\alpha}^{ii}$.

In the boundaries, the condition that is needed to represent the incoming and outgoing phonon modes is a radiation boundary condition [51]. For all atoms in the left boundary, the unknown atomic degrees of freedom x_α^i for atoms that interact with the junction are prescribed by

$$x_\alpha^i = e(\boldsymbol{\kappa}, \nu)_\alpha^i + \sum_{\boldsymbol{\kappa}', \nu'}^L r(\boldsymbol{\kappa}', \nu') e(\boldsymbol{\kappa}', \nu')_\alpha^i \delta[\omega(\boldsymbol{\kappa}, \nu) - \omega(\boldsymbol{\kappa}', \nu')]. \quad (2.47)$$

Here, $e(\boldsymbol{\kappa}, \nu)_\alpha^i$ is the eigenvector component of phonon mode $(\boldsymbol{\kappa}, \nu)$ corresponding to the

α^{th} Cartesian degree of freedom of atom i . The first term on the right hand side represents the incident phonon mode. Without loss of generality, it is given unit amplitude. The second term on the right hand side represents a superposition of reflected phonon modes, where the summation is performed over the phonon modes of the left lead. The delta function indicates that only reflected modes with the same frequency as the incident mode are considered. The amplitudes of the reflected waves, $r(\boldsymbol{\kappa}', \nu')$, are unknown.

For all atoms in the right boundary, the unknown atomic degrees of freedom x_α^i for atoms that interact with the junction are prescribed by

$$x_\alpha^i = \sum_{\boldsymbol{\kappa}', \nu'}^{\text{R}} t(\boldsymbol{\kappa}', \nu') e(\boldsymbol{\kappa}', \nu')_\alpha^i \delta[\omega(\boldsymbol{\kappa}, \nu) - \omega(\boldsymbol{\kappa}', \nu')]. \quad (2.48)$$

Since the right boundary contains only transmitted modes, the summation is performed over the phonon modes of the right lead and the unknowns $t(\boldsymbol{\kappa}', \nu')$ are the amplitudes of the transmitted waves.

Equations (2.46)-(2.48) form a linear system of equations of the form $\mathbf{Ax} = \mathbf{b}$ that can be solved for the unknowns x_α^i , $r(\boldsymbol{\kappa}', \nu')$, and $t(\boldsymbol{\kappa}', \nu')$. The transmission coefficient $\alpha(\boldsymbol{\kappa}, \nu)$ can then be computed via

$$\alpha(\boldsymbol{\kappa}, \nu) = \sum_{\boldsymbol{\kappa}', \nu'}^{\text{R}} |t(\boldsymbol{\kappa}', \nu')|^2 \frac{v_{g,x}(\boldsymbol{\kappa}', \nu')}{v_{g,x}(\boldsymbol{\kappa}, \nu)} \delta[\omega(\boldsymbol{\kappa}, \nu) - \omega(\boldsymbol{\kappa}', \nu')], \quad (2.49)$$

where $v_{g,x}$ is the phonon mode group velocity in the cross-junction direction. The size of the boundaries should be chosen to contain enough atoms so that the system is at least exactly solvable (i.e., \mathbf{A} is square). That is, the number of degrees of freedom within the left (right) boundary should coincide with the number of modes summed over in Eq. (2.47) [(2.48)].

For reliability, we recommend that a buffer region be made between the boundaries

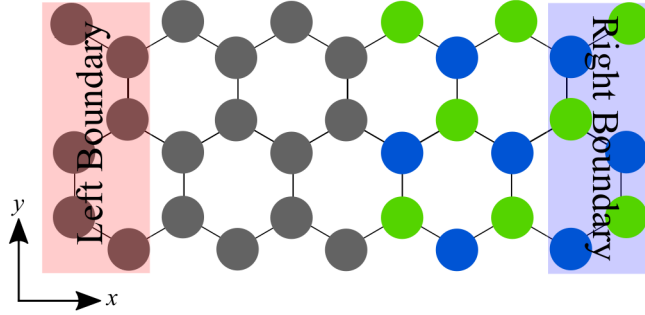


Figure 2.3: Schematic representation of the SBM computational cell for an armchair interface indicating the left boundary (red) and right boundary (blue).

and the junction. All atoms within the left (right) buffer region are then subject to both Eq. (2.46) and Eq. (2.47) [(2.48)]. The addition of the buffer region creates an overdetermined system (i.e., \mathbf{A} has more rows than columns) that can be solved using singular value decomposition.

2.4.3 Symmetry considerations

Within the scattering boundary method (SBM), the equations of motion within the left and right boundaries are given by Eqs. (2.47) and (2.48). The summations over the reflected and transmitted modes are performed over the first Brillouin zones of their respective leads. A numerical solution of these equations would require meshing and summing over a large number of wavevectors and representing the Dirac delta functions as narrow Gaussians. The computational load can be decreased by reducing the number of wavevectors considered to those that (i) satisfy the appropriate geometric condition and (ii) satisfy the frequency constraint imposed by the delta functions. The implementation of these conditions is discussed in the following sections.

2.4.3.1 Crystal momentum conservation

The perfect interface between two leads shown in Fig. 2.3 is aperiodic in the cross-interface x -direction, but remains periodic in the y -direction along the interface (and the z -direction for a three-dimensional system). Whether or not the y - and z - period of the interface match the corresponding bulk periods depends on the interface being studied. Note that the following discussion pertains only to two- and three-dimensional systems, as the wavevector condition is trivial in one-dimension. Note also that no specific rule disallowing in-plane to out-of-plane mode conversion in two-dimensional materials is necessary, as the momentum conservation accounts for this. It would be trivial, however, to explicitly implement such a rule.

In the event that the interface periods matches those of the bulk leads, scattering is specular and

$$\kappa_y(\boldsymbol{\kappa}', \nu') = \kappa_y(\boldsymbol{\kappa}, \nu) \quad (2.50)$$

$$\kappa_z(\boldsymbol{\kappa}', \nu') = \kappa_z(\boldsymbol{\kappa}, \nu). \quad (2.51)$$

That is, all scattered phonon modes have the same wavevector components along the interface as the incident mode.

In the event that the interface periods are larger than those of the bulk (the case for all junctions considered in this work), Eqs. (2.50) and (2.51) are modified to

$$\kappa_y(\boldsymbol{\kappa}', \nu') \equiv \kappa_y(\boldsymbol{\kappa}, \nu) \pmod{2\pi/a_{\text{Int},y}} \quad (2.52)$$

$$\kappa_z(\boldsymbol{\kappa}', \nu') \equiv \kappa_z(\boldsymbol{\kappa}, \nu) \pmod{2\pi/a_{\text{Int},z}}, \quad (2.53)$$

where $a_{\text{Int},y}$ ($a_{\text{Int},z}$) is the interface y -period (z -period). Whereas the conditions given by

Eqs. (2.50) and (2.51) lead to only two planes of constant κ_y and κ_z within the first Brillouin zone upon which scattering might occur, Eqs. (2.52) and (2.53) lead to many, whose number increases as $a_{\text{Int},y}$ and $a_{\text{Int},z}$ increase. As $a_{\text{Int},y}$ and $a_{\text{Int},z}$ go to infinity (as would be required for a rough interface) all wavevectors are possible and scattering is diffuse. Within the context of graphene/hBN, where the Brillouin zone is two-dimensional, only the first condition [Eq. (2.52)] is considered.

2.4.3.2 Energy conservation

After consideration of the wavevector condition, the possible scattered modes are reduced to those that lie along certain planes of constant κ_y and κ_z . The next step is to select from each plane the modes that have frequency $\omega(\boldsymbol{\kappa}, \nu)$ [28].

The first step is to find the κ_x 's at a given κ_y and κ_z that have a mode at frequency $\omega(\boldsymbol{\kappa}, \nu)$. Let \mathbf{D} be the bulk dynamical matrix associated with the lead in question. The dependence of \mathbf{D} on κ_x is isolated by decomposing \mathbf{D} into segments corresponding to the period in the x direction, a_x ,

$$\mathbf{D}(\boldsymbol{\kappa}) = \mathbf{D}_{-,N}e^{-iN\kappa_x a_x} + \dots + \mathbf{D}_{-,1}e^{-i\kappa_x a_x} + \mathbf{D}_0 + \mathbf{D}_{+,1}e^{i\kappa_x a_x} + \dots + \mathbf{D}_{+,N}e^{iN\kappa_x a_x} . \quad (2.54)$$

There are N unit cell replications in the $-x$ and $+x$ directions relative to the central unit cell. With this decomposition, $\mathbf{D}_{-,i}$ and $\mathbf{D}_{+,i}$ depend only on κ_y and κ_z . All dependence on κ_x is in the complex phase factors. Now treat κ_x as an unknown parameter and rewrite

the harmonic lattice dynamics problem as

$$\begin{bmatrix} \mathbf{D}_{-,N} & \mathbf{D}_{-,N-1} & \cdots & \mathbf{D}_{-,1} & \mathbf{0}_1 & \cdots & \mathbf{0}_N \\ & \mathbf{I} & & & & & \\ & & \mathbf{I} & & & & \\ & & & \cdot & & & \\ & & & & \cdot & & \\ & & & & & \cdot & \\ & & & & & & \mathbf{I} \\ & & & & & & \mathbf{0} \end{bmatrix} \mathbf{v} = \xi \begin{bmatrix} \mathbf{0} & \omega^2 \mathbf{I} - \mathbf{D}_0 & \mathbf{D}_{+,1} & \mathbf{D}_{+,2} & \cdots & \mathbf{D}_{+,N} \\ \mathbf{I} & & & & & \\ & \cdot & & & & \\ & & \cdot & & & \\ & & & \cdot & & \\ & & & & \cdot & \\ & & & & & \mathbf{I} \\ & & & & & \mathbf{0} \end{bmatrix} \mathbf{v}, \quad (2.55)$$

where $\xi = \exp(i\kappa_x a_x)$ and

$$\mathbf{v}^\dagger = \left[\xi^{-N} \mathbf{e} \quad \xi^{-(N-1)} \mathbf{e} \quad \cdots \quad \xi^{-1} \mathbf{e} \quad \mathbf{e} \quad \xi \mathbf{e} \quad \cdots \quad \xi^{(N-1)} \mathbf{e} \quad \xi^N \mathbf{e} \right]. \quad (2.56)$$

Here, $\mathbf{0}$ and \mathbf{I} represent zero and identity matrices of the same dimension as \mathbf{D} , blanks are zeros, and \mathbf{e} is the harmonic lattice dynamics polarization eigenvector of the as yet unknown matching mode. Eq. (2.55) is a generalized eigenvalue problem with eigenvectors \mathbf{v} and eigenvalues ξ . Once the eigenvalues ξ are found, κ_x can be determined via $\kappa_x = -i \log(\xi)/a_x$.

This process is repeated for all planes of constant κ_y and κ_z until a complete list of reflected and transmitted modes is formed. Once this list is formed, Eqs. (2.47) and (2.48) are simplified to

$$x_\alpha^i = e(\boldsymbol{\kappa}, \nu)_\alpha^i + \sum_\rho^L r_\rho e(\boldsymbol{\kappa}', \nu')_{\alpha, \rho}^i \quad (2.57)$$

and

$$x_\alpha^i = \sum_\tau^R t_\tau e(\boldsymbol{\kappa}', \nu')_{\alpha, \tau}^i, \quad (2.58)$$

where the ρ and τ index over the reflected and transmitted mode lists. The workflow for

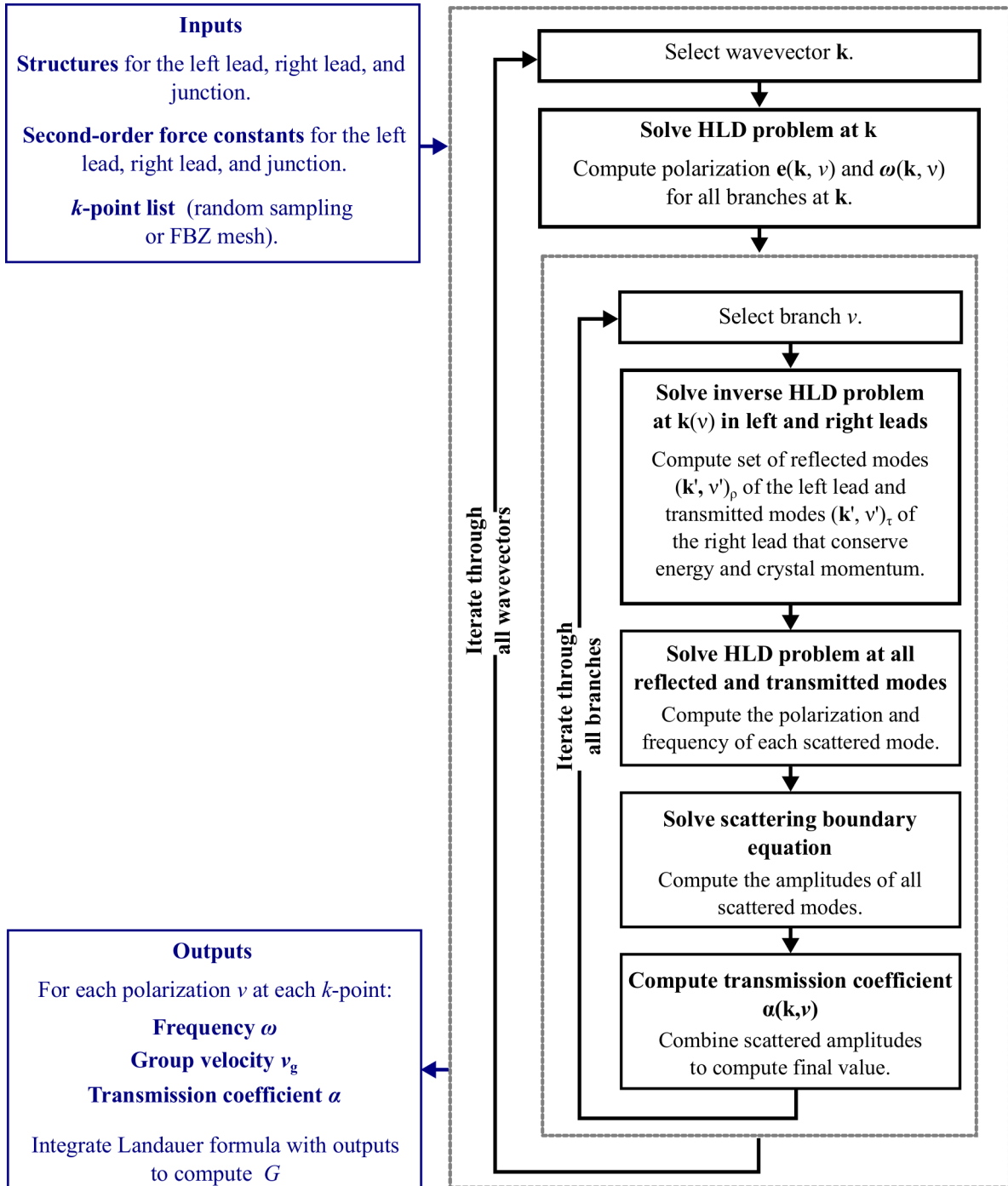


Figure 2.4: Workflow for SBM calculations. Blue boxes represent pre- and post-processing steps, while black boxes indicate calculations done within the SBM program. Dotted gray boxes indicate computations that must be repeated for every wavevector, and every phonon polarization at a wavevector.

SBM calculation is summarized in Fig. 2.4.

Lennard-Jones superlattice junctions

3.1 Introduction

Semiconductor superlattice nanostructures have received considerable research attention since their first appearance in the 1970s [5, 6]. They have applications in solid state lighting and thermoelectric energy conversion due to the size-tunability of their electronic properties. Within a light-emitting diode, lattice-assisted electron-hole recombination generates heat, which must be adequately dissipated in order to maintain performance and prolong device life. The possibility of tuning superlattice design for low thermal conductivity provides a potential path to optimizing the thermoelectric figure of merit.

Early experimental measurements of superlattices revealed that their thermal conductivities were reduced from the bulk thermal conductivities of their constituent materials [52, 53, 54]. This finding was attributed to (i) reduction of phonon mean free paths within the layers and (ii) thermal resistance at the internal interfaces. Computational work on thermal transport within superlattices has been performed using equilibrium [55, 56] and non-equilibrium [31, 55, 57, 58, 59, 60, 61] molecular dynamics (MD) simulations. MD studies are limited by classical statistics and are performed on systems for which empirical potentials are available [e.g., LJ argon, Stillinger-Weber Si-Ge, and Tersoff graphene-BN]. Work has also been done using perturbative anharmonic lattice dynamics calculations, using force constants from both analytical potentials and from density functional theory calculations [62, 63, 64].

A minimum in superlattice thermal conductivity with superlattice period length was predicted using a simple theoretical model by Simkin and Mahan [65], observed computa-

tionally using both MD and lattice-based computational techniques [55, 60, 61, 66], and recently observed experimentally by Ravichandran *et al.* [67]. This minimum is described as a consequence of the transition between a regime where vibrational wave interference significantly affects thermal transport (i.e., the coherent regime) and a regime where waves do not interfere and a particle-like treatment is appropriate [65].

Since superlattices in technological applications are typically grown on substrates and are finite in length, they differ significantly from the ideal infinite superlattice. Instead, it is appropriate to treat them as junctions sandwiched between two bulk leads and to associate the thermal transport through the junction with a thermal conductance. Modeling of thermal transport through the junction with a thermal conductance. Modeling of thermal transport across solid-solid interfaces and junctions began in the 1950s [68] but was limited to simple analytical models (e.g., the acoustic mismatch and diffuse mismatch models) that could not account for detailed interface geometry [3]. Beginning with Lumpkin *et al.* [26], a harmonic lattice-based analytical technique was developed that accounted for exact interface atomic positions and interactions. This technique was based on the scattering of incident phonons by the interface [47, 69], was generalized by Zhao and Freund to arbitrary three-dimensional interfaces [28], and is now known as the scattering boundary method (SBM). Zhao and Freund studied ideal Si-Ge interfaces and verified the validity of the SBM against MD studies of interfaces that used wave packets [70]. Other studies using the SBM focused on the effect of incidence angle on transmission [27] and on the use of non-equilibrium distribution functions in the leads [4].

The use of non-equilibrium MD (NEMD) simulation to probe interface thermal transport developed in parallel to the SBM. Maiti *et al.* were the first to use NEMD simulation to predict interface thermal conductance, studying grain boundaries in Si [71]. NEMD has since been used to study defective interfaces with LJ and Morse interactions [72], temperature and disorder effects at LJ interfaces [73] and Si-Ge interfaces using the Stillinger-Weber

potential [4]. Duda *et al.*, using NEMD, noted that the thermal conductance of an isolated LJ interface increased linearly with increasing temperature [74].

The study of finite-size junctions extended naturally from the techniques developed for isolated interfaces. Landry and McGaughey investigated Si (Ge) thin films sandwiched between bulk Ge (Si) leads. In particular, they studied the dependence of junction thermal conductance on junction length using both SBM calculations and NEMD simulations [75]. Tian *et al.* [76] studied Si-Ge superlattice junctions using a harmonic lattice-based technique [49, 77], where they found that the introduction of disorder at interfaces destroyed coherent transport of phonons, particularly those with high frequencies.

Previous works on superlattices [65, 67] and superlattice junctions [64, 76] suggest that thermal transport in superlattice junctions depends on both period length and junction length, and is modified by disorder. In this chapter, we vary both period length and junction length, and consider the effects of lead composition, finite temperature, and disorder. In Sec. 3.2, we define the structure of the superlattice junction. We describe the three techniques used in Sec. 3.3: the thermal circuit model, NEMD simulations, and the Landauer transport formula with the SBM. Our findings, notably a lead effect, are reported in Sec. 3.4 and summarized in Sec. 3.5.

3.2 Superlattice junction structure: the multiple thin film system

We are interested in calculating the thermal conductance of superlattice junctions with bulk leads. The atoms in our representative crystalline material interact via the pairwise

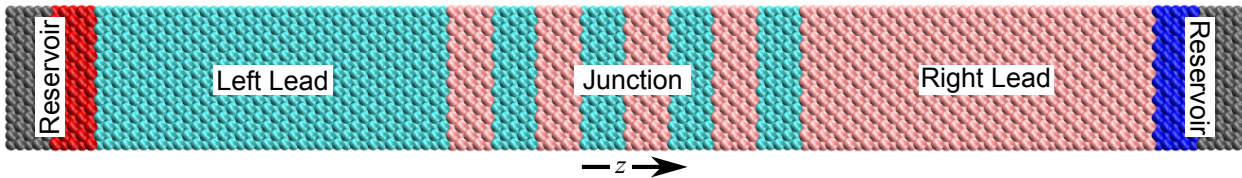


Figure 3.1: Example structure for the case of eight thin films ($m = 8$, a mismatched case) with five monolayers per thin film ($n = 5$). Cyan atoms are Type 1 and pink atoms are Type 2. The red and blue atoms are in the reservoirs and the gray atoms are fixed for use in the MD simulations.

LJ potential with argon parameters. The LJ pairwise interaction is

$$\phi_{ij}(r) = 4\epsilon \left[\left(\frac{\sigma}{r} \right)^{12} - \left(\frac{\sigma}{r} \right)^6 \right], \quad (3.1)$$

where r is the distance between any atoms i and j . The argon LJ parameters are $\epsilon = 1.67 \times 10^{-21}$ J and $\sigma = 3.40 \times 10^{-10}$ m. The interaction is cut off at 2.5σ . Two atomic species are used in order to generate the superlattice junction structures: regular argon (Type 1) and “heavy” argon (Type 2). Type 1 and Type 2 atoms interact identically. They differ only in their masses, μ_1 and μ_2 . Type 1 argon has the true argon atomic mass, $\mu_1 = 6.634 \times 10^{-26}$ kg. In keeping with previous work on similar systems [56, 74] and to capture an atomic mass ratio typical of real nanostructures, $\mu_2 = 3\mu_1$. Thin films of Type 1 and Type 2 atoms are built along the [001] crystallographic direction (i.e., the z axis) in a fashion that alternates between Type 1 and Type 2, as shown in Fig. 3.1.

The alternating Type 1 and Type 2 thin films form the superlattice junction. A junction is defined by the number of atomic monolayers per thin film n , the number of thin films in the junction m , and the argon face-centered cubic (FCC) conventional unit cell lattice constant a (5.315 Å and 5.370 Å at temperatures of 20 K and 40 K) [78]. The length of a single thin film is $na/2$. The length of the entire junction is $mna/2$. We discuss cases where $n = \{2, 4, 8\}$ and m ranges from 1 to 40, leading to junction lengths ranging from 1 nm to 40 nm. We do not explore junction lengths greater than 40 nm, as such structures

may result in a numerical divergence of the thermal conductance prediction as described by Hu *et al* [79]. Finally, the junction is sandwiched between two bulk-like leads. The left lead is always of Type 1. For m odd, the right lead will be of Type 1 (i.e., matched leads). For m even, the right lead will be of Type 2 (i.e., mismatched leads). m_1 (m_2) are the number of thin films of Type 1 (Type 2) in the junction, such that $m_1 + m_2 = m$. Method-specific details are provided in Secs. 3.3.2 and 3.3.3.

3.3 Methods

3.3.1 Thermal circuit

If we assume that each Type 1 - Type 2 interface inside a junction acts as a memoryless phonon scatterer and that each constituent thin film has the thermal conductivity equivalent to a bulk of its type, then the junction can be represented by a series of interface and thin film thermal resistors. This assumption leads to a simple but naïve prediction of the junction thermal conductance

$$G_{\text{J,TC}}(T) = \left[\sum_{i=1}^{m_1} \frac{na}{k_1(\overline{T}_i)} + \sum_{j=1}^{m_2} \frac{na}{k_2(\overline{T}_j)} + \sum_{k=1}^{m_1+m_2+1} \frac{1}{G_{\text{Int},1-2}(T_{\text{Int},k})} \right]^{-1}, \quad (3.2)$$

where k_1 (k_2) is the temperature-dependent bulk crystal thermal conductivity of Type 1 (Type 2) atoms and $G_{\text{Int},1-2}$ is the temperature-dependent per unit area thermal conductance of an isolated Type 1 - Type 2 interface. T is the average temperature of the junction, \overline{T}_i is the average temperature of the i^{th} film within the junction, and $T_{\text{Int},k}$ is the temperature of the k^{th} interface within the junction.

3.3.2 Non-equilibrium molecular dynamics

The direct heat method [25] in NEMD simulation (see Sec. 2.2.3) is performed on the systems of interest using LAMMPS [30] and a time step of 4.34 fs. In an MD simulation, the classical equations of motion are numerically integrated to predict the trajectories of atoms. MD simulations can account for the full effect of the anharmonic interactions between atoms, which is important at finite temperature for LJ interface systems [74]. The aim of the direct heat method is to predict the temperature distribution in the cross-interface (z) direction given a fixed heat flow.

The cross-sectional area of the simulation cell is 6×6 FCC conventional unit cells, giving an area $A = 36a^2$, which is 10.17 nm^2 and 10.38 nm^2 at temperatures of 20 K and 40 K. Each atomic monolayer in the z -direction (i.e., half a conventional unit cell) is composed of $6 \times 6 \times 2 = 72$ atoms. The first four and last four monolayers (288 atoms) of the NEMD system are fixed to prevent atomic sublimation and to give the other atoms a bulk-like environment. Immediately adjacent to both sets of fixed atoms are 16 atomic monolayers (1152 atoms) of thermal reservoir, from which energy will be added or removed during the non-equilibrium portion of the simulation. Interior to the thermal reservoirs on both ends are 120 atomic monolayers (8640 atoms) serving as bulk-like leads.

Velocity rescaling is first performed for 10^6 time steps to ensure that the mean kinetic energy per atom is $1.5k_B T$, where k_B is the Boltzmann constant. The system is then evolved in the microcanonical ensemble for 10^6 time steps to recover realistic Hamiltonian dynamics. For the next 8×10^6 time steps, a fixed amount of energy is removed from the right reservoir and placed in the left reservoir every time step such that total system energy is conserved. This energy transfer is accomplished by rescaling the velocities of the reservoir atoms. Based on the thermal circuit model described in Sec. 3.3.1, the energy transfer (i.e., heat flow) is specifically chosen for the film number, number of monolayers per

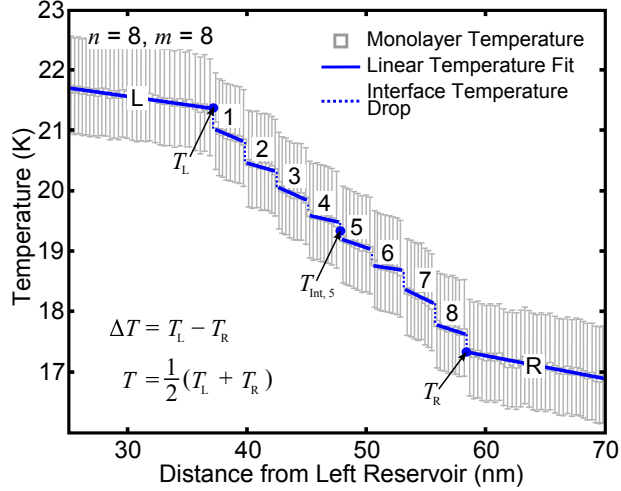


Figure 3.2: Temperature profile from NEMD for eight films ($m = 8$) of eight atomic monolayers each ($n = 8$) at an average temperature of 20 K. The error bars on the monolayer temperatures represent their standard deviation over the data collection time steps. The intrajunction films are numbered 1 through 8, while the left and right leads are labeled L and R.

film, and average temperature of the system so as to produce a cross-junction temperature difference of 5 K. After the 8×10^6 time step run to steady-state, monolayer temperatures and positions are averaged and collected for 5×10^6 time steps. A monolayer's temperature is defined as the temperature corresponding to its mean kinetic energy.

The result of the averaging is a temperature versus position distribution like that shown in Fig. 3.2 for the case of eight films of eight atomic monolayers each ($m = 8$, $n = 8$) at an average temperature of 20 K. Least-squares linear fits to the temperature profile are performed in the leads. Data in the 40 atomic monolayers closest to either reservoir are not included in the lead fits as their dynamics are influenced by the velocity rescaling. Interface temperatures are defined by extrapolation of the fits to the interface locations and then averaging the values on each side. The thermal conductance of the junction region is obtained from

$$G_{J,\text{NEMD}}(T) = \frac{q}{A\Delta T}, \quad (3.3)$$

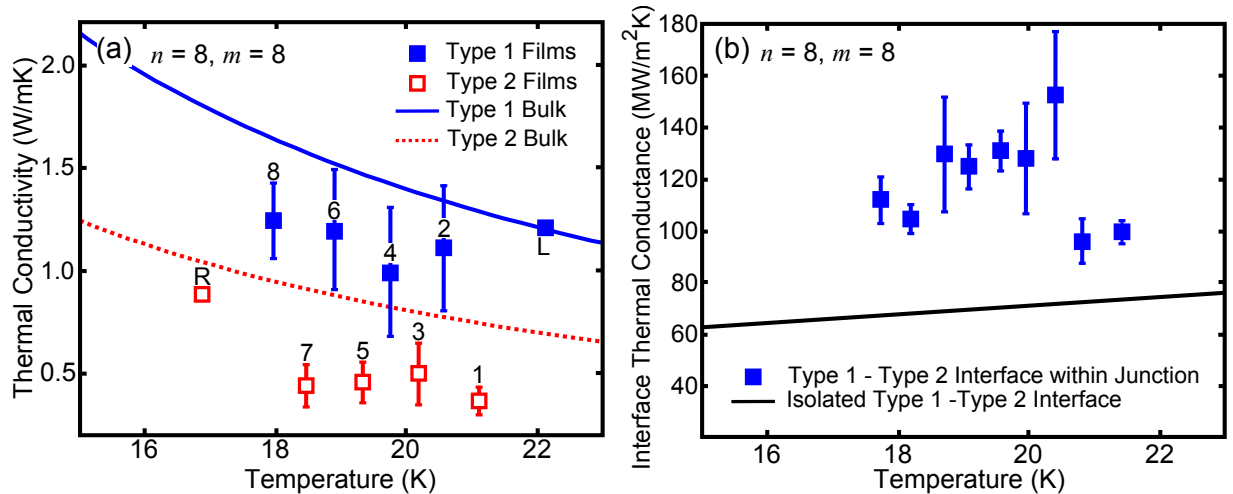


Figure 3.3: Intrajunction (a) film thermal conductivities and (b) film-film interface thermal conductances for the same case as Fig. 3.2 ($n = 8$, $m = 8$). These data are averaged from temperature profiles from five independent NEMD runs, including the profile shown in Fig. 3.2. They are compared against temperature-dependent NEMD values of bulk thermal conductivity and isolated interface thermal conductance. The error bars indicate the standard deviation over the five independent runs.

where ΔT is the difference between the temperatures of the left lead fit extrapolated to the first interface and the right lead fit extrapolated to the last interface. T is the mean of those two temperatures. As shown in Fig. 3.2 and in previous work [57], this method is also able to resolve individual thin film thermal conductivities and intrajunction interface thermal conductances when the thin films are sufficiently large. For systems with eight atomic monolayers per film (e.g., Fig. 3.2), the resolution is good. For systems with two or four atomic monolayers per film, the resolution is poor.

For a system with eight thin films of eight atomic monolayers each at an average temperature of 20 K, the intrajunction film thermal conductivities are plotted in Fig. 3.3(a) as a function of the average individual film temperature. These results are compared against temperature-dependent thermal conductivities for bulk Type 1 and Type 2 argon. The film-film thermal interface conductances for the same case are plotted in Fig. 3.3(b) as a function of interface temperature. The results are compared against the temperature-

dependent thermal conductance of an isolated Type 1 - Type 2 interface. The bulk thermal conductivities and isolated interface thermal conductances are obtained from independent NEMD simulations.

The decrease of thermal conductivity inside the thin films [points 1 through 8 in Fig. 3.3(a)] compared to bulk is consistent with the memoryless interface scattering assumption of the thermal circuit model, where complete carrier scattering at the interfaces causes a reduction of their mean free paths. Note that for the long leads [points L and R in Fig. 3.3(a)], no such reduction is present and the thermal conductivity predictions are close to the bulk values. The 50 to 100% increase of the film-film interface thermal conductances [Fig. 3.3(b)], however, is not consistent with the assumption of memoryless interface scattering. A possible cause of the elevation in thermal conductance is the emergent periodicity of the superlattice junction. The periodicity causes interference between vibrational waves that are scattered by the regularly-spaced interfaces. This effect may be masked within MD simulations due to anharmonic scattering, so we will use a harmonic, lattice-based technique for further analysis.

3.3.3 Scattering boundary method

3.3.3.1 Landauer formula

To isolate the effects of the emergent periodicity, we now limit our analysis to harmonic interactions and consider the transport of vibrational mode energy across the junction. The Landauer formalism as described in Sec. 2.4 is used and is briefly summarized here. Despite the advantages described in Sec. 3.3.2, MD simulations do not provide information about the vibrational modes of the system without additional, computationally-expensive processing steps [56, 80, 81]. In order to extract mode-level detail, we move to a method built explicitly upon the basis of vibrational modes. Consider a model where the vibra-

tional modes of the left lead are coupled to vibrational modes of the right lead via the junction. Since the leads are bulk crystals, their vibrational modes are phonon modes. Further, because there is no anharmonic scattering, the transport through the junction is ballistic and the transmission is elastic (i.e., there is no coupling between vibrational modes of different frequency). Finally, we assume that the temperature difference between the left and right leads is infinitesimal. These conditions and assumptions allow us to apply the Landauer ballistic transport formula to compute the thermal conductance of our superlattice junctions [45].

In the classical limit, application of this formula results in the following expression for the junction thermal conductance

$$G_{\text{J,SBM}} = \frac{1}{V} \sum_{\boldsymbol{\kappa}, \nu}^{\text{Left, } +z} k_{\text{B}} v_{g,z}^{\text{I}}(\boldsymbol{\kappa}, \nu) \alpha_{\text{L} \rightarrow \text{R}}(\boldsymbol{\kappa}, \nu). \quad (3.4)$$

The summation is performed over all rightward traveling bulk phonon modes of the left lead (i.e., incident phonon modes), with each phonon mode being described by a wavevector $\boldsymbol{\kappa}$ and a polarization ν . V is the volume per mode in the reciprocal space of the left lead crystal. $v_{g,z}^{\text{I}}$ is the z -component of the group velocity of the incident phonon mode (I indicates incident). Determination of the bulk phonon properties is done via harmonic lattice dynamics calculations (see Sec. 2.3) [18]. The junction coupling comes in via the transmission coefficient $\alpha_{\text{L} \rightarrow \text{R}}$, a mode-dependent dimensionless quantity that takes on values between zero and unity. In the particle picture, α is the fraction of phonon energy quanta that cross the junction given an incident flux. In the wave picture, α is the fraction of energy flux from the incident wave that crosses the junction.

We use the SBM to compute the transmission coefficients of the incident phonon modes [4, 27, 28, 47]. The SBM is comprised of two steps, which are briefly described in Secs. 3.3.3.2 and 3.3.3.3. For a detailed derivation, see Sec 2.4, or Wang and Wang

[27] or Zhao and Freund [28]. For each junction, bulk phonon properties and phonon transmission coefficients are calculated for rightward traveling modes at 10,000 wavevectors uniformly sampled from the first Brillouin zone of the left lead. Thermal conductance is computed by performing a summation over the sampled modes as shown in Eq. 3.4. We validate our implementation of the SBM against a zero temperature extrapolation of the isolated Type 1 - Type 2 interface thermal conductances from our NEMD simulations [the black line in Fig. 3.3(b)]. The difference between the SBM calculation and the NEMD extrapolation is 8%. Our NEMD interface thermal conductances and extrapolation agree well with results from Duda *et al* [74].

3.3.3.2 Determination of scattered modes

When phonons of wavevector and polarization $[\boldsymbol{\kappa}, \nu]^I$ encounter the junction, some of the energy is reflected back into the left lead, while the remainder is transmitted into the right lead. The first part of the procedure to compute $\alpha_{L \rightarrow R}([\boldsymbol{\kappa}, \nu]^I)$ is to determine what modes are excited in reflection and what modes are excited in transmission. Let the set of possible reflected modes be denoted by $[\boldsymbol{\kappa}, \nu]_j^R$ and the set of possible transmitted modes be denoted by $[\boldsymbol{\kappa}, \nu]_i^T$, where indices i and j indicate that there may be many such modes. Due to the identical crystal structures and lattice constants of Type 1 and Type 2 argon, periodicity in the x - y plane is preserved, hence the x and y components of $\boldsymbol{\kappa}_j^R$ and $\boldsymbol{\kappa}_i^T$ must equal those of the incident mode. The conservation of the wavevector in the x - y plane is equivalent to assuming totally specular scattering. Due to the assumption of elastic transmission, the frequency of the reflected and transmitted modes are identical to that of the incident mode. The problem of finding all phonon modes in both the left and right leads that have the same κ_x , κ_y , and ω as the incident mode can be formulated and solved as a generalized eigenvalue problem.

3.3.3.3 Scattering boundary equations

Once the reflected and transmitted mode sets $[\boldsymbol{\kappa}, \nu]_j^{\text{R}}$ and $[\boldsymbol{\kappa}, \nu]_i^{\text{T}}$ have been determined, $\alpha_{\text{L} \rightarrow \text{R}}([\boldsymbol{\kappa}, \nu]^{\text{I}})$ can be computed by solving the equations of motion of the junction atoms and the lead atoms in the vicinity of the junction. The Newtonian equations of motion are written down explicitly for each junction atom, including interactions with junction atoms and lead atoms. Two equations are written down for each lead atom. The first equation is its Newtonian equation of motion. The second equation is one that enforces the motion of the lead atom as a superposition of incident and reflected modes (for the left side) or transmitted modes (for the right side). These modes have unknown amplitudes R_j and T_i . The assumption of elastic scattering allows us to ascribe an identical periodic time-evolution of $\exp(i\omega t)$ to each atom. The specification of this evolution converts the system of linear differential equations into a system of linear algebraic equations. The identical periodic time evolution means the SBM solutions are time coherent.

This overdetermined system of equations is solved by minimizing the squared error using singular value decomposition. Finally, the modal transmission coefficient is determined as

$$\alpha_{\text{L} \rightarrow \text{R}}(\boldsymbol{\kappa}, \nu) = \sum_i \frac{v_{g,z}^{\text{I}}}{v_{g,i,z}^{\text{T}}} |T_i|^2, \quad (3.5)$$

where the summation is performed over all transmitted modes. $v_{g,i,z}^{\text{T}}$ is the z -component of the group velocity of the i^{th} transmitted mode.

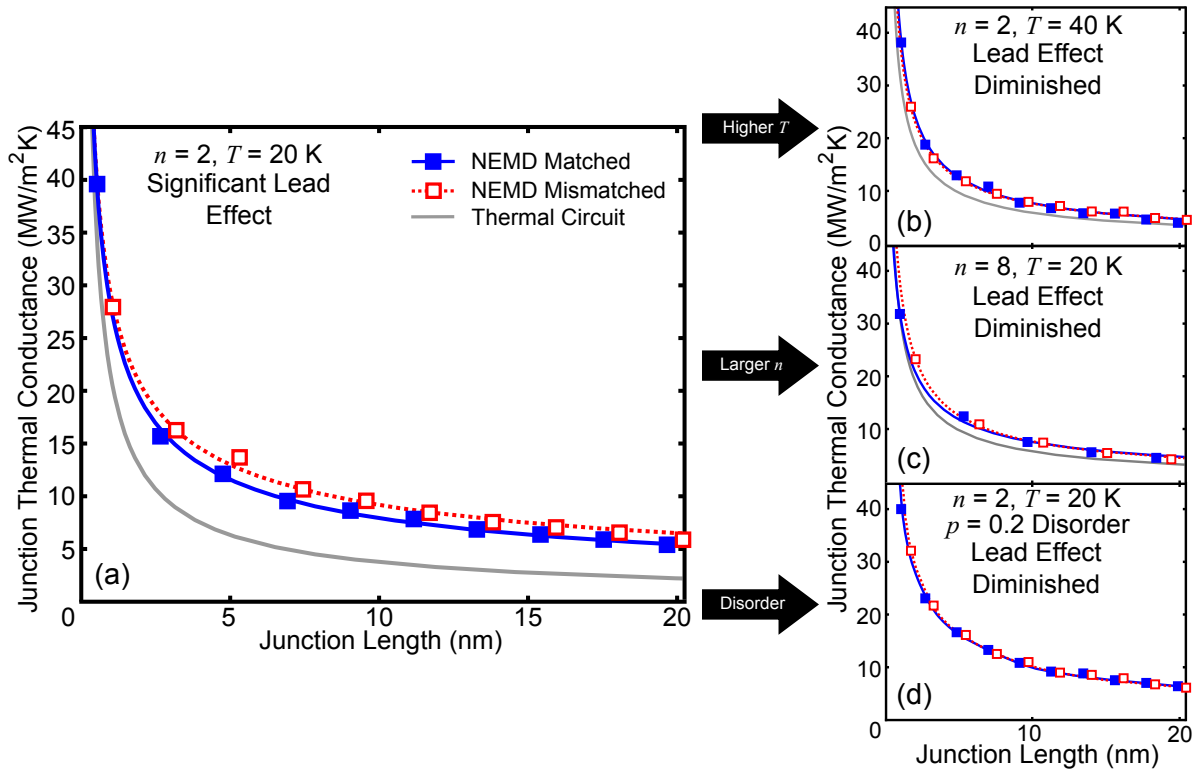


Figure 3.4: Length-dependent junction thermal conductances for the cases (a) $n = 2$, $T = 20$ K, (b) $n = 2$, $T = 40$ K, (c) $n = 8$, $T = 20$ K, and (d) $n = 2$, $T = 20$ K with $p = 0.2$ interfacial species disorder from NEMD and the thermal circuit model. The $n = 2$, $T = 20$ K case shows a strong lead effect, which persists as the number of junction thin films increases. The lead effect is diminished at higher temperatures, greater number of monolayers per thin film, and with the introduction of species disorder at the interfaces.

3.4 Results

3.4.1 NEMD indicates a lead effect

The length dependence of the thermal conductance for superlattice junctions with two, four, and eight atomic monolayers per thin film at average temperatures of 20 K and 40 K were extracted from NEMD simulations. Values for each case were determined as an average over five independent simulations. A select subset of the results are plotted in Figs. 3.4(a)-3.4(d). Power law fits for even thin film number and odd thin film number junctions are also plotted, as is the thermal conductance predicted from the thermal circuit model for the same configurations [Eq. (3.2)]. In all cases, the thermal circuit model underpredicts the NEMD result. The average underprediction throughout the length domain as a percentage of the thermal circuit conductance for two atomic monolayers per film is 60% at 20 K and 26% at 40 K. For four atomic monolayers per film, the underprediction is 34% at 20 K and 9% at 40 K. For eight atomic monolayers per film, the underprediction is 16% at 20 K and 11% at 40 K. This consistent underprediction indicates that the assumption of diffusive transport within films and memoryless scattering at the intrajunction interfaces in the thermal circuit model is an incomplete description of the energy transport process. The discrepancy is largest at low temperature and small film thickness [Fig. 3.4(a)], while the high temperature [Fig. 3.4(b)] and large film thickness [Fig. 3.4(c)] NEMD results are closer to the thermal circuit predictions. The latter results are not surprising since diffusive transport becomes dominant in the high temperature and large film thickness limits. The data in Fig. 3.4(d) are for cases where species disorder is introduced at the lead-junction and intrajunction interfaces. Disorder at the interface is introduced in this fashion: atoms within a thin film of Type 1 (Type 2) immediately adjacent to an interface have a probability p of being Type 2 (Type 1). No comparisons to the thermal circuit

model are made for the disordered cases.

The power law fits are used to differentiate between cases where the thin film number is odd and the leads are of the same type (matched) and cases where the thin film number is even and the leads are of differing type (mismatched). We observe for both temperatures and at all thin film thicknesses that the junction thermal conductances of the mismatched cases are elevated compared to the matched cases at similar lengths. Since the mismatched and matched cases are always at different lengths, it is more appropriate to compare the power law fits. In most of the configurations presented, the difference between the matched and mismatched cases is within the uncertainty of the fits. A clear difference in trend, however, can be observed for the case of two atomic monolayers per film at a temperature of 20 K [Fig. 3.4(a)]. In this case, the 95% confidence intervals of the power law fits (which, for the sake of clarity, are not shown) share very small overlap and the difference between the trends is statistically significant. The mismatched cases consistently exhibit a thermal conductance that is 10% higher than the matched cases at comparable length. In the thermal circuit model, matched and mismatched cases differ only in an additional interface resistance. This difference goes to zero in the limit of large junction size, as the resistance of a single interface becomes negligible compared to the overall resistance of the junction. The 10% difference in conductance seen in the NEMD results, however, persists at all examined lengths with no noticeable attenuation up to the longest lengths investigated. Further NEMD simulations for the $n = 2$ case were performed at average junction temperatures of 15, 10, and 5 K (The conventional unit cell lattice constants of LJ argon at 5, 10, and 15 K are 5.280 Å, 5.289 Å, and 5.303 Å. These values are interpolated from data presented in Ref. [78]). The same lead effect persists at all temperatures investigated. In conjunction with the elevation of intrajunction interface thermal conductances discussed in Sec. 3.3.2 [Fig. 3.3(b)], the lead effect provides further

evidence that the thermal circuit model is insufficient.

The lead effect diminishes when (i) temperature is increased [Fig. 3.4(b)], (ii) the intrajunction thin films are made thicker [Fig. 3.4(c)], and (iii) species disorder is introduced to the lead-junction and intrajunction interfaces [Fig. 3.4(d)]. The increase of temperature increases anharmonic scattering, leading to diffusive transport. Hence, one hypothesis is that the lead effect is caused by partial ballistic transport of energy carriers across the junction. These carriers are not bulk phonons of the constituent films, but rather emergent modes of the superlattice junction. Much like phonons of bulk superlattices [56], these modes do not consider the intrajunction interfaces as defects and do not scatter from them. Disorder at the intrajunction interfaces, however, does act as a scattering source for these emergent modes. Hence, in agreement with earlier work [76], the introduction of species disorder at interfaces also leads to diffusive transport.

If the lead effect is completely attributable to ballistic transport, we would expect saturation of both matched and mismatched junction thermal conductances to a single, fully diffusive limit at long junction lengths (as is the case with thin films of bulk crystals) [75]. For the junction lengths evaluated, however, this saturation is not observed. Instead, the lead effect diminishes as the length of the junction's constituent thin films is increased [Fig. 3.4(c)], not as the total junction length is increased. Within a single thin film, this result can be explained as a size effect related to the thin film length and the mean free paths of the phonons of the film's constituent material [75]. In the picture of the emergent superlattice modes, however, increasing the superlattice period alters the modes themselves [56]. It is known that the thermal conductivity of a bulk superlattice is sensitive to its period (i.e., the minimum in superlattice thermal conductivity) and can be partitioned into a regime where vibrational wave interference is significant and one where interference is not [65, 67]. Hence, another hypothesis is that the lead effect is partially attributable

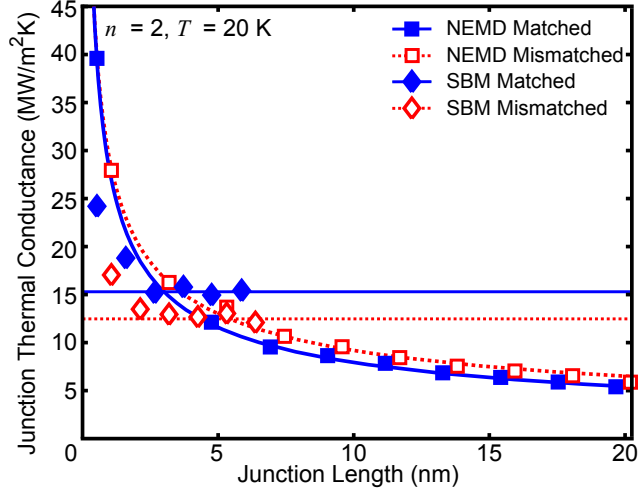


Figure 3.5: Length-dependent junction thermal conductances for the case $n = 2$, $T = 20$ K from NEMD simulations and the SBM calculations. Red and blue curves under the square symbols are power law fits to the NEMD data. Red and blue lines under the diamond symbols are the length-converged SBM results.

to vibrational wave interference in the superlattice junction. Increasing the period of the superlattice junction attenuates the lead effect by moving the system out of the regime where interference is significant.

3.4.2 Lead effect is reversed in harmonic calculation

The interesting case of two atomic monolayers per film at a temperature of 20 K is now analyzed using the SBM. As discussed in Sec. 3.3.3.3, the fully harmonic nature of the SBM calculation has two consequences. First, it considers transport that is completely ballistic. Second, any spatial interference effects caused by the emergent superperiodicity of the junction are preserved. Hence, the SBM can be used to evaluate the two hypotheses posed at the end of Sec. 3.4.1.

Since classical statistics are used to achieve parity with the MD simulations, the only finite temperature effect in the SBM is the setting of the lattice constant equal to the equilibrium value at a temperature of 20 K. As plotted in Fig. 3.5, the SBM junction

thermal conductances converge to length-independent values at a junction length of approximately 4 nm. These results stand in contrast to the NEMD results, where scattering within the junction causes the junction thermal conductances to continue to decrease with increasing junction length. While the SBM results are length-independent beyond junction lengths of 4 nm, they exhibit a strong dependence on the lead properties (i.e., matched or mismatched) at all lengths. The cases with matched leads converge to a junction thermal conductance of 16 MW/m²K, while the cases with mismatched leads converge to 13 MW/m²K, a difference of 19%. The SBM captures the lead effect, but the relative magnitudes of the matched versus mismatched junction thermal conductances are flipped when compared to the NEMD results.

The origin of the lead effect in the SBM calculations can be revealed by examining the transmission coefficients plotted in Figs. 3.6(a) and 3.6(b). Fig. 3.6(a) corresponds to a matched case with seven junction thin films (3.7 nm), while Fig. 3.6(b) corresponds to a mismatched case with eight junction thin films (4.2 nm). Since the thermal conductances for both cases have converged with junction length (Fig. 3.5), the differences in their transmission coefficients must be due to the differing mass of the right lead. The lead effect is not due to the lower cutoff frequency of the Type 2 material, but instead due to details in the shared frequency range of the two materials. While the mismatched case has exactly zero transmission for incident phonons of frequency greater than the Type 2 cutoff, the matched case shows only small transmission beyond the Type 2 cutoff. This finding is highlighted in Fig. 3.7, where the accumulation of the junction thermal conductance against incident phonon frequency is plotted for both matched and mismatched cases. For the matched case, incident phonons above the Type 2 cutoff frequency result in only 0.7% of the overall thermal conductance. Instead, the difference in thermal conductance can be attributed to dips in the transmission coefficients that appear at 1 and 3 Trad/s in

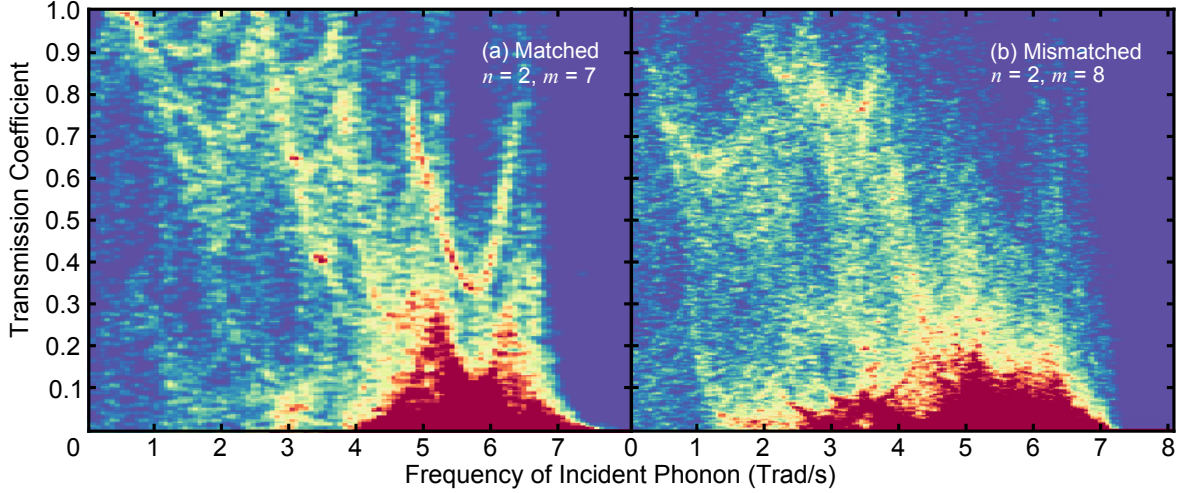


Figure 3.6: Transmission coefficient versus frequency color histograms from the SBM for length-converged matched and mismatched cases. Since these results represent length-converged systems, differences in transmission coefficients between the two cases are due to differences in the right lead mass. The cutoff frequency of Type 2 argon is 7.23 Trad/s. Different colors represent the number of modes in bins of frequency and transmission coefficient.

Fig. 3.6(b), but are far less significant in Fig. 3.6(a). The difference can also be attributed to slower accumulation of the thermal conductance between 2-3 and 5-6 Trad/s. We attribute the maxima and minima in the transmission coefficients seen in Figs. 3.6(a) and 3.6(b) to constructive and destructive interference between reflections and transmissions across successive intrajunction interfaces.

3.5 Summary

Our investigation of superlattice junctions in this chapter reveals that their thermal conductance at finite temperature depends on the material properties of the leads. Specifically, systems with mass-mismatched leads have higher thermal conductance than those with mass-matched leads. This dependence persists when overall junction length is increased [Fig. 3.4(a)], but diminishes when temperature is increased [Fig. 3.4(b)], when the thicknesses of the constituent films are increased [Fig. 3.4(c)], and when species disorder is

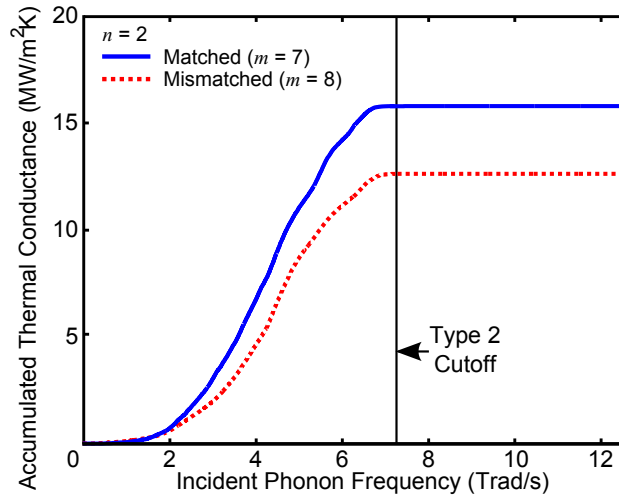


Figure 3.7: Accumulation of junction thermal conductance with frequency from the SBM for length-converged matched and mismatched cases.

introduced at the lead-junction and intrajunction interfaces [Fig. 3.4(d)].

We partially attribute the lead effect to ballistic transport of emergent modes of the superlattice junction. These modes travel ballistically across the junction and do not scatter from the intrajunction interfaces. Increasing temperature and the introduction of species defects at interfaces cause these emergent modes to scatter with one another and with the defects, resulting in attenuation of the lead effect. Increasing the superlattice period of the junction likewise attenuates the lead effect, suggesting that the effect can also be attributed to vibrational wave interference within the junction. The dependence of the lead effect on the superlattice period may be similar to the transition between coherent and incoherent regimes in a bulk superlattice.

As evidenced by the SBM calculations, the lead effect is also present in the zero temperature, harmonic limit (Fig. 3.5), but it is reversed. In this limit, the phonon transmission coefficients (and consequentially the thermal conductances) are highly dependent on the right lead mass (Fig. 3.6). It is not surprising that the lead effect can be altered by the introduction of finite temperature (and along with it, anharmonic interactions). It is surprising, however, that the effect of finite temperature is not simply to reduce the lead effect

until none can be observed. Instead, the reversal of the lead effect when comparing the SBM data to the NEMD data (Fig. 3.5) suggests the existence of a regime where finite temperature affects the matched and mismatched cases differently. In this intermediate regime, the effect of finite temperature appears to drive the junction thermal conductance of the matched case higher than that of the mismatched case. As discussed in Sec. 3.4 A, we performed NEMD simulations at average junction temperatures as low as 5 K for the case of $n = 2$ in an attempt to access this regime. We observed the same lead effect as at 20 K in all cases and did not notice any evidence of an appreciable attenuation or reversal. While direct heat method NEMD simulation does not provide concrete evidence of the reversal of the lead effect, the existence of the intermediate regime could be probed by modal anharmonic analysis of matched and mismatched cases in the temperature range of 0 to 5 K [81, 82, 83].

Graphene/hBN heterostructures

4.1 Introduction

Since its discovery, graphene has been the subject of intense experimental and theoretical study [84]. The lack of an electronic band gap, however, has stymied graphene's application in nanoelectronic devices. An avenue to graphene-based materials with tunable band gap is in-plane heterostructures built with other two-dimensional materials, such as hexagonal boron nitride (hBN). Using chemical vapor deposition, researchers have fabricated graphene/hBN heterostructures such as superlattices to a high degree of precision [7, 8].

Due to the need to dissipate heat in nanoelectronic devices, understanding the thermal properties of graphene/hBN heterostructures is critical. Thermal transport in graphene and hBN is dominated by phonons [85] and significant experimental and theoretical work has been done on bulk and nanostructured samples [85, 86, 87, 88, 89, 90, 91, 92, 93, 94]. Suspended graphene has an exceptionally high thermal conductivity, reported to be in the range 2,600-5,300 W/m-K experimentally [85, 86, 87] and as high as 3500 W/m-K computationally [88, 89]. Graphene supported by a substrate has a lower thermal conductivity. A computational study reported a value of 2450 W/m-K [90], while experimental values are reported to be between 370 and 600 W/m-K [91, 92]. Wang *et al.* measured the thermal conductivity of bilayer hBN to be 600 W/m-K [93], while computational studies report the intrinsic single-layer hBN thermal conductivity to be as high as 800 W/m-K [94]. Thermal transport across in-plane interfaces between graphene and hBN is not as well studied. To date, no experimental measurements have been made.

Computational studies of thermal transport across graphene/hBN interfaces have been

performed, all using the Tersoff interatomic potential [61, 95, 96, 97, 98]. Jiang and Wang [95] used nonequilibrium (NE) molecular dynamics (MD) (see Sec. 2.2.3) simulation to study in-plane islands of hBN embedded within a graphene sheet. They observed that the reduction of heat current across these structures varied linearly with the perimeter of the embedded object. Zhu and Ertekin performed NEMD simulations of armchair-aligned graphene/hBN superlattices. They studied periods ranging from 2 to 500 unit cells (0.5 to 125 nm at a temperature of 300 K). They observed a minimum in thermal conductivity at a period of 10 unit cells, suggesting that interference effects involving superlattice phonons are significant at such small periods. They also independently predicted an isolated armchair graphene/hBN interface conductance of 2.59 GW/m²K. da Silva *et al.* [96] used equilibrium MD simulations and normal mode decomposition to compute phonon lifetimes in armchair- and zig-zag-aligned graphene/hBN superlattices up to twenty unit cells in period. Their results indicate that the minimum in thermal conductivity is due to a reduction in phonon group velocity, a result that has been observed in other superlattice systems [56, 65, 67].

Due to the high Debye temperature of graphene (2,300 K for in-plane modes [99]), its room temperature thermal transport properties are strongly dependent upon quantum statistical effects, which cannot be captured by the MD techniques. Jiang and Wang recognized this limitation and explored graphene/hBN interfaces using the atomistic Green's function (AGF) technique, which is a harmonic, lattice-based, transfer matrix approach that can naturally include quantum statistics. They calculated the thermal conductance of armchair and zig-zag graphene/hBN interfaces to be 3.5 and 6.9 GW/m²K at a temperature of 300 K. Ong and Zhang [97] studied the armchair graphene/hBN interface using the AGF technique and found a thermal conductance of 3.59 GW/m²K at 300 K, in good agreement with Jiang and Wang. Building off of theoretical contributions made by Huang

et al. [100], Ong and Zhang computed transmission coefficients for phonon modes in the non-primitive rectangular Brillouin zones of graphene and hBN. They quantified the effect of off-normal phonon incidence on the transmission coefficient and decomposed the thermal conductance into contributions from transverse, longitudinal, and flexural modes. More recently, using the same method, Ong *et al.* calculated the thermal conductance of the boron (nitrogen) bonded zig-zag interface configuration to be 3.05 (3.42) GW/m²K at a temperature of 300 K [98].

In this chapter, we investigate phonon transport across a variety of heterostructures built from graphene and hBN by calculating the modal contributions to the thermal conductance using the scattering boundary method (SBM, see Sec. 2.4) [4, 26, 27, 28, 47]. In Sec. 4.2, we review the Landauer model of the interface, the geometry and configuration of the junctions considered, and the empirical potentials used to model the atomic interactions. In Sec. 4.3, we present and discuss results for (i) ideal interfaces between graphene and hBN along armchair and zig-zag directions, (ii) finite-length graphene/hBN superlattices, and (iii) substrated and bilayer junctions. We summarize our findings in Sec. 4.4.

4.2 Thermal conductance model

4.2.1 Landauer formalism

Using the Landauer formalism discussed in Sec. 2.4, we model a junction as a scattering source positioned between two phonon emitters, leading to a three-part domain composed of the left lead, the junction, and the right lead. The left and right leads are semi-infinite, behave as bulk crystals, and are at thermal equilibrium at temperatures T_L and T_R . Any deviations from equilibrium are so small that they can be ignored. Without loss of gener-

ality, we impose that $T_L > T_R$ so that the net flow of heat is from the left lead to the right lead through the junction. If we assume that the temperature difference $T_L - T_R$ is small so that $T_L \approx T_R = T$, the thermal conductance due to ballistic transport of phonons from the left lead to the right lead through the junction, G , can be written using the formula [45]

$$G = \frac{1}{\Delta} \int_{\substack{\boldsymbol{\kappa} \in \text{first} \\ \text{Brillouin} \\ \text{zone}}} \sum_{\nu}^{\text{Left, } +x} \hbar \omega(\boldsymbol{\kappa}, \nu) v_x(\boldsymbol{\kappa}, \nu) \frac{\partial f_{\text{BE}}}{\partial T} \alpha(\boldsymbol{\kappa}, \nu) d\boldsymbol{\kappa}. \quad (4.1)$$

The integral is taken over the first Brillouin zone of the left lead and the summation is taken over the phonon modes ν at a particular wavevector $\boldsymbol{\kappa}$ that have a positive group velocity component $v_x(\boldsymbol{\kappa}, \nu)$ in the cross-interface (i.e., x) direction. $\omega(\boldsymbol{\kappa}, \nu)$ and $\alpha(\boldsymbol{\kappa}, \nu)$ are the frequency and transmission coefficient associated with the phonon mode at $(\boldsymbol{\kappa}, \nu)$ and f_{BE} is the Bose-Einstein distribution. Δ is the out-of-plane thickness of the junction, which is 3.4 Å for single layer systems and 6.8 Å for bilayer systems.

The terms within Eq. (4.1) can be split into three parts. First, the integral is performed numerically by discretizing the hexagonal first Brillouin zone into a 40,000-point uniform rectangular grid. While the thermal conductance is converged to within 1% for a 10,000-point sampling of the first Brillouin zone, more points are used to achieve higher resolution in figures. Second, the $\omega(\boldsymbol{\kappa}, \nu)$ and $v_x(\boldsymbol{\kappa}, \nu)$ are bulk crystalline properties that are determined via HLD calculations (see Sec. 2.3). Third, the $\alpha(\boldsymbol{\kappa}, \nu)$ are junction properties that are determined by the SBM (see Sec. 2.4.2) [4, 26, 27, 28, 47].

All results presented in this paper are at a temperature of 300 K. We assume that phonon scattering in the junction involves only two-phonon processes that conserve energy and that phonon momentum is conserved up to the periodicity of the junction. Details regarding the application of the conservation rules are provided in Sec. 2.4.3. The uncertainty in our thermal conductance predictions is quantified by considering the convergence

of thermal conductance with the size of the junction. Convergence is assessed based on the length of the buffer region (see Sec. 2.4.2). The error is computed by comparing the thermal conductance of each junction Type to that of a prototype junction with a long buffer region and converged thermal conductance. Due to the computational expense associated with longer systems, the buffer region is 16 primitive unit cells (39.97 Å) long in the prototypes and 8 primitive unit cells (19.98 Å) long in the junctions discussed in this chapter. In the case of single-layer junctions, the prototype is an armchair graphene/hBN interface. In the case of bilayer junctions, the prototype is two armchair graphene/hBN interfaces. The errors are $\pm 4\%$ for single-layer and $\pm 9\%$ for bilayer.

4.2.2 Junction configurations and force constants

The required inputs to the SBM are the atomic structure of the junction and the second-order (i.e., harmonic) force constants that describe the atomic interactions in and between the leads and the junction. A list of all junctions considered is provided in Table 4.1. The lattice mismatch between graphene and hBN is resolved by isotropically straining the graphene, which has an unstrained lattice constant of 1.4388 Å[101], by 0.2363% to match the hBN lattice constant of 1.4422 Å[102]. The structure of the armchair and zig-zag graphene/hBN interfaces are shown in Fig. 4.1.

For intralayer interactions, we use the Tersoff interatomic potential [22] with parameters fit to bulk dispersions generated from first principles density functional theory calculations [101, 102]. The phonon dispersions for graphene and hBN along high-symmetry directions are plotted in Fig. 4.2. Of note is the phonon band gap in hBN between 215 and 235 Trad/s. The z -acoustic branches in both graphene and hBN are quadratic, the origin of which has been argued from symmetry considerations by Lifshitz [103]. Note that the thermal characteristic frequency $k_B T / \hbar$ at a temperature of 300 K is 39.4 Trad/s.

Type I junctions contain a perfect armchair (IA) or nitrogen-bonded zig-zag (IZ) interface between graphene and hBN. The masses of the three atomic species are the correct physical values, but the Tersoff parameters used for all interactions are identical. Specifically, those published by Lindsay and Broido for graphene [101].

Type II junctions are geometrically identical to Type I junctions, but we instead use Tersoff parameters specific to graphene [101] and hBN [102]. At the interface, the cross-species interaction parameters are computed according to the standard Tersoff mixing rules [104]. The introduction of mixing makes Type II junctions a more realistic model of graphene/hBN interfaces than Type I junctions. In junctions IIA-S and IIZ-S, an on-site potential is added to model the presence of a substrate. For the i^{th} atom in the N^{th} unit cell, this potential has the form

$$U_{\text{Substrate},N,i} = \frac{1}{2}k_z z_{N,i}^2, \quad (4.2)$$

where $z_{N,i}$ indicates the displacement along the z (i.e., out of plane) direction. k_z is chosen to be 16 N/m to represent a typical van der Waals interaction between single-layer graphene and a substrate [105].

In both Type I and Type II junctions, we show results only for boron-bonded zig-zag interfaces. Nitrogen-bonded zig-zag interfaces are also possible. Because our choice of Tersoff parameters for hBN applies an average of B-N-B and N-B-N bond coefficients to all bonds, we observe no discernable difference in thermal conductance between the two structures.

Type III junctions are finite-length superlattices composed of alternating layers of graphene and hBN. The armchair-aligned superlattice unit cell is built from two atomic layers of hBN attached to two layers of graphene, forming a 2×2 unit cell. The unit cell is then repeated n times to form a $2 \times 2 \times n$ junction, where n ranges from 1 to 18. These

Type	Left Lead	Right Lead	Junction	Mixing	Layering	Junction Conductance (GW/m ² K)
IA	G	G'	Armchair	None	Single	5.56 ± 0.22
IZ	G	G'	Zig-zag	None	Single	5.46 ± 0.22
IIA	G	BN	Armchair	Tersoff	Single	3.67 ± 0.15
IIA-S	G	BN	Armchair	Tersoff	Substrate, $k_z = 16$ N/m	3.16 ± 0.13
IIZ	G	BN	Zig-zag	Tersoff	Single	3.70 ± 0.15
IIZ-S	G	BN	Zig-zag	Tersoff	Substrate, $k_z = 16$ N/m	3.19 ± 0.13
IIIA	G	BN	Armchair $2 \times 2 \times n$ Superlattice	Tersoff	Single	See Fig. 4.5
IVA-1	G	G	Armchair $2 \times 2 \times (n + 1/2)$ Superlattice	Tersoff	Single	
IVA-2	G-G	BN-BN	Armchair	Tersoff + LJ	Bilayer	3.38 ± 0.30
	G-G	BN-G	Armchair	Tersoff + LJ	Bilayer	4.31 ± 0.39

Table 4.1: Junction configurations considered. G and BN indicate the Broido *et al.* [101] and Sevik *et al.* [102] Tersoff interaction parameters for graphene and hBN. G' indicates a system using graphene Tersoff parameters but with hBN atomic masses. In cases where both graphene and hBN use the same Tersoff parameters, no cross-interface mixing is used. Otherwise, appropriate mixing rules are applied.

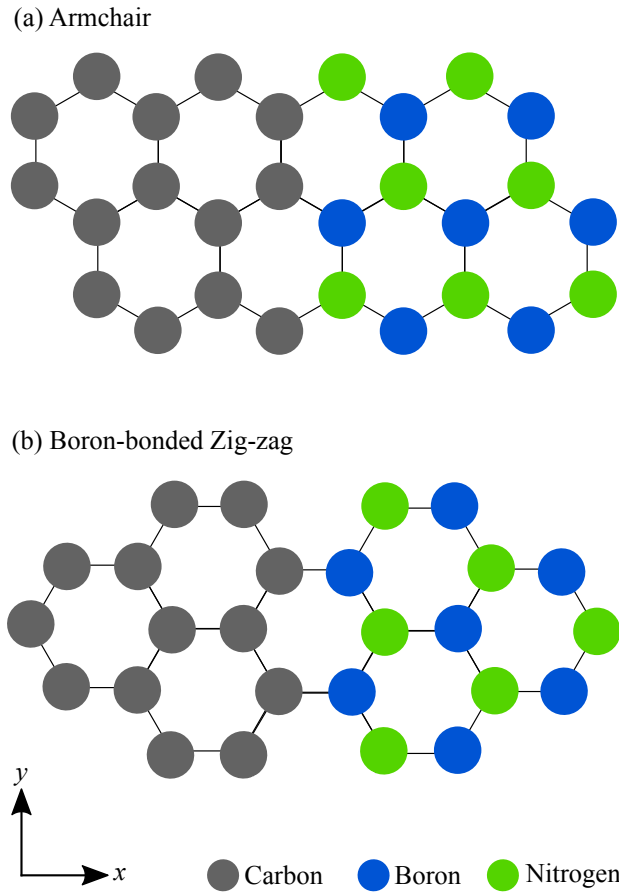


Figure 4.1: Graphene/hBN interfaces: (a) armchair and (b) boron-bonded zig-zag.

$2 \times 2 \times n$ junctions have mismatched graphene and hBN leads. To study the effect of having matched leads, each $2 \times 2 \times n$ junction has a $2 \times 2 \times (n + 1/2)$ counterpart, which has an additional two atomic layers of hBN, such that both leads are graphene. The interatomic interactions in the Type III junctions are the same as those in the Type II junctions.

Type IV junctions are bilayer systems created using AB (Bernal) stacking [106]. Type IVA-1 is an armchair graphene/hBN interface over an identical armchair graphene/hBN interface. In Type IVA-2, the bottom layer is graphene and the top layer is an armchair hBN-graphene interface. The intralayer interactions in the Type IV junctions are identical to those used in the Type II and III junctions and the interlayer interactions are modeled using a 12-6 Lennard-Jones potential with ϵ and σ values of 3.85×10^{-22} J and 3.4 \AA [105].

4.3 Results

4.3.1 Junction Types I and II: Cross-interface interaction

The acoustic mismatch and diffuse mismatch models for predicting interface thermal conductance [3] ignore the cross-interface interaction. They instead attempt to describe interfaces using only the bulk properties of the adjoining materials. It is well-known that these techniques can be inaccurate when compared to ones that incorporate a detailed cross-interface interaction [4, 107, 108]. We use the SBM to quantify the difference in thermal conductance between a model where only mass properties differ (Type I) to a higher-fidelity model that incorporates mixed interactions across the interface (Type II). In Type I junctions, the predicted thermal conductance is 5.56 ± 0.22 GW/m²K for armchair and 5.46 ± 0.22 GW/m²K for zig-zag. In Type II junctions, the predicted thermal conductance is 3.67 ± 0.15 GW/m²K for armchair and 3.70 ± 0.13 GW/m²K for zig-zag. Even with an identical interface geometry, the addition of a physically realistic cross-species interaction and a more accurate potential for hBN reduces the predicted thermal conductance by 40-50%. If classical statistics are used in the evaluation of Eq. (4.1), the thermal conductances of Type IIA and Type IIZ junctions are 11.6 ± 0.46 and 12.0 ± 0.48 GW/m²K, three times the values predicted using quantum statistics. The use of the correct Bose-Einstein statistics is thus critical when predicting thermal conductance at a temperature of 300 K.

The Type IIA armchair junction thermal conductance is within 2% of the value reported by Ong *et al.*, who also used graphene- and hBN-specific Tersoff potentials and mixing rules at the interface [97]. For the Type IIZ junction, the difference in our thermal conductances between the nitrogen-bonded and boron-bonded variants is small enough as to be within their uncertainties. Our Type IIZ zig-zag thermal conductance is 8% larger than the nitrogen-bonded value reported by Ong *et al.* and 20% larger than their value for the

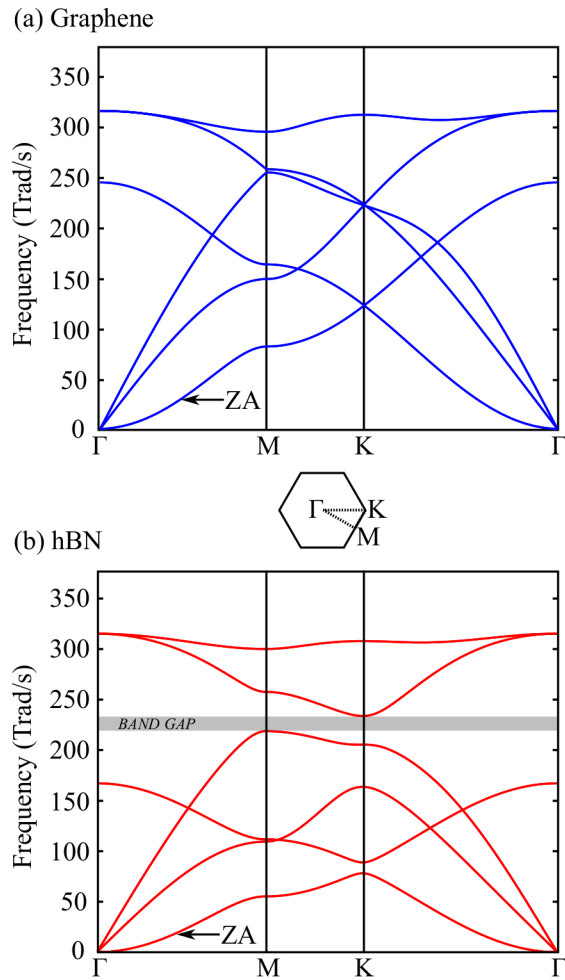


Figure 4.2: Phonon dispersion along the high symmetry loop Γ -M-K- Γ in the first Brillouin zone of (a) graphene and (b) hBN using force constants from the Tersoff potential. The quadratic z -acoustic (ZA) branch is indicated for both systems. The band gap in hBN is highlighted. Both graphene and hBN are at a lattice constant of 1.4422 \AA

boron-bonded case [98]. We attribute this difference to differences in Tersoff parameters. Specifically, their parameter set distinguishes between N-B-N and B-N-B angular bonds while ours does not.

The Landauer integrand [Eq. (4.1)] throughout the first Brillouin zone is shown for the Type I junctions in Figs. 4.3(a) and 4.3(b) and for the Type II junctions in Figs. 4.3(c) and 4.3(d). Despite the significant differences in how the integrands are distributed across the first Brillouin zone, the total thermal conductances of the armchair and zig-zag inter-

faces are within their uncertainties for each type. As expected, common to all integrands is symmetry about $\kappa_y = 0$ and asymmetry about $\kappa_x = 0$. Type I junctions have larger integrands throughout the first Brillouin zone when compared to Type II junctions and a slower decrease in the integrand from the Γ -point to the zone edge. This effect is due to the homogenous interaction environment in Type I that is broken by the Tersoff mixing rules in Type II. Such a homogenous environment allows the transmission coefficients to be higher for most modes.

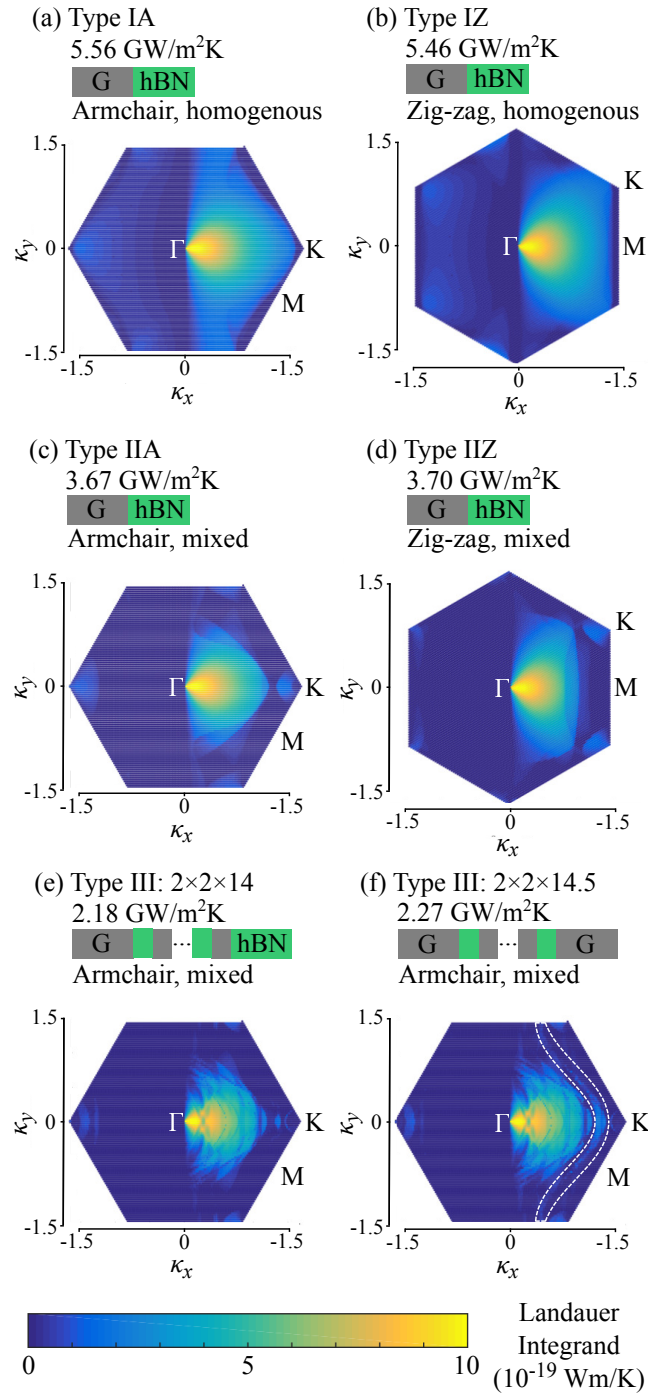


Figure 4.3: The Landauer integrand [Eq. (4.1)] throughout the graphene first Brillouin zone for the (a) Type IA, (b) Type IZ, (c) Type IIA, (d) Type IIZ, (e) Type III: $2 \times 2 \times 14$, and (f) Type III: $2 \times 2 \times 14.5$ junctions. κ_x and κ_y are given in units of \AA^{-1} . In (f), the white dashed line highlights contributions of modes whose frequencies lie within the hBN band gap. These modes contribute in cases of matched leads (f), but not in cases of mismatched leads (e).

All Type II integrands show significant contributions to thermal conductance for $\kappa_x > 0$ (89 and 92% of the total for Types IIA and IIZ). The most significant contributions to thermal conductance come from wavevectors near the Γ -point, where the acoustic modes are highly populated and have high group velocities and transmission coefficients. In fact, 60% of the thermal conductance for both Type II junctions comes from acoustic phonon modes with frequencies less than 100 Trad/s. The contribution decays for large ratios of $|\kappa_y/\kappa_x|$ (i.e., large incidence angles) and large wavevector magnitudes.

The small contribution from the left half of the first Brillouin zone ($\kappa_x < 0$) is because the majority of those modes have negative cross-interface group velocity $v_{g,x}$. These modes do not contribute to the summation in Eq. (4.1). As shown in Fig. 4.2, for modes with $\kappa_x < 0$, the only contributors to thermal conductance are the three optical branches with positive $v_{g,x}$ near the zone edge along K- Γ and, to a lesser extent, M- Γ . In both Type II junctions, the Landauer integrand extinguishes for all wavevectors greater than 1 \AA^{-1} , with the exception of small contributions at the K points. The zig-zag interface differs from the armchair interface in the drop off of the Landauer integrand with respect to incidence angle. This drop off occurs sharply at $|\kappa_y/\kappa_x| = 1$ for the zig-zag case, while there is little angular drop off in the armchair case.

The accumulation of thermal conductance with respect to mode frequency for the armchair interface is plotted in Fig. 4.4(a). The zig-zag interface is qualitatively identical. We distinguish between in-plane (IP) and out-of-plane (OP) modes by projecting the real portion of the normalized mode eigenvector onto the z unit vector. If the result is greater than 0.5, we consider the mode OP, otherwise, we consider it IP. The OP modes, which are a third of all modes, contribute 32% to the total thermal conductance. The modal contributions to thermal conductance are plotted in Fig. 4.4(b). At frequencies near zero (i.e., the Γ -point), the OP modes contribute nothing as the ZA branch has zero group velocity due

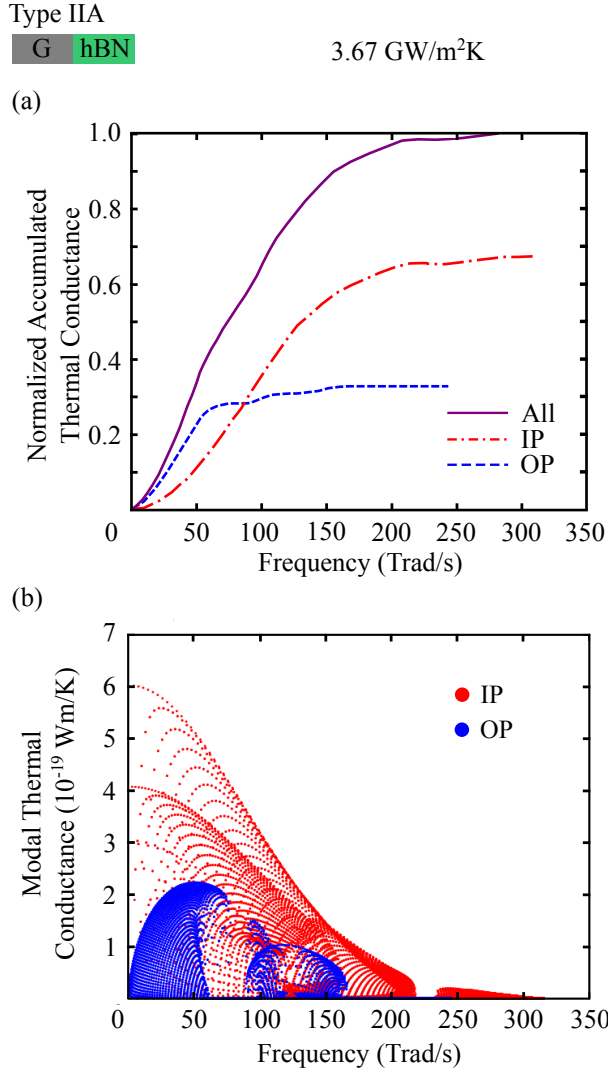


Figure 4.4: (a) Accumulation and (b) modal contribution to thermal conductance as a function of frequency for Type IIA junctions. Note that the characteristic thermal frequency at 300 K is 39.2 Trad/s.

to its quadratic shape, see Fig. 4.2(a). Their contributions peak at 40 Trad/s due to the increasing group velocity but decreasing Bose-Einstein population. The OP thermal conductance accumulation saturates near 150 Trad/s, corresponding to the highest frequency of graphene’s ZA branch. There are steep drop offs in the conductance contribution of the OP modes at 50-100 Trad/s and between 110-140 Trad/s. These drop offs are due to changes in the transmission coefficient, which often varies dramatically between near unity

and zero, and stand in contrast to the lack of modal transmission at 215-235 Trad/s, which is due to the hBN band gap. Whereas most of the OP contribution to thermal conductance comes at frequencies lower than 75 Trad/s, IP contributions are more evenly distributed throughout the frequency range. At low frequency, individual IP modes contribute highly, but there is a low density of states. Between 100 and 200 Trad/s, the IP density of states increases, but the single mode contributions decrease due to low group velocity. Only IP modes exist above the hBN band gap and are responsible for all transmission above 235 Trad/s.

4.3.2 Junction Type III: Finite superlattices

The thermal conductance of the graphene/hBN superlattice junctions as a function of the number of periods is plotted in Fig. 4.5. The addition of a single 2×2 superlattice period into a perfect armchair interface between graphene and hBN decreases the junction thermal conductance by 10% from 3.67 to 3.24 GW/m²K. This decrease is much smaller than the 66% reduction predicted from a series conductance model that assumes that the introduction of a single superlattice period increases the number of isolated graphene/hBN interfaces from one to three. The thermal conductance continues to decrease as more periods are added. The rate of decrease becomes smaller as period number increases. For ballistic transport (as assumed here) in the limit of a large number of periods, the thermal conductance will converge to a value representative of an infinite superlattice. We see this convergence as the superlattice approaches 18 periods, with matched and mismatched trends converging to 2.2 and 2.1 GW/m²K. As was the case with the Type I and II junctions, acoustic modes near the Γ point dominate in their contribution to the thermal conductance of superlattice junctions, see Figs. 4.3(e) and 4.3(f). At all period numbers considered, modes less than 100 Trad/s in frequency account for no less than 71% of the

total thermal conductance.

The matched leads $[2 \times 2 \times (n + 1/2)]$ superlattice junctions consistently have higher thermal conductance than the corresponding mismatched leads $(2 \times 2 \times n)$ junctions. Thus, despite having an additional two atomic layers within the junction, changing the leads to graphene/graphene from graphene/hBN causes the thermal conductance to be greater than that of the shorter mismatched case. We previously observed this effect in finite superlattice junctions built from Lennard-Jones solids [48]. Though the current system differs from that study in that it is two-dimensional and incorporates cross-interface interaction mixing, the effect is still observed. The origin of this effect can be understood by considering the distribution of the Landauer integrand across the first Brillouin zone for the $2 \times 2 \times 14$ and $2 \times 2 \times 14.5$ cases. As shown in Figs. 4.3(e) and 4.3(f), the superlattice junction integrand distributions contain an abundance of peaks and valleys, in contrast to those for the simple interfaces shown in Figs. 4.3(a)-4.3(d), which have a single, central peak at the Γ point and uniform decay. This added structure is caused by interference effects in the superlattice junctions that are absent from the single interfaces.

The difference between the matched and mismatched lead superlattice junctions is more subtle. The two cases differ primarily due to a band of high transmission found in the matched case forming an arc starting at $(\kappa_x, \kappa_y) = (0.5, -1.5) \text{ \AA}^{-1}$, going through $(1.4, 0) \text{ \AA}^{-1}$, and ending at $(0.5, 1.5) \text{ \AA}^{-1}$. This band is absent from the mismatched case and corresponds to phonon transmission from the highest transverse acoustic branch and second to highest transverse optical branch in graphene [see Fig. 4.2(a)]. Between 215 and 235 Trad/s, these two graphene branches have no matching branches in hBN due to its band gap. As a result, in the mismatched leads cases, there are no energy conserving transmission pathways available to these phonon modes.

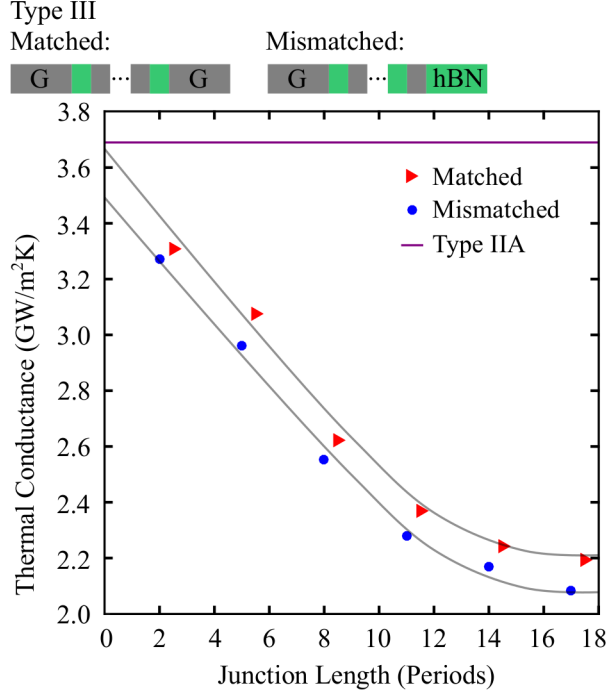


Figure 4.5: Thermal conductance of Type III junctions as a function of the number of superlattice periods. The purple line corresponds to a single graphene/hBN interface. The gray lines serve as a guide for the eye.

4.3.3 Junction Types II-S and IV: Substrates and bilayers

A simple model for estimating the junction thermal conductance of a bilayer system is to consider the two layers as independent parallel channels. Because we report thermal conductance on a per area basis [see Eq. (4.1)], the thermal conductance G_{Parallel} is then the arithmetic average of the two isolated single layer conductances, G_{Top} and G_{Bottom} ,

$$G_{\text{Parallel}} = \frac{G_{\text{Top}} + G_{\text{Bottom}}}{2}. \quad (4.3)$$

In reality, interactions between the layers cause the actual thermal conductance G to deviate from G_{Parallel} by

$$G = G_{\text{Parallel}} + \Delta G_{\text{Interaction}}, \quad (4.4)$$

where $\Delta G_{\text{Interaction}}$ is negative. We quantify $\Delta G_{\text{Interaction}}$ by comparing the thermal conductances of bilayer Type IV and substrated II-S junctions to those of the Type II junctions coupled through the parallel transport model.

We consider two bilayer systems. The Type IVA-1 junction is a graphene/hBN armchair interface over an identical graphene/hBN armchair interface, while the Type IVA-2 junction is a graphene/hBN armchair interface over a layer of graphene. In both cases, zone-center acoustic phonon modes are again the dominant contributors to the thermal conductance. Modes with frequencies less than 100 Trad/s in Type IVA-1 and IVA-2 junctions contribute 72 and 78% to the total. For junction Type IVA-1, G_{Top} is identical to G_{Bottom} and is 3.67 GW/m²K, so that G_{Parallel} is 3.67 GW/m²K. The SBM result is 3.38 ± 0.30 GW/m²K, giving a $\Delta G_{\text{Interaction}}$ of -0.29 GW/m²K. For junction Type IVA-2, G_{Top} is again 3.67 GW/m²K, while G_{Bottom} is 5.87 GW/m²K [representing the phonon radiation limit, i.e., when all α in Eq. (4.1) are unity]. G_{Parallel} is then 4.77 GW/m²K while the SBM result is 4.31 ± 0.39 GW/m²K, giving a $G_{\text{Interaction}}$ of -0.46 GW/m²K. Unlike in bilayer graphene, where the addition of a second layer reduces the thermal conductivity by nearly an order of magnitude [91, 92], the addition of a second layer reduces the thermal conductance of graphene/hBN interfaces by less than 10%.

The effect of the interlayer interaction can be understood by considering the modal transmission coefficients as a function of frequency for the single-layer and bilayer systems, as plotted in Figs. 4.6(a)-4.6(c). Aside from the doubling of the number of modes from a single-layer to a bilayer system, the transmission coefficient plots for Type IIA and Type IVA-1 junctions are nearly indistinguishable. The most notable differences are the reduced transmission coefficients near 50 Trad/s and in the region 250-300 Trad/s in the Type IVA-1 junction. In the Type IVA-2 junction, the transmission coefficients shown in Fig. 4.6(c) can be decomposed to those in the range 0.5 to 1, where the profile closely replicates that

of the Type IIA system, and those in the range 0 to 0.5, where the great number of modes at 0.5 suggest a similarity to single-layer graphene, where all transmission coefficients are unity. These qualitative similarities suggest that many modes are largely unaffected by the interlayer interaction. This is not the case for all modes, the most obvious of which are the modes with transmission coefficients that lie between 0 and 0.5. Since they do not fit either the Type IIA profile or the single-layer graphene profile, they are influenced by the bilayer interaction in a non-trivial manner. It is the reduction in the transmission coefficient of these modes that creates a negative $\Delta G_{\text{Interaction}}$. The limitation of $\Delta G_{\text{Interaction}}$ to only 10% of the single-layer value can be attributed to the weakness of the van der Waals interlayer interaction.

The Type II-S junctions, where the substrate is modeled by an on-site potential, represent a simpler computational approach for capturing the bilayer interaction. The thermal conductances of the substrated Type IIA-S and Type IIZ-S junctions are 3.16 ± 0.13 and 3.19 ± 0.13 GW/m²K, a decrease from the monolayer Type IIA and Type IIZ junctions of 15%. This reduction is similar in magnitude to the 9 and 11% reductions observed in the explicit bilayer calculations. Two thirds of this decrease comes from the contributions of the OOP modes. The primary effect of the substrate interaction is to lift the ZA branch from 0 to 25 Trad/s at the Γ point, so that these modes are less populated. Accompanied with this change is a reduction of $v_{g,x}$ of the ZA branch from Γ to K and Γ to M. A similar effect is seen in the explicitly modeled bilayer systems, where the second layer lifts the ZA branch from 0 to 18 Trad/s [90]. Indeed, the change to the ZA branch is the only major alteration to the dispersion when a second layer of either graphene/hBN (Type IVA-1) or graphene (Type IVA-2) is added. The accuracy of the simple substrate model lies in its ability to capture this change in the dispersion.

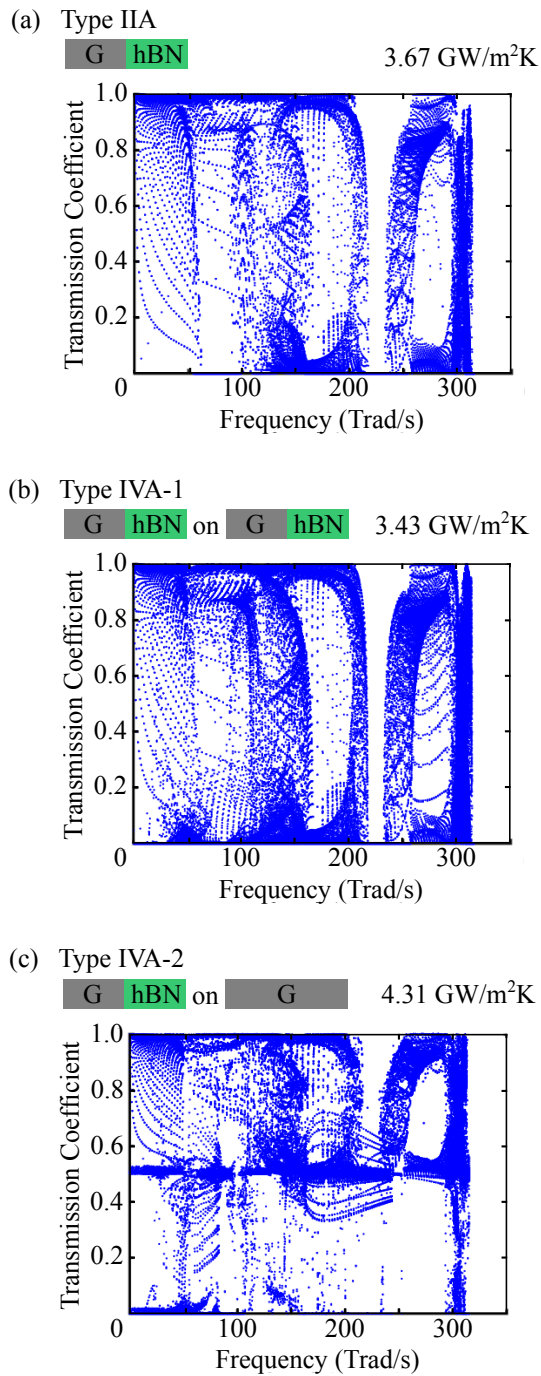


Figure 4.6: Modal transmission coefficient versus frequency for (a) Type IIA, (b) Type IVA-1 and (c) Type IVA-2 junctions and their corresponding thermal conductances as calculated from the SBM.

4.4 Summary

In this chapter, we used the SBM to compute mode-resolved transmission coefficients of phonon modes. We found that the primary contributors to the thermal conductance of graphene/hBN heterostructures are acoustic phonon modes with frequencies below 100 Trad/s. These modes have high group velocity, high population, and transmission coefficients near one [see Figs. 4.4(a) and 4.4(b)]. The use of an accurate cross-interface interaction and quantum statistics dramatically impact the interface thermal conductance. Ignoring the former increases the prediction by a factor of 1.5, while ignoring the latter increases it three-fold. The thermal conductances of the isolated armchair and zig-zag graphene/hBN interfaces correspond to a Kapitza length of 700 nm of single-layer graphene based on a thermal conductivity of 2,600 W/m-K [87]. While the thermal resistance of such interfaces is significant compared to bulk graphene, the thermal conductances are one to two orders of magnitude larger than typical interface conductances in three-dimensional materials, which range from tens to hundreds of MW/m²K [3].

The thermal conductance of a finite graphene/hBN superlattice junction depends on the superlattice length and the lead species. As shown in Fig. 4.5, junctions with matched graphene/graphene leads have a 5 to 10% greater thermal conductance than comparable junctions with mismatched graphene/hBN leads. This difference is a result of transmission that occurs in the matched lead case but cannot occur in the mismatched lead case due to the hBN band gap. This lead effect is a consequence of our assumption of harmonic interactions, but because the Debye temperatures of both graphene and hBN are high, such behavior may be observable at room temperature.

Finally, we found that the thermal conductances of explicitly-modeled bilayer junctions of graphene/hBN do not differ greatly from those predicted from simpler models (e.g., an independent parallel transport model or a single-layer with an on-site potential). The

strength of the intralayer van der Waals interaction is not strong enough to cause significant coupling between the layers. Since the intralayer interactions are far softer than the interlayer interactions, however, anharmonic effects could be significant at room temperature, which may increase the thermal conductance of a real bilayer junction [74].

C₆₀ molecular crystal

5.1 Introduction

C₆₀ buckminsterfullerene is a spherical molecule of covalently-bonded carbon atoms often referred to as a cage. The centers of mass of a bulk sample of C₆₀ will self-organize into a crystal. At temperatures below 260 K, bulk C₆₀ has a rotationally-ordered simple cubic structure with a four cage unit cell. A transition occurs as the temperature surpasses 260 K, where the rotationally aligned C₆₀ begins to rotate freely. While the centers of mass do not move from the low temperature structure, but the high temperature, rotationally disordered structure now forms an FCC crystal [109]. Though C₆₀ was first synthesized in 1985, it has recently attracted great attention due to its possible application in devices [110]. First, due to its strong absorption in the visible and ultraviolet regimes, it has possible applications in organic photovoltaics [111, 112]. Second, due to the low thermal conductivity of C₆₀, it has possible applications as a thermal insulator and possibly as an organic thermoelectric material [113]. Third, it is relatively easy to modify the electronic and magnetic properties of C₆₀ by chemically functionalizing the cage with atoms, ions, or molecules. A commonly used derivative of C₆₀ is phenyl-C₆₁-butyric acid methyl ester (PCBM), where a C₆₀ is functionalized with an organic molecule to allow for solution-based fabrication [114].

The thermal conductivity of the bulk C₆₀ crystal is critical to the performance and function of potential C₆₀-based devices. Only a handful of measurements of been performed of C₆₀'s thermal conductivity. In 1992, Yu *et al.* used a steady-state single heater method and reported a thermal conductivity of 0.4 W/m-K, a value that was temperature-

independent for temperatures of 260 K and above [9, 16]. Later on, the 3ω method was used on a C_{60}/C_{70} alloy and a thermal conductivity of 0.1 W/m-K was reported at room temperature [115]. Wang *et al.* reported a similar thermal conductivity of 0.1 W/m-K for disordered C_{60} at room temperature [115]. Measurements on the C_{60} derivative PCBM have resulted in thermal conductivities in the range 0.03-0.06 W/m-K [116, 117]. Chen *et al.* performed direct method MD simulations on face-centered cubic C_{60} and hexagonal close-packed PCBM using the polymer consistent force-field (PCFF) and reported room temperature thermal conductivities of 0.2 and 0.075 W/m-K, representing the only published computational work on C_{60} thermal conductivity thus far [118]. They concluded that the much smaller thermal conductivity of PCBM as compared to C_{60} was due to the scattering of long wavelength C_{60} phonons by the functional group.

In this chapter, we study the mechanisms of thermal transport in crystalline C_{60} using MD simulation. Specifically, we consider the impact of the degrees of freedom of a single C_{60} (vibrational, rotational, center-of-mass translation) on the thermal conductivity of a bulk crystal. Even without the added complexity of functional groups, the physics of C_{60} is rich at room temperature due to the free rotation of the cages. A requirement of the crystal description of a solid (and the phonon description of thermal transport) is that the atoms only deviate slightly from an equilibrium position (See Section 2.3). The free rotation of the cages represents a large displacement, hence, at room temperature, it is only appropriate to treat the translations of the centers-of-mass of the C_{60} as a crystal, while the cage rotations and intra-cage vibrations do not fit the phonon picture. By predicting the thermal conductivity separately for full degree of freedom C_{60} crystal and point mass C_{60} crystal (where both intra-cage vibrations and cage rotations are removed), we explore the impact of the non-crystal-like degrees of freedom on thermal conductivity.

The remainder of the chapter is organized as follows. In Sec. 5.2, we describe the

structure and interaction potentials used to model the two forms of C_{60} . In Sec. 5.3, we describe details regarding the MD simulations performed. In Sec. 5.4, we present thermal conductivity results and conclude in Sec. 5.5.

5.2 C_{60} model

5.2.1 Structure

To generate the structure of a single C_{60} molecule, shown in Fig. 5.1, we use the program specified by Senn, which is briefly described here [119]. The positions of the atoms are calculated based on the vertices of a truncated icosahedron of the appropriate size. We first specify the parameters defining the size of the cage. Two bond lengths are required. First, $r_6 = 1.391 \text{ \AA}$ is the length of the carbon-carbon double bond. Second, $r_5 = 1.455 \text{ \AA}$ is the length of the carbon-carbon single bond. The radius of the circumscribed sphere of the icosahedron is then

$$r_{12} = \left(r_5 + \frac{1}{2}r_6 \right) \frac{\sqrt{5 + \sqrt{5}}}{2}. \quad (5.1)$$

The positions of ten of the twelve vertices of the icosahedron are given by

$$X_k = \frac{2r_{12}}{\sqrt{5}} \cos k\delta, \quad (5.2)$$

$$Y_k = \frac{2r_{12}}{\sqrt{5}} \sin k\delta, \quad (5.3)$$

$$Z_k = (-1)^k \frac{r_{12}}{\sqrt{5}}, \quad (5.4)$$

where $\delta = 36^\circ$. The integer index k ranges from 1 to 10. The two remaining vertices are $[X_{11}, Y_{11}, Z_{11}] = [0, 0, -r_{12}]$ and $[X_{12}, Y_{12}, Z_{12}] = [0, 0, r_{12}]$. We can now compute the positions of two unique carbon atoms on a C_{60} by considering pairs of connected vertices

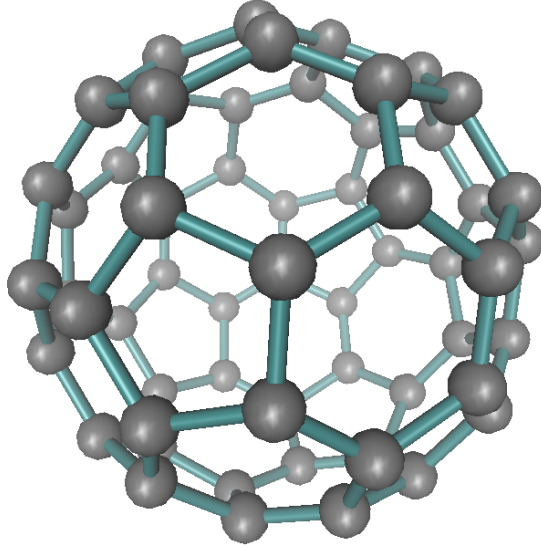


Figure 5.1: A single C_{60} molecule, viewed along the z -axis of construction.

k and j . The n^{th} carbon atom is located at

$$x_n = X_j + \left(\frac{r_5}{2r_5 + r_6} \right) (X_k - X_j), \quad (5.5)$$

$$y_n = Y_j + \left(\frac{r_5}{2r_5 + r_6} \right) (Y_k - Y_j), \quad (5.6)$$

$$z_n = Z_j + \left(\frac{r_5}{2r_5 + r_6} \right) (Z_k - Z_j). \quad (5.7)$$

That is, using Eq. 5.7 with a non-repeating choice of two vertices k and j as input will generate the position of a carbon atom. The choice of coordinate system places the center-of-mass of the C_{60} molecule at $[0, 0, 0]$.

5.2.2 Polymer consistent force-field

Once the structure of a single C_{60} molecule is defined, it is necessary to define the bonded interactions on the cage. We use the PCFF, a subclass of the `class2` potential in LAMMPS [30]

$$U_{\text{PCFF}} = (U_{\text{Bond}} + U_{\text{Angle}} + U_{\text{Dihedral}})_{\text{Bonded}} + U_{\text{vdW}}. \quad (5.8)$$

The first three terms on the right-hand side of Eq. 5.8 represent the bonded intra-cage interactions, while the last term represents the non-bonded van der Waals interaction that couples different cages. PCFF parameters are traditionally tabulated in energy units of Kcal/mol. All parameters are taken from LAMMPS documentation or Ref. [29].

We will specify the forms and parameters of U_{PCFF} term by term. The first term in the bonded portion of Eq. 5.8 is the two-body bond term U_{Bond} . It is composed of the single and double covalent bonds between nearest neighbor carbon atoms

$$U_{\text{Bond}} = \sum U_{2,\text{Single}} + \sum U_{2,\text{Double}}. \quad (5.9)$$

The summations are performed over all single and double bonds. Both $U_{2,\text{Single}}$ and $U_{2,\text{Double}}$ have the same form U_2 ,

$$U_2 = K_2(r - r_0)^2 + K_3(r - r_0)^3 + K_4(r - r_0)^4, \quad (5.10)$$

where r represents the distance between the bonded atoms. For $U_{2,\text{Single}}$, $r_0 = r_5 = 1.455$ Å, $K_2 = 299.67$ Kcal/mol-Å², $K_3 = -501.77$ Kcal/mol-Å³, and $K_4 = 679.81$ Kcal/mol-Å⁴. For $U_{2,\text{Double}}$, $r_0 = r_6 = 1.391$ Å while other parameters remain the same.

The second term in the bonded portion of Eq. 5.8 is the three-body angle term U_{Angle} . It is composed of angular bonds between three carbon atoms. Note that, in a C_{60} molecule,

three-atom chains form on the perimeter of either pentagons or hexagons, hence

$$U_{\text{Angle}} = \sum U_{3,108} + \sum U_{3,120} , \quad (5.11)$$

where $U_{3,108}$ represent the in-pentagon bonds and $U_{3,120}$ represent the in-hexagon bonds. The summations are performed over all occurrences of the two types of angles. Both $U_{3,108}$ and $U_{3,120}$ have the same form U_3 ,

$$U_3 = [Q_2(\theta - \theta_0)^2 + Q_3(\theta - \theta_0)^3 + Q_4(\theta - \theta_0)^4] + [N_1(r_{ij} - r_1)(\theta - \theta_0) + N_2(r_{jk} - r_2)(\theta - \theta_0)] . \quad (5.12)$$

Each three-atom chain is defined by a central atom and two edge atoms. θ is the smaller angle formed by the two lines connecting the central atom with the edge atoms. r_{ij} is the distance between the central atom and the first edge atom, while r_{jk} is the distance between the central atom and the second edge atom (the labeling of first and second edge atoms is irrelevant for C_{60}). For the three-atom chains existing in a hexagon, $\theta_0 = 120^\circ$, $Q_2 = 39.52$ Kcal/mol-deg², $Q_3 = -7.44$ Kcal/mol-deg³, $Q_4 = -9.56$ Kcal/mol-deg⁴, $N_1 = N_2 = 8.02$ Kcal/mol-deg-Å and $r_1 = r_2 = 1.423$ Å. For three-atom chains existing in a pentagon, $\theta_0 = 108^\circ$ while all other parameters are identical to the hexagon case.

The final term on the right-hand side of Eq. 5.8 is the non-bonded van der Waals interaction. It is specified by a 9-6 Lennard-Jones potential,

$$U_{\text{vdW}} = \sum \epsilon \left[2 \left(\frac{\sigma}{r} \right)^9 - 3 \left(\frac{\sigma}{r} \right)^6 \right] , \quad (5.13)$$

where the summation is performed over all pairs of atoms (both within a cage and between cages). The energy and distance parameters ϵ and σ are 0.054 Kcal/mol and 4.01 Å. U_{vdW} is strictly cut off at distances beyond 15.5 Å, encompassing the center-of-mass of the

second-nearest neighbor cage.

After the PCFF as defined is applied to the structure constructed in Sec. 5.2.1, single-cage relaxation is performed using MD simulation. After relaxation, the relaxed average bond lengths at a temperature of 300 K are $r_6 = 1.422 \text{ \AA}$ and $r_5 = 1.498 \text{ \AA}$. A bulk system is then built by placing the centers-of-mass of multiple cages in a FCC crystalline arrangement where the rotational orientation of each cage is uniformly randomized over the three Euler angles. Relaxation is performed at 300 K and the zero pressure conventional face-centered cubic lattice constant is found to be 14.387 \AA , which is comparable to the experimental lattice constant of 14.17 \AA .

5.2.3 Point mass

To isolate the center-of-mass translations of the C_{60} cages independent of all intra-cage vibrations and cage rotations, we model each C_{60} molecule as a point whose mass is sixty times that of a single carbon atom. The challenge involved in creating this reduced order model is the definition of the effective pair potential $U_{\text{Eff}}(r)$ between C_{60} two molecules. In the full degree of freedom model, this was done by calculating the exact inter-atomic interactions and summing them. However, in the point mass model, the individual atoms are not modeled and it is necessary for $U_{\text{Eff}}(r)$ to capture the average effect of the angular disorder in the system. We compute the interaction energy between a pair of rigid C_{60} molecules whose centers-of-mass are separated by a distance r atomistically by summing the interaction energy across all interacting atoms. Call this quantity $U_l(r)$, where the index l indicates the rotational orientation of one C_{60} relative to the other (i.e., l is shorthand for three Euler angles). We choose W random orientations and create $U_{\text{Eff}}(r)$ by taking

the weighted average of the $U_l(r)$ over all orientations considered

$$U_{\text{Eff}}(r) = \frac{\sum_l^W U_l(r) \exp[-\min(U_l)/k_B T]}{\sum_l^W \exp[-\min(U_l)/k_B T]}. \quad (5.14)$$

Here, $\min(U_l)$ is the minimum energy (i.e., well depth) of $U_l(r)$ for the particular orientation l . Eq. 5.14 forms $U_{\text{Eff}}(r)$ by weighing each orientational pair energy $U_l(r)$ by the Boltzmann factor of their energy minimum. For our work, W is taken to be 1,000. To ensure that 1,000 is sufficient for statistical convergence, five different random sequences of 1,000 orientations were used to generate five different versions of $U_{\text{Eff}}(r)$. The maximum deviation between any two of the five potentials was 2% throughout the range of r . $U_{\text{Eff}}(r)$ is sampled at 2,000 evenly spaced points between $r = 5$ and 25 \AA and implemented in LAMMPS using the command `pair_style table linear` (i.e., a lookup table). $U_{\text{Eff}}(r)$ is plotted in Fig. 5.2

The method of generating $U_{\text{Eff}}(r)$ presented here is not the only method, though it provides for a simple way to sample the rotational phase space experienced by a single C_{60} molecule within the FCC environment. It is also possible to sample the rotational phase space by observing and recording the orientation of C_{60} molecules within an equilibrium MD simulation at a temperature of 300 K.

5.3 Thermal conductivity calculation

Direct heat non-equilibrium MD (Sec. 2.2.3) is used to predict the thermal conductivity of full degree of freedom and point mass systems.

In the full degree of freedom simulations, a 2×2 unit cell (826.0 \AA^2) cross-sectional area is used. The fixed and reservoir regions are 2 unit cells (28.74 \AA) in length, while the sample length varies from 5 to 35 unit cells (65.1 to 489 \AA). The simulation time step is 0.3 femtoseconds and the applied heat flux is $0.0035 \text{ Kcal/mol-fs}$. Velocity rescaling,

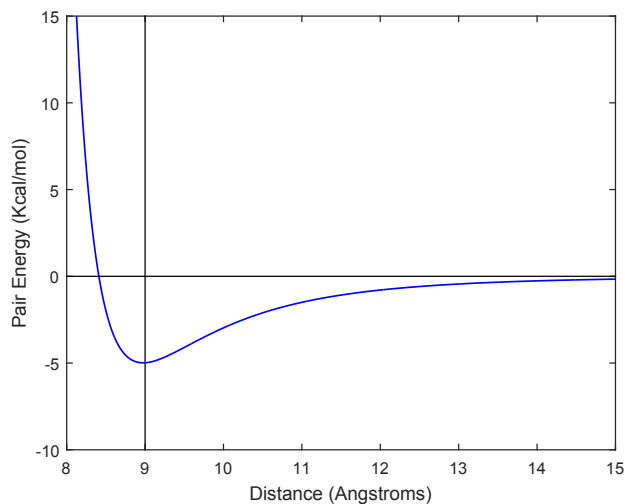


Figure 5.2: The effective molecular pair potential $U_{\text{Eff}}(r)$ used in point mass simulations. The vertical line crosses the minimum of the potential, which occurs at a pair separation of 9 Å.

Nose-Hoover thermostatting, and relaxation are run for 100,000 time steps each. The heat flux is applied for 1×10^7 time steps prior to a 3×10^6 time step data collection sequence. A diagram of the direct method simulation cell and an example output temperature profile are plotted in Fig. 5.3.

In the point mass simulations, the time step is 1.0 femtoseconds, the reservoirs are 4 unit cells in length, and all other parameters are identical to the full degree of freedom simulations. The lattice constant is changed to 12.68 Å from the 14.387 Å used in the full degree of freedom case in order to produce a zero pressure system at a temperature of 300 K. A 2×2 unit cell cross-sectional area is used for comparability to the full degree of freedom simulations.

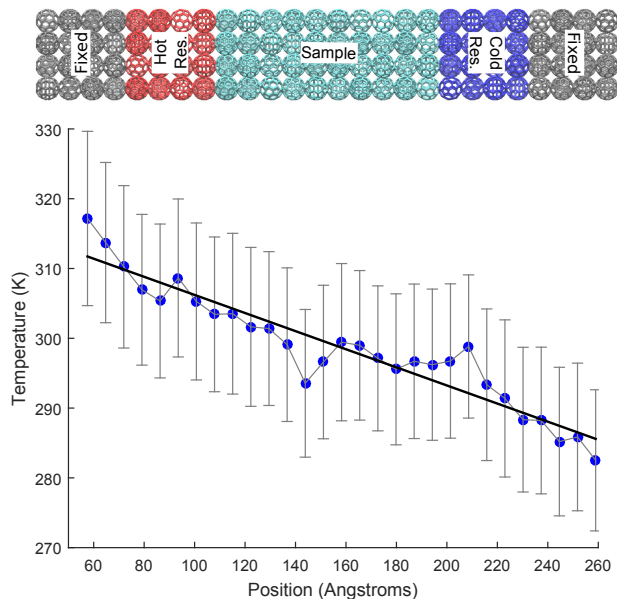


Figure 5.3: A diagram of a full degree of freedom C_{60} direct method MD simulation cell along with the temperature profile for a 15 unit cell (216 nm) long sample. Note that the rotational orientations of the C_{60} are random. Each data point represents the temperature of a layer of C_{60} molecules. The error bars represent the standard deviation of the kinetic energy within a layer (see Sec. 2.2.2).

5.4 Results

5.4.1 Validation

We validate our model of C_{60} by first comparing the vibrational characteristics of single molecule C_{60} to that of first principals density functional theory (DFT) [120] and to that of experiment [121]. The results are plotted in Fig. 5.4.

As shown in Fig 5.4(a), the PCFF model overestimates the single molecule heat capacity of the more accurate DFT model in the temperature range of 100 to 2000 K. At 300 K, the PCFF heat capacity is 36% greater than that of both DFT and experiment. The origin of the overestimation can be determined by comparing the molecular vibrational spectra produced using PCFF and using DFT [Fig 5.4(b)]. The PCFF model has a great number of modes at frequencies between 200 and 400 cm^{-1} that are not present in the DFT

model. Instead, the DFT model shows a peak in mode number near 800 cm^{-1} , as well as modes near 1600 cm^{-1} that are not present in the PCFF model. PCFF shifts modes that would otherwise be at higher frequency to lower frequencies, causing the heat capacity to accumulate faster at low temperature.

Despite the PCFF's inability to reproduce the DFT C_{60} vibrational spectrum, it correctly models the range of frequencies over which the molecular vibrations occur. This can be observed by comparing the high-temperature heat capacities of PCFF versus DFT C_{60} , which differ by less than a percent at 2000 K.

We validate the ability of our PCFF model to model crystalline C_{60} by comparing the frequency spectrum of the center of mass translations in an energy-conserving, full degree of freedom MD simulation of FCC arranged C_{60} to that of a frozen phonon model produced by Chen *et al.* (also using PCFF). The results are plotted in Fig. 5.5.

The three vibrational peaks at 20, 30 and 38 cm^{-1} in Fig. 5.5 agree well with the average frequencies of the three acoustic branches of the phonon dispersion. While comparison against another PCFF model cannot inform us regarding the accuracy of the PCFF model, the agreement between MD simulation and the frozen phonon model suggests that the phonon picture is an appropriate model for the center-of-mass translations in FCC C_{60} crystal.

5.4.2 Thermal conductivity

The length-dependent thermal conductivity of full degree of freedom and center-of-mass translation only FCC C_{60} are plotted in Fig. 5.6. Results of direct method MD simulation are compared to results using the Green-Kubo method [78] for the same system.

In the full degree of freedom system, the thermal conductivity as predicted from direct method appears to plateau to 0.28 W/m-K at a sample length of 28 nm before diverging

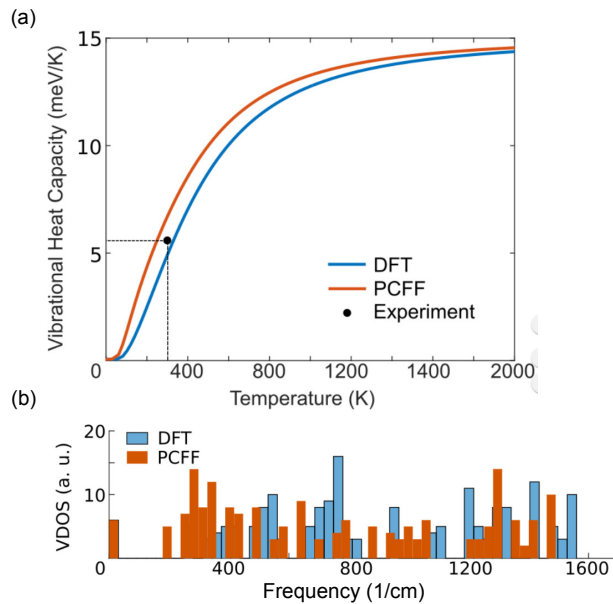


Figure 5.4: The (a) heat capacity and (b) spectrum of molecular vibrations of a single C_{60} molecule from the PCFF model compared to that using first principals density functional theory. Note that the experimental value was measured by Jin *et al.* [121] from crystalline C_{60} and has been normalized to a single crystal.

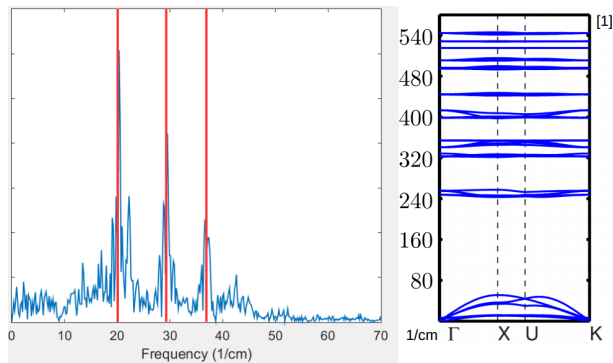


Figure 5.5: The frequency spectrum of center of mass translations in FCC C_{60} using the PCFF compared against the frozen phonon dispersion by Jin *et al.*, also produced from PCFF. The three peaks highlighted in red correspond with the average frequencies of the three acoustic branches.

linearly for samples 30 nm and longer. The Green-Kubo [78] thermal conductivity of 0.25 W/m-K agrees well both the plateau and with simulations results reported by Chen *et al.* [118]. We suspect that the linear divergence seen in the direct method results is a numerical artifact. Such divergence is well known for direct method MD simulations and

has been demonstrated by Hu *et al.* [79] to systematically occur in isotropic crystalline samples with length to cross-sectional area ratios (aspect ratios) greater than 100. While the aspect ratio of the samples considered here peak at only 12, it is unclear how the disorder introduced by the free rotations affects the divergence. In order to investigate the nature of the divergence further, it is necessary to determine whether the direct heat thermal conductivity at lower aspect ratios agrees with the plateau value by considering a 28 nm sample with 3×3 cross-sectional area.

In the center-of-mass translation only system, the direct method simulations converges at a sample length of 30 nm. The thermal conductivity of the 50 nm system is 0.36 W/m-K. The Green-Kubo thermal conductivity of the center-of-mass translation system is 0.45 W/m-K, 25% larger than the direct method prediction.

If the direct method thermal conductivity near a sample length of 25 nm is assumed to be the length-converged thermal conductivity of full degree of freedom FCC C_{60} , then both direct method and Green-Kubo simulations suggest that a system with only center-of-mass translations has a higher thermal conductivity (30% greater in direct method, 80% greater in Green-Kubo) than a full degree of freedom system. This behavior is counter-intuitive from a degree of freedom perspective, as less degrees of freedom are available to carry heat in the translation only system. However, the results suggest that the intra-molecular vibrations and molecular rotations present in the full degree of freedom system, but absent in the translation-only system, act as scattering sources of the center of mass phonons, inhibiting their transport and lowering thermal conductivity.

5.5 Conclusions

In this Chapter, we presented evidence that the motions of the centers of mass in an FCC C_{60} crystal may be treated as phonon-like. We also discovered that the thermal

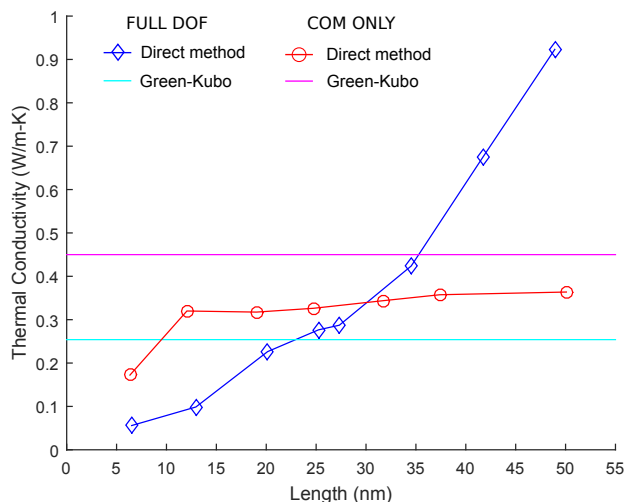


Figure 5.6: Thermal conductivity of full degree of freedom and center-of-mass translation only C_{60} systems at a temperature of 300 K.

conductivity of a full degree of freedom C_{60} crystal is lower than that of a system that considers only the motions of the molecular centers of mass. This behavior suggests a physical description of thermal transport whereby the center of mass phonons are scattering with molecular vibrations and rotations. An argument can be made that the large gap in frequency between the center of mass acoustic phonons and the intracage vibrations make any interaction between the two unlikely. Such an argument, however, does not sufficiently capture the role of rotations, both in their direct interaction with the center of mass phonons and in their role of possibly mediating interaction between center of mass phonons and molecular vibrations. Since the rotations are not limited in amplitude, they cannot be properly described in a phonon picture.

We have also revealed that the direct method prediction of thermal conductivity in full degree of freedom C_{60} crystal diverges for aspect ratios as low as 12. To better characterize the divergence, it is necessary to performed direct method MD simulations at lower aspect ratios using a 3×3 unit cell cross-sectional area.

Summary and future work

6.1 Overview

6.1.1 Summary

The aim of this thesis was to investigate thermal transport across two- and three-dimensional heterostructure junctions joining bulk crystals and in molecular crystals. In Chapter 2 we presented theoretical and practical underpinnings of two methods: direct heat MD simulation and HLD with the SBM. MD simulations allow us to integrate the coupled, non-linear equations of the classical many-body problem, while the direct method is a “computational experiment,” whereby thermal conductivity and thermal conductance can be extracted from the temperature profiles that result from the MD simulation. Though MD is powerful, it is inhibited by its inability to account for quantum effects. Within the scope of this thesis, the most pertinent facet of this limitation is the inability of MD to account for quantum statistics, specifically, the Bose-Einstein population distribution of phonons at thermal equilibrium. For soft systems that are at or near their Debye temperatures, this limitation does not present a problem. However, for stiff systems (like graphene) near room temperature, results from MD simulations can not be directly compared with results from experiment. HLD with the SBM overcomes this shortcoming of MD by naturally accounting for quantum statistics. The SBM is also inherently mode-level, allowing us to sweep over the first Brillouin zones of crystals and compute the transmission coefficients associated with every phonon mode. Integration then allows computation of thermal conductance using the Landauer formalism. The SBM, however, cannot account for the full

anharmonicity of the interatomic interactions in the way that MD simulations can, and hence the thermal conductance predicted from the SBM and the Landauer formalism will deviate in soft systems. It is appropriate to consider MD simulation as representative of the high-temperature limit of a system, and HLD with the SBM as representative of the harmonic, low-temperature limit.

In Chapter 3, we applied MD simulations and the SBM to a soft, three-dimensional semiconductor heterostructure junction, the Lennard-Jones superlattice joining crystalline leads. Using classical statistics, we identified a lead effect in the SBM, where nearly identical junctions have a higher thermal conductance when placed between leads of the same mass as opposed to being placed between leads of differing masses. This phenomenon results from the lack of anharmonic scattering occurring within the junction due to the assumptions of the SBM, causing the phonon properties of the leads to play a more important role in determining the junction thermal conductance. When the same systems are simulated using MD, we find that the lead effect is reversed, that is, a higher thermal conductance is observed when the junction is placed between leads of differing masses. The lead effect disappears in MD when higher temperatures, long superlattice periods, and rough interfaces are introduced. In smooth, short period systems at low temperatures, a lead effect transition takes place as we move from the SBM to MD, that is, as more and more anharmonicity is added.

In Chapter 4, we applied the SBM with quantum statistics to heterostructure junctions of graphene and hBN, exploiting the SBM's ability to more accurately represent graphitic systems at room temperature. We validated our method by demonstrating that our predictions for the thermal conductance of armchair- and zig-zag aligned graphene-hBN interfaces are in good agreement with literature. By applying the SBM across a uniform wavevector grid, we are able to plot the contributions to the thermal conductance as a

two-dimensional function of wavevector. Modes close to the center of the zone, which are both highly populated and have high group velocities, make the most significant contributions to thermal conductance. In graphene/hBN superlattice junctions, the lead effect discovered in the LJ superlattice system appears as well. Due to wavevector mapping of the thermal conductance contributions, we are able to isolate the cause of the lead effect in the graphene/hBN system to transmission at frequencies in the band gap of hBN that cannot occur if hBN is a lead. In bilayer systems, we discovered that, due to weak inter-layer coupling, the reduction in thermal conductance when moving from single to double layer reduces 10% on a per-area basis, which is insignificant when compared to the drastic reduction in thermal conductivity when moving from single to double layer graphene.

In Chapter 5, we used MD simulations' ability to model non-crystalline systems to study C_{60} molecular crystals at a temperature of 300 K. We formulated a model of C_{60} using PCFF, a potential that encompasses both covalent bonds and van der Waals interactions. We found that the molecular vibrational spectrum is similar in order of magnitude to results from first principles density functional theory calculations. When placed in a face-centered cubic crystal, the translations of the centers-of-mass of the C_{60} s show frequency peaks that agree with literature values using a frozen phonon approach. C_{60} at room temperature is interesting from a thermal transport perspective because while the centers-of-mass form a crystal, the molecules themselves rotate freely. By inhibiting first intramolecular vibrations and then both intramolecular vibrations and molecular rotations, we observe the effects of the different degrees of freedom as well as their interactions with one another.

6.1.2 Molecular dynamics versus scattering boundary method

It is important to summarize the situations where direct heat MD simulations (see Sec. 2.2.3) are most appropriate and the situations where Landauer formalism and the SBM (see

Sec. 2.4) are most appropriate.

Direct heat MD simulations are most appropriate for modeling systems at temperatures higher than their Debye temperature. In the high-temperature limit, the classical statistics present in the MD system do not differ drastically from quantum statistics. Further, the ability of MD simulations to capture anharmonic dynamics is critical in this limit as anharmonic dynamics are more significant at high temperature. Special care must be taken when using MD simulations at temperatures very low relative to the system's Debye temperature. First, the lack of quantum statistics presents an additional source of error if the aim is to compare results from MD to results from experiments. Second, as phonon mean free paths become longer at low temperature, the system lengths necessary for there to be a detectable temperature gradient can become very large, requiring very long computation time for convergence. In the limit of zero temperature, or in a MD simulation with only harmonic interactions, no phonons originating from the reservoirs interact with one another in the sample to thermalize, and hence there exists no near-equilibrium temperatures within the sample to record a temperature profile. In this ballistic limit, it is still possible to extract average kinetic energies within the sample, but these average kinetic energies cannot be directly converted to a temperature as they associated with distribution functions that are far out of equilibrium.

The Landauer formalism in conjunction with SBM is most appropriate for modeling systems at temperatures far below their Debye temperature. As formulated in this thesis, the SBM does not account for anharmonic interactions at all but does account for the quantum Bose-Einstein distribution of phonons, making it ideal for the low temperature regime. The notion of temperature within SBM pertains only to the distribution functions, and not to the level of anharmonic interactions. Even if a distribution function for a high temperature is used, the thermal conductance predicted from SBM is only a harmonic

value. It cannot be said in generality whether a harmonic thermal conductance is higher or lower than a fully anharmonic thermal conductance as it will depend on the specific material system. Another important limitation of the Landauer formalism as written in Sec. 2.4.1 is that the formulation is based on the assumption of an infinitesimal heat flow across the junction. While the thermal conductance predicted from infinitesimal heat flow is typically valid in the linear regime (i.e., the Fourier regime where heat varies directly with temperature difference), the SBM cannot be used to predicted thermal conductance in the presence of large heat or temperature gradients. The method suggested in Sec. 6.2.1 should instead be considered.

6.2 Future work

6.2.1 Coupled leads

As discussed in Sec. 2.3.3, anharmonic lattice dynamics can be used to predict the thermal conductivity of crystals at finite temperature. First, phonon-phonon scattering rates are accounted for by treating the anharmonic interatomic interactions perturbatively. The Boltzmann transport equation associated with the non-equilibrium phonon population is then solved (either directly or iteratively) using the phonon-phonon scattering rates as input.

In the form presented in Sec. 2.1, the Landauer formalism assumes that the left and right leads are nearly in thermal equilibrium. That is, the temperature of the leads differ only by an infinitesimal amount, and similarly, the heat that flows between the leads through the junction is infinitesimal. In realistic situations, finite heat flows between the leads and the leads are not at thermal equilibrium. This inconsistency presents a major limitation of the HLD and SBM formalism as presented and used in this thesis. An alternate scheme can

be used whereby the leads L and R are explicitly modeled using two separate Boltzmann transport equations. The junction can then be introduced as a coupling term between the two equations. The Boltzmann transport equations are

$$\mathbf{v}_{\mathbf{g},\text{L}}(\mathbf{k}, \nu)^\dagger \nabla_{\mathbf{x}} n_{\text{L}}(\mathbf{k}, \nu) = \left[\frac{\partial n_{\text{L}}(\mathbf{k}, \nu)}{\partial t} \right]_{\text{L} \leftrightarrow \text{L}} + \left[\frac{\partial n_{\text{L}}(\mathbf{k}, \nu)}{\partial t} \right]_{\text{L} \leftrightarrow \text{R}}, \quad (6.1)$$

$$\mathbf{v}_{\mathbf{g},\text{R}}(\mathbf{k}, \nu)^\dagger \nabla_{\mathbf{x}} n_{\text{R}}(\mathbf{k}, \nu) = \left[\frac{\partial n_{\text{R}}(\mathbf{k}, \nu)}{\partial t} \right]_{\text{R} \leftrightarrow \text{R}} + \left[\frac{\partial n_{\text{R}}(\mathbf{k}, \nu)}{\partial t} \right]_{\text{R} \leftrightarrow \text{L}}. \quad (6.2)$$

In Eqs. 6.1 and 6.2, x is the cross-junction direction, n is the wavevector-domain phonon distribution function, and subscripts L and R refer to the two leads. The first terms of the right-hand sides include all scattering events occurring within a given lead, including but not limited to phonon-phonon scattering, boundary scattering, and impurity scattering. The second terms of the right-hand sides are the cross-junction terms and account for the loss and gain of phonons across the junction, that is, the cumulative effect of transmission and reflection events. If the SBM is used to compute phonon transmission coefficients $\alpha(\mathbf{k}, \nu)$, then, using a probabilistic interpretation of transmission coefficient, a possible form of the cross-junction term might be

$$\left[\frac{\partial n_{\text{L}}(\mathbf{k}, \nu)}{\partial t} \right]_{\text{L} \leftrightarrow \text{R}} \propto \alpha_{\text{L} \rightarrow \text{R}}(\mathbf{k}, \nu) n_{\text{L}}(\mathbf{k}, \nu) v_{\mathbf{g},\text{L}}^x(\mathbf{k}, \nu) + \sum_{\mathbf{k}', \nu'}^{\text{R}} \alpha'_{\text{R} \rightarrow \text{L}}(\mathbf{k}', \nu', \mathbf{k}, \nu) n_{\text{R}}(\mathbf{k}', \nu') v_{\mathbf{g},\text{R}}^x(\mathbf{k}', \nu'), \quad (6.3)$$

along with a prefactor that has a unit of inverse length. Eq. 6.3 models the cross-junction term as the modal phonon fluxes in the x -direction mediated by transmission coefficients. The first term on the right-hand side represents the outgoing flux of phonon mode (\mathbf{k}, ν) . The second term on the right-hand side represents the incoming flux into phonon mode (\mathbf{k}, ν) from all R phonon modes (\mathbf{k}', ν') . Note that α' on the right hand side differs from α as α' describes the specific transmission coefficient from one R mode to a single L mode, as opposed to one R mode to all L modes.

An inconsistency that arises if Eq. 6.3 is used with Eqs. 6.1 and 6.2 is that, while the collision terms within the leads account for anharmonic effects perturbatively, the SBM does not account for any anharmonic effects. While use of the SBM with this model allows us to model harmonic junctions between anharmonic, out-of-equilibrium leads, the calculation of the cross-junction coupling with anharmonicity, perturbatively or otherwise, remains a challenge.

6.2.2 C_{60} intercage thermal conductance

In Chapter 5, we proposed the notion that center of mass phonons were interacting with cage vibrations and rotations, reducing thermal conductivity. In this picture, collective waves carry energy through bulk C_{60} , scattering from time to time. An alternate picture is that energy diffuses from molecule to molecule, where energy is trapped in the high-frequency vibrations of the cage (in a classical picture) but is slowly drained by the weak cross-cage interaction. In the limit of harmonic interactions, the timescales involved with the cross-cage interaction can be computed on the basis of the vibration modes of the single C_{60} molecule, and, in conjunction with the Landauer formalism, can be used to predict the thermal conductance between C_{60} cages. In the case of two neighboring cages, we can compute the vibrational spectrum and normal modes of the isolated cage as well the as vibrational spectrum and normal modes of the two cage system, the latter of which takes into account the harmonic intercage interaction. It is then possible to establish a system where a single molecular mode is active in one cage and no other modes are present. We can then calculate the lifetime of that mode in the presence of a neighboring cage. We can also calculate the exact rate at which energy leaves the initial mode to the other modes of the system. By establishing a list of mode-to-mode energy transfer rates, it is possible to use a Landauer-like formalism to calculate the harmonic intercage thermal conductance.

See Appendix [A](#) for further discussion on this method.

Intermolecular interactions by mode projection

A.1 Theory

Suppose we have a system of atoms F that interact via Hooke's law springs and are governed by classical physics. F can be divided into two disjoint sets of atoms A and B , representing two molecules that share no degrees of freedom. F has a total of N degrees of freedom, N_A of them in A and N_B of them in B , such that $N = N_A + N_B$. We think about how energy moves between A and B in terms of their vibrations. This will allow us to describe the thermal conductance between individual molecules.

F is described by a configuration vector $\mathbf{x}(t)$ that varies with time t . \mathbf{x} lives in an N -dimensional space \mathcal{F} . If interaction operator is \mathbf{H} (that is, \mathbf{H} describes all interactions in F), then the time evolution of $\mathbf{x}(t)$ is given by Newton's laws

$$\frac{d^2\mathbf{x}}{dt^2} = \mathbf{H}\mathbf{x}. \tag{A.1}$$

We will assume \mathbf{H} is time-independent. The analysis is analogous for time-variant \mathbf{H} , however the results are more involved practically and beyond the scope of this report. The crux of the technique to be described is to represent the motion of F using the vibrational modes of A and B in isolation. Conceptually, this is no different than choosing to use a different coordinate system to describe some situation. Practically, it is only slightly more involved.

Due to disjointness, \mathbf{x} can be split between A and B without any complication: $\mathbf{x} = (\mathbf{x}_A, \mathbf{x}_B)$, where the operation (\cdot, \cdot) indicates the concatenation of two vectors. \mathbf{x}_A describes A alone, and lives in an N_A -dimensional subspace \mathcal{A} . Similarly, \mathbf{x}_B describes B alone and lives in an N_B -dimensional subspace \mathcal{B} . It is convenient to define \mathbf{H}_A as the interaction operator containing only interactions internal to A . Similarly, \mathbf{H}_B contains only interactions internal to B . Then, in the basis upon which interactions are described,

$$\mathbf{H} = \begin{bmatrix} \mathbf{H}_A & 0 \\ 0 & \mathbf{H}_B \end{bmatrix} + \delta\mathbf{H} = \mathbf{H}_0 + \delta\mathbf{H}, \quad (\text{A.2})$$

where $\delta\mathbf{H}$ describes intermolecular interactions.

Suppose $\{\mathbf{a}_1, \dots, \mathbf{a}_{N_A}\} \in \mathcal{A}$ forms a basis for \mathcal{A} and $\{\mathbf{b}_1, \dots, \mathbf{b}_{N_B}\} \in \mathcal{B}$ forms a basis for \mathcal{B} . Then certainly $\{(\mathbf{a}_1, \mathbf{0}_B), \dots, (\mathbf{a}_{N_A}, \mathbf{0}_B), (\mathbf{0}_A, \mathbf{b}_1), \dots, (\mathbf{0}_A, \mathbf{b}_{N_B})\} \in \mathcal{F}$, or $\{\mathbf{a}_n\} \cup \{\mathbf{b}_m\}$ for short, forms a basis for \mathcal{F} . A possible basis for \mathcal{A} is set of eigenvectors of \mathbf{H}_A , so let $\{\mathbf{a}_n\}$ be the eigenvectors of \mathbf{H}_A (i.e., the natural modes of A). Similarly, the eigenvectors of \mathbf{H}_B form a basis for \mathcal{B} , so let $\{\mathbf{b}_m\}$ be the eigenvectors of \mathbf{H}_B (i.e., the natural modes of B). For compactness, we will refer to $\{\mathbf{a}_n\} \cup \{\mathbf{b}_m\}$ as $\{\mathbf{e}_p^0\}$, where the first N_A eigenvectors are those of \mathbf{H}_A , and the remaining N_B are those of \mathbf{H}_B . Since $\{\mathbf{e}_p^0\}$ is a basis for \mathcal{F} , any configuration of the system can be written as the superposition

$$\mathbf{x}(t) = \sum_p^N c_p(t) \mathbf{e}_p^0 \exp(-i\omega_p^0 t), \quad (\text{A.3})$$

where ω_p^0 is the natural frequency associated with basis element \mathbf{e}_p^0 . These frequencies can be obtained by solving the eigenproblem for \mathbf{H}_A or \mathbf{H}_B . The components $\{c_p(t)\}$ are, in general, time-dependent. This is because $\{\mathbf{e}_p^0\}$ are generally not eigenvectors of \mathbf{H} . As a result, despite the explicit time dependence $\exp(-i\omega_p^0 t)$ in every term in the sum, no term is of single frequency. In quantum mechanical parlance, these modes are not “stationary.”

We are interested in finding the components $\{c_p(t)\}$ as their squares will tell us about the energy in modes of A and modes of B as a function of time. Substitution of Eq. A.3 into Eq. A.1 results in

$$\sum_p^N \left(\frac{d^2 c_p}{dt^2} - i2\omega_p^0 \frac{dc_p}{dt} \right) \mathbf{e}_p^0 \exp(-i\omega_p^0 t) = \sum_p^N c_p \delta \mathbf{H} \mathbf{e}_p^0 \exp(-i\omega_p^0 t). \quad (\text{A.4})$$

Keeping in mind the orthonormality condition $\mathbf{e}_q^{0\dagger} \mathbf{e}_p^0 = \delta_{pq}$, projection of Eq. A.4 onto modes \mathbf{e}_q^0 from the left results in

$$\frac{d^2 c_q}{dt^2} - i2\omega_q^0 \frac{dc_q}{dt} = \sum_p^N c_p (\mathbf{e}_q^{0\dagger} \delta \mathbf{H} \mathbf{e}_p^0) \exp(-i\omega_p^0 t). \quad (\text{A.5})$$

Speaking in the language of anharmonic lattice dynamics, the term $\mathbf{e}_q^{0\dagger} \delta \mathbf{H} \mathbf{e}_p^0$ is the p - q matrix element of the perturbation $\delta \mathbf{H}$ in the unperturbed eigenbasis $\{\mathbf{e}_p^0\}$. If we isolate c_q on the left hand side, we get

$$\frac{d^2 c_q}{dt^2} - i2\omega_q^0 \frac{dc_q}{dt} - [(\mathbf{e}_q^{0\dagger} \delta \mathbf{H} \mathbf{e}_q^0) \exp(-i\omega_q^0 t)] c_q = \sum_{p \neq q}^N c_p (\mathbf{e}_q^{0\dagger} \delta \mathbf{H} \mathbf{e}_p^0) \exp(-i\omega_p^0 t). \quad (\text{A.6})$$

This is a set of N coupled second order complex linear differential equations for the mode amplitudes $c_q(t)$. Note that the strength of coupling depends on the matrix elements of the intermolecular interaction $\delta \mathbf{H}$. Since these equations are linear, they can be solved to extract squared amplitudes $|c_q(t)|^2$, which are directly proportional to the energy in mode \mathbf{e}_q^0 at time t .

While Eq. A.6 is general, its solution may be involved. By limiting ourselves to harmonic interactions, we exploit the N eigenvectors $\{\mathbf{e}_m\}$ of \mathbf{H} and their associated frequencies

$\{\omega_m\}$ to avoid solving Eq. A.6 directly. We decompose Eq. A.3 as

$$\mathbf{x}(t) = \sum_p^N c_p(t) \mathbf{e}_p^0 \exp(-i\omega_p^0 t) = \sum_m^N b_m \mathbf{e}_m \exp(-i\omega_m t), \quad (\text{A.7})$$

where in this case the coefficients b_m are determined by the initial conditions and do not vary in time

$$b_m = \sum_p^N c_p(0) \mathbf{e}_m^\dagger \mathbf{e}_p^0. \quad (\text{A.8})$$

Taking the inner product of Eq. A.7 with \mathbf{e}_q^0 gives

$$c_q(t) = \sum_m^N \left[\left(\sum_p^N c_p(0) \mathbf{e}_m^\dagger \mathbf{e}_p^0 \right) \mathbf{e}_q^{0\dagger} \mathbf{e}_m \exp[i(\omega_q^0 - \omega_m)t] \right], \quad (\text{A.9})$$

where we have substituted Eq. A.8 for b_m .

Once we have the amplitudes $c_q(t)$ we can consider their energy content $|c_q(t)|^2$ under a set of initial conditions where some A mode $\mathbf{e}_p^0 \in \mathcal{A}$ has unit amplitude at $t = 0$ and no other mode is activated. We can then observe the amplitudes in all of the B modes and the rates of change of their energies. These energies, of course, come from the initially excited A mode. From this we can build a matrix of energy transfer timescales \mathbf{T}_{pq} , paving the way to thermal conductance prediction.

A.2 Toy example

While the following example may appear too simple to be useful, it serves to drive home two points. First, despite the apparent complication that comes with generalization, this method is no different from plucking an atom and seeing how another atom starts to move in response. Second, this method can be used to study energy transfer between any arbitrary subset of a F with any other arbitrary subset of F , as long as these subsets do

not share degrees of freedom. These subsets can be individual atoms, or even individual degrees of freedom within an atom.

Suppose two atoms of unit mass are attached to walls with springs of unit stiffness. These are our “molecules.” They interact via a spring of stiffness k . We have $N = 2$, $N_A = 1$, $N_B = 1$. In the basis of the atomic positions, we have

$$\mathbf{H}_A = \mathbf{H}_B = -1, \quad \mathbf{H} = \begin{bmatrix} -1 - k & k \\ k & -1 - k \end{bmatrix}, \quad (\text{A.10})$$

with

$$\{\mathbf{e}_1^0, \mathbf{e}_2^0\}, \{\omega_1^0, \omega_2^0\} = \left\{ \begin{bmatrix} 1 \\ 0 \end{bmatrix}, \begin{bmatrix} 0 \\ 1 \end{bmatrix} \right\}, \{1, 1\}, \quad (\text{A.11})$$

and

$$\{\mathbf{e}_1, \mathbf{e}_2\}, \{\omega_1, \omega_2\} = \left\{ \begin{bmatrix} 1 \\ 1 \end{bmatrix}, \begin{bmatrix} -1 \\ 1 \end{bmatrix} \right\}, \{-1, -2k - 1\}. \quad (\text{A.12})$$

We want to see how energy flows from left side mode \mathbf{e}_1^0 to right side mode \mathbf{e}_2^0 . This is just a general way of saying we would like to see how energy flows to the second atom when the first atom is plucked. The appropriate initial condition is $c_1(0) = 1$ and $c_2(0) = 0$. First, solve for $\{b_m\}$

$$b_1 = \mathbf{e}_1^\dagger \mathbf{e}_1^0 = \begin{bmatrix} 1 & 1 \end{bmatrix} \begin{bmatrix} 1 \\ 0 \end{bmatrix} = 1 \quad (\text{A.13})$$

$$b_2 = \mathbf{e}_2^\dagger \mathbf{e}_1^0 = \begin{bmatrix} -1 & 1 \end{bmatrix} \begin{bmatrix} 1 \\ 0 \end{bmatrix} = -1. \quad (\text{A.14})$$

Next, solve for the amplitude of \mathbf{e}_2^0 , $c_2(t)$

$$c_2(t) = b_1 \mathbf{e}_2^{0\dagger} \mathbf{e}_1 \exp [i(\omega_2^0 - \omega_1)t] + b_2 \mathbf{e}_2^{0\dagger} \mathbf{e}_2 \exp [i(\omega_2^0 - \omega_2)t] \quad (\text{A.15})$$

$$= \begin{bmatrix} 0 & 1 \end{bmatrix} \begin{bmatrix} 1 \\ 1 \end{bmatrix} \exp [i2t] - \begin{bmatrix} 0 & 1 \end{bmatrix} \begin{bmatrix} -1 \\ 1 \end{bmatrix} \exp [i2(k+1)t] \quad (\text{A.16})$$

$$= \exp [i2t] - \exp [i2(k+1)t] . \quad (\text{A.17})$$

Finally, consider the square amplitude, a real number proportional to mode energy

$$|c_2(t)|^2 = [\sin (2t) - \sin [2(k+1)t]]^2 + [\cos (2t) - \cos [2(k+1)t]]^2 \quad (\text{A.18})$$

$$= 4 \sin^2 (kt) . \quad (\text{A.19})$$

As expected, the energy moves back and forth between the left and right “molecules” with a frequency proportional to k , the interaction stiffness. How do we extract a timescale τ_{12} ? Here, the frequency is an obvious timescale, but in general there will not be a single frequency. We apply a trick similar to what is done in Fermi’s Golden Rule, which is

$$|c_2(t)|^2 = 4 \sin^2 (kt) \approx 4[\exp (2kt) - 1] . \quad (\text{A.20})$$

This will be true very close to $t = 0$, as $\sin (x)$ and $\exp (x)$ have the same linear term in their Taylor series expansion about $x = 0$. A central assumption of Fermi’s Golden Rule is that the amplitude varies slowly so that $c_n(t) \approx c_n(0)$. Going by this convention, we say

$$\tau_{12} = \frac{1}{2k} . \quad (\text{A.21})$$

As k goes to zero, the lifetime of \mathbf{e}_1^0 goes to infinity, as it does not lose energy to \mathbf{e}_2^0 . As k increases, the mode lifetime goes to zero. This agrees with intuition.

A.3 Towards thermal conductance

Both temperature and quantum population effects can be added to this model. Suppose that A is at temperature T_A , meaning some external influence holds the square amplitudes of mode \mathbf{e}_p^0 at $\hbar\omega_p^0 f_{\text{BE}}(T_A, \omega_p^0)$, where f_{BE} is Bose-Einstein distribution. To get to thermal conductance, consider the energy current balance between A and B

$$q = q_{A \rightarrow B} - q_{B \rightarrow A}. \quad (\text{A.22})$$

In Landauer thermal conductance for crystalline systems, $q_{A \rightarrow B}$ is

$$q_{A \rightarrow B} = \frac{1}{2\pi} \int d\boldsymbol{\kappa} \sum_{\nu}^+ \hbar\omega(\boldsymbol{\kappa}, \nu) v_z(\boldsymbol{\kappa}, \nu) \alpha(\boldsymbol{\kappa}, \nu) f_{\text{BE}}(\boldsymbol{\kappa}, \nu, T_A). \quad (\text{A.23})$$

In analogy, $q_{A \rightarrow B}$ should be

$$q_{A \rightarrow B} = \sum_n^{N_A} \hbar\omega_n^0 f_{\text{BE}}(\omega_n^0, T_A) \left[\sum_m^{N_B} \frac{1}{\mathbf{T}_{nm}} \right]. \quad (\text{A.24})$$

Note that $\sum_m^{N_B} 1/\mathbf{T}_{nm}$ has taken the role of $v_z(\boldsymbol{\kappa}, \nu) \alpha(\boldsymbol{\kappa}, \nu) d\boldsymbol{\kappa}$. The linear response relation $q = G\Delta T$ for thermal conductance G is only valid for ΔT small. For ΔT small enough to be well approximated by the linear term of the Taylor series for f_{BE} about T_A , thermal conductance can be written as

$$G = \sum_n^{N_A} \hbar\omega_n^0 \frac{\partial f_{\text{BE}}}{\partial T}(\omega_n^0, T_A) \left[\sum_m^{N_B} \frac{1}{\mathbf{T}_{nm}} \right]. \quad (\text{A.25})$$

Phonons as an operator equation

In Sec. 2.3, a derivation of the phonon modes for a three-dimensional periodic mass-spring model of a crystal was given using Newtonian classical mechanics. While the derivation is the easiest to conceptually understand, it is not usually how it is done in most texts on the subject. Instead, an operator-based derivation compatible with both Hamiltonian mechanics and quantum mechanics will be summarized in this Appendix for a one-dimensional system. Intuitive understanding of the one-dimensional case leads to intuitive understanding of the three-dimensional case, however, the algebra involved in the three-dimensional case is more involved. A textbook such as Ref. [36] can be referred to for the three-dimensional derivation.

The Hamiltonian for the one-dimensional chain is

$$H = \sum_n \sum_i \frac{\hat{p}_{ni}^2}{2m_i} + \sum_{n,l} \sum_{i,j} \Phi_{ni,lj} (\hat{x}_{ni} - \hat{x}_{lj})^2. \quad (\text{B.1})$$

n and l are indices over the unit cells, while i and j are indices over the atoms within a unit cell. m_i are the scalar atomic masses, while \hat{p}_{ni} and \hat{x}_{ni} are the atomic momentum and position operators. Suppose that the crystal has a unit cell length of a so that na is a lattice vector for any integer n . If we assume that there is only one atom per unit cell, that each atom interacts only with its immediate neighbors, and that all interactions are identical, Eq. B.1 can be simplified to

$$H = \sum_n \frac{\hat{p}_n^2}{2m} + \frac{m\omega_0^2}{2} (\hat{x}_{n-1} - \hat{x}_n)^2, \quad (\text{B.2})$$

where the atom index has been dropped and the force constant has been written in terms

of its natural frequency. Assume that \hat{x}_n and \hat{p}_n have Fourier decompositions

$$\hat{x}_n = \sum_k \hat{X}_k \exp(ikna) \quad (\text{B.3})$$

and

$$\hat{p}_n = \sum_k \hat{P}_k \exp(ikna), \quad (\text{B.4})$$

where k is the wavenumber. To the best of my understanding, Eqs. B.3 and B.4 ensure that operators \hat{x}_{ni} and \hat{p}_{ni} are invariant with respect to translation by a unit cell, that is, invariant in the change of index n . The exact theoretical origin is found in the spectral theory of self-adjoint operators and is beyond the scope of this thesis. Substitution of Eqs. B.3 and B.4 into Eq. B.2 gives

$$\begin{aligned} \text{H} = \sum_n \left[\sum_{k,q} \frac{\hat{P}_k \hat{P}_q \exp(i(k+q)na)}{2m} + \right. \\ \left. \frac{m\omega_0^2}{2} (\exp(-ika) - 1) \exp(-ikna) \hat{X}_k (\exp(-iqa) - 1) \exp(-iqna) \hat{X}_q \right]. \end{aligned} \quad (\text{B.5})$$

The second term requires expansion of the square Hooke's law term in the Hamiltonian. Using the orthonormality condition $\sum_n \exp[i(k+q)na] = \delta_{k,-q}$, the summation over the unit cell indices n can be performed to reveal

$$\text{H} = \sum_k \frac{\hat{P}_k \hat{P}_{-k}}{2m} + \frac{m\omega_0^2}{2} (\exp(-ika) - 1) (\exp(ika) - 1) \hat{X}_k \hat{X}_{-k}, \quad (\text{B.6})$$

which can be further simplified using trigonometric identities to

$$\text{H} = \sum_k \frac{\hat{P}_k \hat{P}_{-k}}{2m} + \frac{m\omega_0^2}{2} 4 \sin^2(ka/2) \hat{X}_k \hat{X}_{-k}. \quad (\text{B.7})$$

The transforms in Eq. B.3 and B.4 diagonalizes Eq. B.2 into Eq. B.5, the latter of which can

be thought of as a countably infinite matrix with only diagonal elements and where each diagonal element is indexed by a wavenumber k . It is important to notice the similarity of Eq. B.7 with the Hamiltonian for the simple harmonic oscillator, as this analogy carried forth will bring about the phonon modes.

Since Eq. B.7 is left as an operator equation, the procedure to derive the phonon modes completely can be done either classically or quantum mechanically. If done quantum mechanically, the procedure is to first show that \hat{X}_k and \hat{P}_k are canonically conjugate (i.e., a Heisenberg pair). Then, treating \hat{X}_k and \hat{P}_k as canonical position and momenta, an equivalent simple harmonic oscillator system is solved by defining ladder operators \hat{a}_k and \hat{a}_k^\dagger and rewriting Eq. B.7 in terms of the ladder operators. This derivation can be found in any standard text on quantum mechanics.

Bibliography

- [1] D. G. Cahill, P. V. Braun, G. Chen, D. R. Clarke, S. Fan, K. E. Goodson, P. Keblinski, W. P. King, G. D. Mahan, A. Majumdar, H. J. Maris, S. R. Phillpot, E. Pop, and L. Shi. *Appl. Phys. Rev.*, 1:793, 2014. [1](#)
- [2] D. G. Cahill, W. K. Ford, K. E. Goodson, G. D. Mahan, A. Majumdar, H. J. Maris, R. Merlin, and S. R. Phillpot. *J. Appl. Phys.*, 93:011305, 2003. [1](#)
- [3] E. T. Swartz and R. O. Pohl. *Rev. Mod. Phys.*, 61:605, 1989. [1](#), [40](#), [69](#), [81](#)
- [4] E. S. Landry and A. J. H. McGaughey. *Phys. Rev. B*, 80:165304, 2009. [1](#), [29](#), [30](#), [40](#), [41](#), [48](#), [63](#), [64](#), [69](#)
- [5] A. Y. Cho. *Appl. Phys. Lett.*, 19:467, 1971. [1](#), [3](#), [39](#)
- [6] L. Esake and L. L. Chang. *Phys. Rev. Lett.*, 31:2080, 1974. [1](#), [3](#), [39](#)
- [7] Z. Liu, L. Ma, G. Shi, W. Zhou, Y. Gong, and S. Lei. *Nature Nano.*, 8:119, 2013. [1](#), [61](#)
- [8] G. H. Han, J. A. Rodriguez-Manzo, C.-W. Lee, N. J. Kybert, M. B. Lerner, Z. J. Qi, E. N. Dattoli, A. M. Rappe, M. Drndic, and A. T. C. Johnson. *ACS Nano*, 7:10129, 2013. [1](#), [61](#)
- [9] R. C. Yu, N. Tea, M. B. Salamon, D. Lorents, and R. Malhotra. *Phys. Rev. Lett.*, 68:2050, 1992. [1](#), [4](#), [84](#)
- [10] T. L. Bergman, A. S. Lavinea, F. P. Incropera, and D. P. DeWitt. *Fundamentals of Heat and Mass Transfer*. Wiley, 2011. [2](#), [12](#)
- [11] G. Chen. *Nanoscale Energy Transport and Conversion: A Parallel Treatment of*

- Electrons, Molecules, Phonons, and Photons*. Oxford University Press, 2005. 2, 27, 28
- [12] A. K. Geim and K. S. Novoselov. *Nat. Mater.*, 6:183, 2007. 3
- [13] D. S. L. Abergel, V. Apalkov, J. Berashevich, K. Ziegler, and T. Chakraborty. *Adv. Phys.*, 59:261, 2010. 3
- [14] Z. Liu, L. Ma, G. Shi, W. Zhou, Y. Gong, S. Lei, X. Yang, J. Zhang, J. Yu, K. P. Hackenberg, A. Babakhani, J.-C. Idrobo, R. Vajtai, J. Lou, and P. M. Ajayan. *Nat. Nanotechnol.*, 8:119, 2013. 3
- [15] J. Lu, L. C. Gomes, R. W. Nunes, A. H. Castro Neto, and K. P. Loh. *Nano Lett.*, 14:5133, 2014. 3
- [16] N. H. Tea, R.-C. Yu, M. B. Salamon, D. C. Lorents, R. Malhotra, and R. S. Ruoff. *Appl. Phys. A*, 56:219, 1993. 4, 84
- [17] M. P. Allen and D. J. Tildesley. *Computer Simulation of Liquids*. Clarendon Press, 1989. 4, 10
- [18] M. T. Dove. *Introduction to Lattice Dynamics*. Cambridge University Press, 2005. 4, 23, 48
- [19] C. Kittel. *Introduction to Solid State Physics*. Wiley, 2004. 4, 5, 23
- [20] N. W. Ashcroft and N. D. Mermin. *Solid State Physics*. Cengage Learning, 1976. 4, 5, 7, 9, 23, 24, 25
- [21] J. E. Lennard-Jones. *Proc. R. Soc. London, Ser. A*, 106:463, 1924. 4, 8
- [22] J. Tersoff. *Phys. Rev. B*, 37:6991, 1988. 4, 8, 65
- [23] D. Sholl and J. A. Steckel. *Density Functional Theory: A Practical Introduction*. Wiley-Interscience, 2009. 4

- [24] W. Kohn and L. J. Sham. *Phys. Rev.*, 140:A1133, 1965. 4
- [25] P. K. Schelling, S. R. Phillpot, and P. Keblinski. *Phys. Rev. B*, 65:144306, 2002. 5, 13, 44
- [26] M. E. Lumpkin, W. M. Saslow, and W. M. Visscher. *Phys. Rev. B*, 17:4295, 1978. 5, 30, 40, 63, 64
- [27] J. Wang and J.-S. Wang. *J. Phys.: Condens. Matter*, 19:236211, 2007. 5, 30, 40, 48, 49, 63, 64
- [28] H. Zhao and J. B. Freund. *J. Appl. Phys.*, 97:024903, 2005. 5, 30, 31, 35, 40, 48, 49, 63, 64
- [29] H. Sun, S. J. Mumby, J. R. Maple, and A. T. Hagler. *J. Am. Chem. Soc.*, 116:2978, 1994. 8, 87
- [30] S. Plimpton. *J. Comp. Phys.*, 117:1, 1995. 9, 44, 87
- [31] N. Yang, G. Zhang, and B. Li. *Nano Lett.*, 8:276, 2008. 13, 39
- [32] F. Reif. *Fundamentals of Statistical and Thermal Physics*. Waveland Press, 2008. 13, 27
- [33] D. J. Evans and B. L. Holian. *J. Chem. Phys.*, 83:4069, 1985. 14
- [34] Eigen C++ library. http://eigen.tuxfamily.org/index.php?title=Main_Page. 22
- [35] ScaLAPACK library. <http://www.netlib.org/scalapack/>. 22
- [36] A. L. Fetter and J. D. Walecka. *Quantum Theory of Many-Particle Systems*. Dover Publications, 2003. 24, 113
- [37] R. D. Mattuck. *A Guide to Feynman Diagrams in the Many-Body Problem*. Dover Publications, 1992. 24

- [38] C. Cohen-Tannoudji, J. Dupont-Roc, and G. Grynberg. *Photons and Atoms: Introduction to Quantum Electrodynamics*. Wiley-VCH, 1997. 25
- [39] J. E. Turney, E. S. Landry, A. J. H. McGaughey, and C. H. Amon. *Phys. Rev. B*, 79:064301, 2009. 26
- [40] L. Lindsay, D. A. Broido, and T. L. Reinecke. *Phys. Rev. B*, 88:144306, 2013. 26
- [41] A. Jain and A. J. H. McGaughey. *J. Appl. Phys.*, 116:073503, 2014. 26
- [42] J. A. Reissland. *Physics of Phonons*. John Wiley & Sons Ltd, 1973. 26
- [43] G. P. Srivastava. *The Physics of Phonons*. CRC Press, 1990. 26
- [44] J. M. Ziman. *Electrons and Phonons: The Theory of Transport Phenomena in Solids*. Oxford University Press, 2001. 26
- [45] R. Landauer. *Philos. Mag.*, 21:863, 1970. 28, 48, 64
- [46] S. Datta. *Quantum Transport: Atom to Transistor*. Cambridge University Press, 2005. 28
- [47] D. A. Young and H. J. Maris. *Phys. Rev. B*, 40:3685, 1989. 30, 40, 48, 63, 64
- [48] S. Lu and A. J. H. McGaughey. *AIP Advances*, 5:053205, 2015. 30, 76
- [49] J.-S. Wang, J. Wang, and J. T. ü. *Eur. Phys. J. B*, 62:381, 2008. 30, 41
- [50] N. Mingo and L. Yang. *Phys. Rev. B*, 68:245406, 2003. 30
- [51] A. Sommerfeld. *Partial Differential Equations in Physics*. Academic Press, 1949. 31
- [52] T. Yao. *Appl. Phys. Lett.*, 51:1798, 1987. 39
- [53] G. Chen, A. Verma, and J. S. Smith. *Appl. Phys. Lett.*, 67:3554, 1995. 39
- [54] S. M. Lee, D. G. Cahill, and R. Venkatasubramanian. *Appl. Phys. Lett.*, 70:2957, 1997. 39
- [55] E. S. Landry, M. I. Hussein, and A. J. H. McGaughey. *Phys. Rev. B*, 77:184302,

2008. [39](#), [40](#)
- [56] S. C. Huberman, J. M. Larkin, A. J. H. McGaughey, and C. H. Amon. *Phys. Rev. B*, 88:155311, 2013. [39](#), [42](#), [47](#), [54](#), [62](#)
- [57] E. S. Landry and A. J. H. McGaughey. *Phys. Rev. B*, 79:075316, 2009. [39](#), [46](#)
- [58] K. Imamura, Y. Tanaka, N. Nishiguchi, S. Tamura, and H. J. Maris. *J. Phys.: Condens. Matter*, 15:8679, 2003. [39](#)
- [59] K. Termentzidis, P. Chantrenne, and P. Keblinski. *Phys. Rev. B*, 79:214307, 2009. [39](#)
- [60] Y. Chen, D. Li, J. R. Lukes, Z. Ni, and M. Chen. *Phys. Rev. B*, 72:174302, 2005. [39](#), [40](#)
- [61] T. Zhu and E. Ertekin. *Phys. Rev. B*, 90:195209, 2014. [39](#), [40](#), [62](#)
- [62] I. Savic, D. Donadio, F. Gygi, and G. Galli. *Appl. Phys. Lett.*, 102:073113, 2013. [39](#)
- [63] J. Garg, N. Bonini, and N. Marzari. *Nano Lett.*, 11:5135, 2011. [39](#)
- [64] M. N. Luckyanova, J. Garg, K. Esfarjani, A. Jandi, M. T. Bulsara, A. J. Schmidt, A. J. Minnich, S. Chen, M. S. Dresselhaus, Z. Ren, E. A. Fitzgerald, and G. Chen. *Science*, 338:936, 2012. [39](#), [41](#)
- [65] M. V. Simkin and G. D. Mahan. *Phys. Rev. Lett.*, 84:927, 2000. [39](#), [40](#), [41](#), [54](#), [62](#)
- [66] J. Jiang, J. Wang, and B. Wang. *Appl. Phys. Lett.*, 99:043109, 2011. [40](#)
- [67] J. Ravichandran, A. K. Yadav, R. Cheoito, P. B. Rossen, A. Soukiassian, S. J. Suresha, J. C. Duda, B. M. Foley, C.-H. Lee, Y. Zhu, A. W. Lichtenberger, J. E. Moore, D. A. Muller, D. G. Schlom, P. E. Hopkins, A. Majumdar, R. Ramesh, and M. A. Zurbuchen. *Nat. Mat.*, 13:168, 2014. [40](#), [41](#), [54](#), [62](#)
- [68] W. A. Little. *Can. J. Phys.*, 37:334, 1959. [40](#)

- [69] S. Pettersson and G. D. Mahan. *Phys. Rev. B*, 42:7386, 1990. 40
- [70] P. K. Schelling, S. R. Phillpot, and P. Keblinski. *Appl. Phys. Lett.*, 80:2484, 2003. 40
- [71] A. Maiti, G. D. Mahan, and S. T. Pantelides. *Solid State Commun.*, 102:517, 1997. 40
- [72] C. J. Twu and J. R. Ho. *Phys. Rev. B*, 67:205422, 2003. 40
- [73] R. J. Stevens, L. V. Zhigilei, and P. M. Norris. *Int. J. Heat Mass Transfer*, 50:3977, 2007. 40
- [74] J. C. Duda, T. S. English, E. S. Piekos, W. A. Soffa, L. V. Zhigilei, and P. E. Hopkins. *Phys. Rev. B*, 84:193301, 2011. 41, 42, 44, 49, 82
- [75] E. S. Landry and A. J. H. McGaughey. *J. Appl. Phys.*, 107:013521, 2010. 41, 54
- [76] Z. Tian, K. Esfarjani, and G. Chen. *Phys. Rev. B*, 89:235307, 2014. 41, 54
- [77] H. Zhao and J. B. Freund. *J. Appl. Phys.*, 105:013515, 2009. 41
- [78] A. J. H. McGaughey. *Phonon transport in molecular dynamics simulations: formulation and thermal conductivity prediction*. PhD thesis, University of Michigan, Ann Arbor, 2004. 42, 53, 93, 94
- [79] L. Hu, W. J. Evans, and P. Keblinski. *J. Appl. Phys.*, 110:113511, 2011. 43, 95
- [80] A. J. H. McGaughey and M. Kaviani. *Phys. Rev. B*, 71:184305, 2005. 47
- [81] K. Sääskilahti, J. Oksanen, J. Tulkki, and S. Volz. *Phys. Rev. B*, 90:134312, 2014. 47, 59
- [82] Y. Chalopin, N. Mingo, J. Diao, D. Srivastava, and S. Volz. *Appl. Phys. Lett.*, 101:221903, 2012. 59
- [83] Y. Chalopin and S. Volz. *Appl. Phys. Lett.*, 103:051602, 2014. 59

- [84] A. K. Geim. *Science*, 324:1530, 2009. [61](#)
- [85] S. Ghosh, I. Calizo, D. Teweldebrhan, E. P. Pokatilov, D. L. Nika, A. A. Balandin, W. Bao, F. Miao, and C. N. Lau. *Appl. Phys. Lett.*, 92:151911, 2008. [61](#)
- [86] A. A. Balandin, S. Ghosh, W. Bao, I. Calizo, D. Teweldebrhan, F. Miao, and C. N. Lau. *Nano Lett.*, 8:902, 2008. [61](#)
- [87] S. Chen, A. L. Moore, W. Cai, J. W. Suk, J. An, C. Mishra, C. Amos, C. W. Magnuson, K. Kang, L. Shi, and R. S. Ruoff. *ACS Nano*, 5:321, 2011. [61](#), [81](#)
- [88] G. Fugallo, A. Cepellotti, L. Paulatto, M. Lazzeri, N. Marzari, and F. Mauri. *Nano Lett.*, 14:6109, 2014. [61](#)
- [89] D. L. Nika, E. P. Pokatilov, A. S. Askerov, and A. A. Balandin. *Phys. Rev. B*, 79:155413, 2009. [61](#)
- [90] L. Lindsay, D. A. Broido, and N. Mingo. *Phys. Rev. B*, 83:235428, 2011. [61](#), [79](#)
- [91] J. H. Seol, L. Jo, A. L. Moore, L. Lindsay, Z. H. Aitken, M. T. Pettes, X. Li, Z. Yao, R. Huang, D. Broido, N. Mingo, R. S. Ruoff, and L. Shi. *Science*, 328:213, 2010. [61](#), [78](#)
- [92] W. Cai, A. L. Moore, Y. Zhu, X. Li, S. Chen, L. Shi, and R. S. Ruoff. *Nano Lett.*, 10:1645, 2010. [61](#), [78](#)
- [93] C. Wang, J. Guo, L. Dong, A. Aiyiti, X. Xu, and B. Li. *Sci. Rep.*, 6:25334, 2016. [61](#)
- [94] L. Lindsay and D. A. Broido. *Phys. Rev. B*, 84:155421, 2011. [61](#)
- [95] J.-W. Jiang and J.-S. Wang. *Europhys. Lett*, 96:16003, 2011. [62](#)
- [96] C. da Silva, F. Saiz, D. A. Romero, and C. H. Amon. *Phys. Rev. B*, 93:125427, 2016. [62](#)
- [97] Z.-Y. Ong and G. Zhang. *Phys. Rev. B*, 91:174302, 2015. [62](#), [69](#)

- [98] Z.-Y. Ong, G. Zhang, and Y.-W. Zhang. *Phys. Rev. B*, 93:075406, 2016. 62, 63, 70
- [99] V. K. Tewary and B. Yang. *Phys. Rev. B*, 79:125416, 2009. 62
- [100] Z. Huang, J. Y. Murthy, and T. S. Fisher. *J. Heat Transfer*, 133:114502, 2011. 63
- [101] L. Lindsay and D. A. Broido. *Phys. Rev. B*, 81:205441, 2010. xix, 65, 66, 67
- [102] C. Sevik, A. Kinaci, J. B. Haskins, and T. Cagin. *Phys. Rev. B*, 84:085409, 2011. xix, 65, 66, 67
- [103] I. M. Lifshitz. *Zh. Eksp. Teor. Fiz.* 65
- [104] J. Tersoff. *Phys. Rev. B*, 39:5566, 1989. 66
- [105] L. A. Girifalco, M. Hodak, and R. S. Lee. *Phys. Rev. B*, 62:13104, 2000. 66, 68
- [106] K. Yan, H. Peng, Y. Zhou, H. Li, and Z. Lio. *Nano Lett.*, 11:1106, 2011. 68
- [107] J. C. Duda, J. L Smoyer, P. M. Norris, and P. E. Hopkins. *Appl. Phys. Lett.*, 95:031912, 2009. 69
- [108] J. C. Duda, P. M. Norris, and P. E. Hopkins. *J. Heat Transfer*, 133:74501, 2011. 69
- [109] W. I. F. David, R. M. Ibberson, J. C. Matthewman, K. Prassides, T. J. S. Dennis, J. P. Hare, H. W. Kroto, R. Taylor, and D. R. M. Walton. *Nature*, 353:147, 1991. 83
- [110] H. W. Kroto, J. R. Heath, S. C. O'Brien, R. F. Curl, and R. E. Smalley. *Nature*, 318:162, 1985. 83
- [111] P. W. M. Blom, V. D. Mihailetschi, L. J. A. Koster, and D. E. Markov. *Adv. Mater.*, 19:1551, 2007. 83
- [112] R. Saran, V. Stolojan, and R. J. Curry. *Sci. Rep.*, 4:5041, 2014. 83
- [113] C. Kim. *Appl. Phys. Lett.*, 92:013109, 2008. 83
- [114] N. S. Sariciftci, A. J. Heeger L. Smilowitz, and F. Wudl. *Science*, 258:1474, 1992. 83
- [115] J. R. Olson, K. A. Topp, and R. O. Pohl. *Science*, 259:1145, 1993. 84

- [116] J. C. Duda, P. E. Hopkins, Y. Y. Shen, and M. C. Gupta. *Appl. Phys. Lett.*, 102:251912, 2013. 84
- [117] J. C. Duda, P. E. Hopkins, Y. Y. Shen, and M. C. Gupta. *Phys. Rev. Lett.*, 110:015902, 2013. 84
- [118] L. Chen, X. Jia, and S. Kumar. *Sci. Rep.*, 5:12763, 2015. 84, 94
- [119] P. Senn. *J. Chem. Educ.* 85
- [120] W. L. Ong. Personal communication. 92
- [121] Y. Jin, J. Cheng, M. Varma-Nair, G. Liang, Y. Fu, B. Wunderlich, X. D. Xiang, R. Mostovoy, and A. K. Zettl. *J. Phys. Chem.*, 96:5151, 1992. xvi, 92, 94